Dissertation
submitted to the
Combined Faculties for the Natural Sciences and for Mathematics
of the Ruperto-Carola University of Heidelberg, Germany
for the degree of
Doctor of Natural Sciences

Put forward by
M. Sc. Claudia Katharina Spindeldreier
Born in: Bielefeld, Germany

Oral examination: January 26th, 2018

Dosimetry with ionization chambers and optically stimulated luminescence detectors in magnetic fields

Referees: Prof. Dr. Joao Seco
Prof. Dr. Oliver Jäkel

Erklärung

Ich erkläre hiermit, dass ich die vorgelegte Dissertation selbst verfasst und mich dabei keiner anderen als der von mir ausdrücklich bezeichneten Quellen und Hilfen bedient habe.

Heidelberg, den 13.11.2017

Claudia Katharina Spindeldreier

Abstract

Hybrid magnetic resonance guided radiotherapy (MRgRT) devices allow imaging the patient during treatment by means of non-ionizing radio-frequency. This technology enables real-time image guided radiotherapy, thereby it is expected to improve treatment precision and clinical outcome. In order to use hybrid MRgRT devices clinically, dosimetry needs to be performed in the static magnetic field of the magnetic resonance imaging scanner for commissioning and quality assurance measurements.

For this purpose, the applicability of two detector types - ionization chambers and optically stimulated luminescence detectors (OSLDs) - for dosimetry in magnetic fields was investigated in this work by means of experimental measurements and Monte Carlo simulations. The ionization chambers show a response that depends on the magnetic field strength and orientation as well as on the sensitive chamber volume. Likewise, the effective point of measurement is influenced by these parameters. In order to account for these effects, magnetic field correction factors were calculated. Also the response of OSLDs was found to depend on the magnetic field strength and direction. No substantial change in their angular dependence due to the magnetic field could be measured.

In conclusion, both detector types can be used for precise dosimetry in high magnetic fields when applying the calculated magnetic field correction factors or when calibrating the detectors directly in the magnetic field.

Zusammenfassung

Kombinierte Geräte bestehend aus einem Magnetresonanztomopgraphen (MRT) und einer Bestrahlungsanlage ermöglichen es, während der Bestrahlung ohne zusätzliche ionisierende Strahlendosis MR-Bilder von Patienten aufzunehmen. Damit legen sie die Basis für eine echtzeit-bildgeführte Therapietechnik, von der eine Steigerung der Bestrahlungspräzision und des klinischen Therapieerfolgs erhofft wird. Für die klinische Einführung dieser Geräte ist es notwendig, Dosimetrie im Hochmagnetfeld des MRTs durchzuführen.

In dieser Arbeit wurde die Anwendbarkeit von zwei Detektortypen - Ionisationskammern und optisch stimulierte Lumineszenz-Detektoren (OSLDs) - für die Dosimetrie in starken Magnetfeldern mittels Experimenten und Monte Carlo Simulationen untersucht. Es zeigte sich, dass das Ansprechverhalten von Ionisationskammern von der Magnetfeldstärke und Magnetfeldrichtung sowie dem sensitiven Volumen der Kammern abhängt. Der effektive Messort der Kammern wird ebenfalls von diesen Parametern beeinflusst. Um diese Effekte zu berücksichtigen, wurden Magnetfeld-Korrektionsfaktoren berechnet. Auch das Ansprechen der OSLDs ist von der Magnetfeldstärke und -richtung abhängig. Eine Änderung der Winkelabhängigkeit der OSLDs durch das Magnetfeld konnte messtechnisch nicht festgestellt werden.

Zusammenfassend sind beide Detektortypen für die präzise Dosimetrie im Magnetfeld geeignet, wenn entsprechende Korrektionsfaktoren verwendet oder die Detektoren direkt im Magnetfeld kalibriert werden.

Contents

Acronyms

CPE	charged particle equilibrium
CSDA	continuous slowing down approximation
CT	computed tomography
ERE	electron return effect
EPID	electronic portal imaging device
EPOM	effective point of measurement
IGRT	image guided radiation therapy
IMRT	intensity modulated radiation therapy
IPSS	intermediate phase space scoring
KERMA	kinetic energy released per unit mass
LED	light-emitting diode
NRC	National Research Council of Canada
MLC	multi leaf collimator
MRgRT	magnetic resonance guided radiation therapy
MRI	magnetic resonance imaging
linac	linear accelerator
OAR	organ at risk
OSLD	optically stimulated luminescence detector
PDD	percentage depth dose
PMT	photomultiplier tube
PTV	planning target volume

PSD	plastic scintillation detector
QA	quality assurance
SCD	source to chamber distance
SSD	source to surface distance
TPR	tissue phantom ratio
TPS	treatment planning system
TLD	thermoluminescent detector
VRT	variance reduction technique
XCSE	photon cross section enhancement

Chapter 1

Introduction

The aim of modern radiotherapy is to tailor a high dose region precisely to the target, while organs at risk (OARs) and healthy tissue are optimally spared. This results in an effectively treated tumor, while side effects are reduced. With the development of image guided radiation therapy (IGRT), patient positioning and target localization and thus the precision of the therapy itself can be improved. However, when using computed tomography (CT) or x-ray radiography as imaging modalities, constraints in terms of imaging frequency and duration are required to limit the additional dose of ionizing radiation to the patient.

To overcome the problem of imaging dose, magnetic resonance imaging (MRI) devices that acquire images with non-ionizing radio-frequency instead of ionizing radiation can be used. This concept, called magnetic resonance guided radiation therapy (MRgRT) resulted in the development of hybrid machines combining a radiotherapy device with an MRI scanner (Mutic and Dempsey, 2014; Lagendijk et al., 2014b; Fallone, 2014; Keall et al., 2014). With these devices, patients can be imaged before and during treatment without delivering additional imaging dose. Another advantage of the MRI scans is the high soft-tissue contrast. The target, but also OARs, are directly visible during treatment. The images can not only be used for patient positioning and target localization before the treatment, but also for motion mitigation like gating and tracking of the target during irradiation. Moreover, changes in the anatomy like weight loss or organ filling can be considered by adapting the treatment plan according to the current MR images. Functional MR imaging might be useful for target delineation and visualization of the radiation response (Lagendijk et al., 2014a). Therefore, MRgRT devices have the potential to shrink target margins, escalate the dose to the tumor and thus are expected to improve treatment precision and clinical outcome.

However, the static magnetic field of the MRI implicates new challenges: The Lorentz force deflects the secondary electrons, produced when the primary photons travel through matter. This deflection results in a change of the dose distribution. Moreover, the response of radiation detectors is influenced by the magnetic field (O'Brien et al., 2016). Since precise dosimetry is crucial for the high precision MRgRT devices, the behavior of radiation detectors in the magnetic field needs to be understood in detail and a protocol for dosimetry in magnetic fields has to be developed.

Therefore, the aim of this project was to investigate the detector response of two clinical detector types in magnetic fields and calculate magnetic field correction factors by means of experiments and Monte Carlo simulations.
The two detector types were air-filled ionization chambers and Al_2O_3:C optically stimulated luminescence detectors (OSLDs). To validate the Monte Carlo simulations, the consistency of the simulated particle transport in a magnetic field was tested and experimental response measurements were compared to the simulations.

Ionization chambers were examined as they are used routinely for precise absolute and relative dosimetry for machine commissioning and quality assurance (QA) tests. Since electrons have a large mean free path length in air compared to water, they can travel on circular paths inside the air cavity due to the deflection by the Lorentz force. This results in a manipulated signal of the chambers in magnetic fields (Meijsing et al., 2009). In this work, the influence of the magnetic field strengths, the chamber radius and the orientation between beam, magnetic field and chamber on the response was investigated. Furthermore, the impact of the sensitive volume of the chambers on the response was examined, since dead volumes can change the chamber response substantially. Finally, the effective point of measurement (EPOM) of ionization chambers in magnetic fields was studied.

OSLDs as solid state detectors are used clinically for relative dosimetry in QA tests and in-vivo patient dose measurements. Due to the larger density of the sensitive material, smaller effects of the magnetic fields on the detector response are expected, compared to air-filled ionization chambers. When used as passive detectors, only the energy deposition process occurs in presence of the magnetic field, the read-out is performed separately in a dedicated reader. No electricity or ferro-magnetic materials that might interfere with the magnetic field of the MRI are used. Combined with the feasibility of high precision point measurements (Yukihara et al., 2005) and 2D dosimetry (Ahmed et al., 2014), OSLDs are promising for dosimetry in hybrid MRgRT devices.
In this work, the response of OSLDs in high magnetic fields was investigated by means of measurements and simulations. Magnetic field correction factors for different orientations of detector and magnetic field were calculated. The angular dependence and the feasibility of point measurements in a heterogeneous phantom in a magnetic field were studied.

The thesis is structured in six chapters. Following the introduction (chapter 1), the materials and methods used in this thesis (chapter 2) are described. The experiments and results are presented in chapters 3 and 4 and discussed in chapter 5. Finally, the thesis closes with conclusions and an outlook in chapter 6.

Chapter 2

Materials and methods

In this section, the material and methods used throughout the thesis are described. A description of the concepts of radiation therapy, the physics of ionizing radiation and radiation dosimetry is given. Moreover, the detectors and the equipment used in the experiments as well as the Monte Carlo simulation software are presented.

2.1 Principles of radiation therapy

The basic principle of radiation therapy is to treat tumors with ionizing radiation while sparing healthy tissue (see figure 2.1). Today mostly modern linear accelerators (linacs) with energies between 6 - 18 MV are used for photon beam generation. The dose to the target is formed by modulating the fluence with multi leaf collimators (MLCs) and overlaying several radiation fields from different beam angles.
On a cellular level, ionizing radiation induces DNA damage in the cells (single or double-strand breaks) which can lead to cell death. However, this process occurs not only in the tumor, but also in healthy tissue. Therefore, modern treatment techniques like intensity modulated radiation therapy (IMRT) sparing healthy tissue and fractionated treatment schemes are in use. The latter exploits the fact that sub-lethal damage repair is more efficient in healthy cells than in tumor cells. Hence, the treatment is divided into several fractions with small doses (see figure 2.1) delivered over several days or weeks (Liauw et al., 2013).

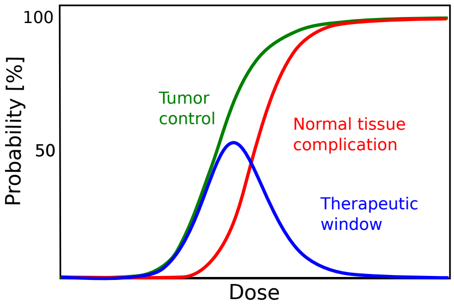

Figure 2.1: The ratio of tumor control and normal tissue complication defines the therapeutic window of radiation therapy. Adapted from (Podgorsak, 2005).

2.1.1 Image guided radiation therapy

Modern treatment techniques like 3D conformal radiotherapy and IMRT are routinely used and allow a conformal irradiation of the planning target volume (PTV) while sparing OARs and normal tissue. The accuracy in target localization and the visualization of the surrounding tissue are crucial for these treatment techniques. In IGRT procedures, imaging methods are used for target localization and patient anatomy visualization before and during treatment.

In order to correct for *inter-fractional* changes, images of the target volume before each fraction can be acquired with kV-tubes and flat panel detectors installed at modern linacs. Moreover, an MV electronic portal imaging device (EPID) enables MV imaging with the linac beam. In both images the soft tissue contrast for PTV visualization is rather low, but the planned target position can be determined in relation to the bony structure or implanted markers. For the assessment of 3D images, cone-beam CTs with the kV or MV source can be acquired. In-room CTs can be installed to obtain high resolution 3D images before treatment for target localization, but also for dose reconstruction and comparison with the reference plan.
Moreover, dedicated systems like the helical tomotherapy combine features of a linac and a helical CT. While the gantry rotates, the treatment couch is translated slowly, creating a helical motion of the beam. In that way, it delivers IMRT plans and simultaneously acquires MV CT images with the treatment beam (Khan and Gibbons, 2014).

For tumors with a high *intra-fractional* motion amplitude, techniques like tumor gating and tracking can be used. Without motion management, PTV margins have to be large to cover the moving tumor with the beam. The aim of gating and tracking techniques is to shrink these margins with the potential to escalate the dose to the tumor.
For these management techniques, markers are detected with fluoroscopy or electromagnetic field tracking systems to determine the tumor motion. Furthermore, optical systems monitor the surface motion. In combination with correlation models, determined e.g. with the help of 4D CTs, the tumor motion can be predicted from the surface motion.
The problem of IGRT with devices using ionizing radiation is the potential for an excessive imaging dose to the patient. The additional dose needs to be balanced with improvements in the delivery of therapeutic dose (Khan and Gibbons, 2014). A possible solution of this problem might be MRgRT which uses MR imaging before and during treatment.

2.1.2 Magnetic resonance guided radiation therapy

MRgRT exploits the advantage of excellent soft-tissue contrast images of the patient without delivering imaging dose to the patient. Since radio-frequency instead of ionizing radiation is used for image generation, no constraints on imaging frequency and duration are needed. Thus, in principal the tumor location and motion can be monitored during the whole treatment, preferably in real-time for tumor gating and tracking (Crijns et al., 2011). Consequently, MRgRT might lead to PTV margin reduction and dose escalation to the tumor. The acquired image also visualizes changes in the patient anatomy and can be used for treatment adaptation as well as dose reconstruction and accumulation (Lagendijk et al., 2014a; Glitzner et al., 2015). Moreover, functional MR imaging can be used for tumor delineation and radiation response monitoring.

Two MRgRT approaches exist: (i) Offline MRgRT can be performed with a shuttle system or a table shared by the linac and the MRI. The patient is imaged at a conventional MRI in treatment position and is transported in this position to the linac for therapy. In this way, inter-fractional changes can be accurately monitored (Karlsson et al., 2009; Jaffray et al., 2014; Bostel et al., 2014). (ii) Online MRgRT uses special devices that integrate an MRI into a radiotherapy unit. These devices have the potential for inter- and intra-fractional motion visualization and real-time adaptation (Kupelian and Sonke, 2014). However, new challenges due to the permanent magnetic field in these devices are arising (see section 2.3.4).

Several hybrid MRgRT devices exist or are currently under development: The first clinical device, the MRIdian® from ViewRay®, combines three ^{60}Co heads with a transverse low-field 0.35 T MRI (Mutic and Dempsey, 2014). By now, the ^{60}Co heads can be upgraded to a conventional 6 MV linac. A research group in Utrecht developed together with Elekta and Philips the Unity machine - a 7 MV linac with a 1.5 T transverse magnetic field (Lagendijk et al., 2014b). Moreover, the MagnetTx Aurora RT™, developed at the Cross Cancer Institute, integrates a 0.5 T MRI with a 6 MV linac, where beam and magnetic field are aligned parallel (Fallone, 2014). Within the Australian MR-linac project a combination of a 6 MV linac with a 1 T inline MRI is investigated. In this device, the patient is rotated instead of the photon beam for treatment (Keall et al., 2014).

First reports reveal that (online-adaptive) MRgRT could be successfully integrated into clinical routine (Chen et al., 2017; Fischer-Valuck et al., 2017). Clinical trials will specify the most suitable adaptive workflow and the patient cohort that benefits most from this technique.

Furthermore, the potential and challenges of MR guided proton therapy are investigated, including the impact of the magnetic field on beam delivery and dose distribution (Raaymakers et al., 2008; Moteabbed et al., 2014; Oborn et al., 2015; Schellhammer and Hoffmann, 2017; Oborn et al., 2017).

2.2 Physics of ionizing radiation

2.2.1 Interactions of photons with matter

Photons with energies applied in radiotherapy may interact with matter through coherent Rayleigh scattering, photoelectric absorption, incoherent Compton scattering or pair production. Thereby, the amount of photons passing the medium of a certain thickness is decreased exponentially. The total attenuation coefficient is the sum of the individual contributions

$$\mu(E_\gamma, Z) = \sigma_R(E_\gamma, Z) + \tau(E_\gamma, Z) + \sigma(E_\gamma, Z) + \kappa(E_\gamma, Z) \tag{2.1}$$

with σ_R, τ, σ and κ the attenuation coefficients of Rayleigh scattering, photo effect, Compton effect and pair production (Schlegel and Bille, 2002).

In Rayleigh scattering the photon is elastically scattered without energy loss. The photoelectric effect occurs mostly for low-energy photons. In this process, the photon interacts with tightly bound electrons of the absorber's inner atomic shell. The photon is totally absorbed and the electron is released with a kinetic energy of the initial photon energy reduced by the electron binding energy.
The Compton effect is the dominant effect for photon energies between approximately 0.1 to 10 MeV in water (see figure 2.2). The photon interacts with an essentially free electron and transfers a part of its energy to the electron. The electron is released with a certain kinetic energy and the photon is scattered. In a pair production process, the photon is absorbed and an electron-positron pair is generated in the Coulomb force field usually near an atomic nucleus. With lower probability this process can take place in the field of an atomic electron (triplet production). For pair production a minimum energy of $2m_0c^2 = 1.022$ MeV is needed (Attix, 2004).

2.2.2 Interactions of electrons with matter

Charged particles in a medium interact with the absorber via Coulomb interactions with the absorber's orbital electrons or nuclei. In most of these interactions only a small amount of energy is transferred, such that one can refer to the continuous slowing down approximation (CSDA) of charged particles. Different types of interactions can be distinguished:
Soft collisions occur when the charged particle passes an atom at a large distance. The Coulomb field of the charged particle excites the absorber atom to a higher energy level and might ionize it by ejection of a valence electron. In *hard collisions*, the charged particles interact with single atomic electrons that are ejected from the atomic shell with a considerable kinetic energy (delta rays). Coulomb-force interactions with the external nuclear field of the absorber atoms might occur, when the electron passes the nucleus at a very small distance. The electron is elastically scattered or inelastic radiative interactions take place leading to bremsstrahlung emission (Attix, 2004).

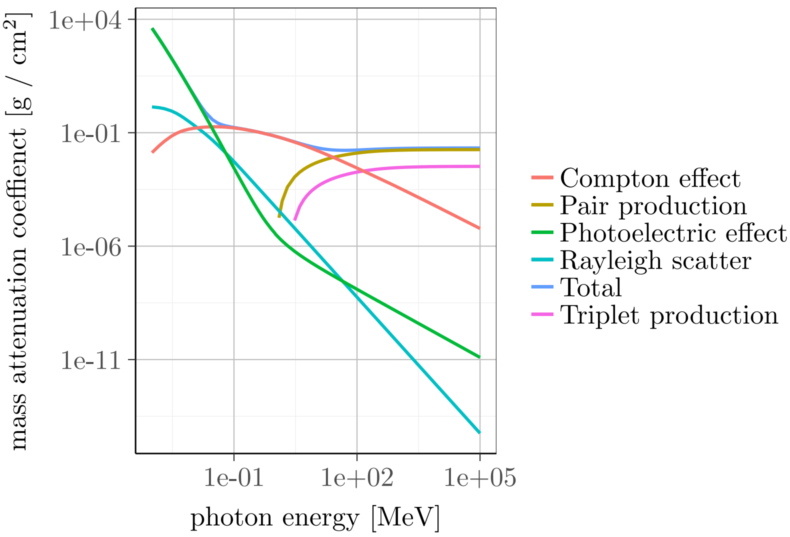

Figure 2.2: Total photon mass attenuation and its individual contributions for water as a function of energy. Data taken from the XCOM data base (Berger et al., 2010).

The energy loss of charged particles per unit length x can be described via the stopping power $S = dE/dx$ of a material. It consists of a collisional and a radiative contribution. The collision stopping power can be expressed as

$$S_{col} = (dE/dx)_{col} = \rho 2\pi r_e^2 m_0 c^2 \frac{Z}{uA} z^2 \frac{1}{\beta^2} R^*_{col}(\beta) \tag{2.2}$$

with the absorber's density ρ, the classical electron radius r_e, the electron rest mass m_0, the speed of light c, the absorber's atomic number Z and weight A, the atomic mass u, the charge z of the projectile, the ratio of particle velocity and velocity of light β and a rest function R^*_{col} that differs for electrons and positrons (Krieger, 2012).
The range of an electron R is the expectation value of its path length until it loses all its energy and stops. It varies stochastically depending on the individual interactions of the electron in matter. In the CSDA approach the range is calculated with the stopping power S as (Attix, 2004)

$$R_{CSDA}(E) = \int_0^{E_0} \left(\frac{S}{\rho}\right)^{-1} dE. \tag{2.3}$$

2.2.3 Electrons in magnetic fields

For hybrid MRgRT devices, the interaction of the magnetic field with secondary electrons has to be considered. Electrons in a magnetic field are deflected by the Lorentz force in a direction perpendicular to the magnetic field and the motion direction of the electron (see figure 2.3).

The Lorentz force is defined as

$$\vec{F_L} = e\vec{v} \times \vec{B} \tag{2.4}$$

with the elementary charge e, the velocity of the electron $\vec{v}$ and the magnetic field strength $\vec{B}$. Due to the Lorentz force, the electrons will travel on circular or helical paths in vacuum. The radius r of the curvature can be calculated by equating the centrifugal force $F_z = mv^2/r$ with the Lorentz force F_L. For the relativistic case, one obtains

$$r = \frac{mv}{eB} = \frac{m_0\gamma\beta c}{eB} = \frac{m_0\gamma c}{eB}\sqrt{1-\frac{1}{\gamma^2}}, \tag{2.5}$$

with $m = \gamma m_0$, $\beta = v/c = \sqrt{1-\frac{1}{\gamma^2}}$. The parameter γ can be derived via the relativistic kinetic energy

$$E_{kin,rel} = m_0c^2 \cdot (\gamma - 1). \tag{2.6}$$

Electron radii calculated for several mono-energetic electrons in homogeneous magnetic fields are presented in table 2.1.

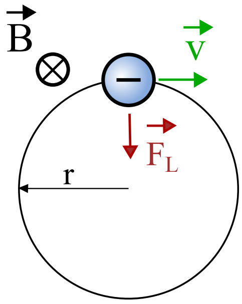

Figure 2.3: If magnetic field and electron velocity are perpendicular to each other, the Lorentz force deflects the electron onto a circular track.

Table 2.1: Radii of electron trajectories for different electron energies in magnetic fields from 0.7 T to 1.0 T, calculated relativistically.

$E_{kin,rel}$ [MeV]	γ	$r_{0.7T}$ [mm]	$r_{0.8T}$ [mm]	$r_{0.9T}$ [mm]	$r_{1.0T}$ [mm]
0.5	1.98	4.16	3.64	3.23	2.91
1.0	2.96	6.78	5.93	5.27	4.74
1.5	3.94	9.27	8.11	7.21	6.49
2.0	4.91	11.72	10.25	9.11	8.20
3.0	6.87	16.55	14.48	12.87	11.59
6.0	12.74	30.93	27.07	24.06	21.65

2.3 Radiation dosimetry

2.3.1 Dosimetric quantities

In the following, dosimetric quantities needed for the quantification of radiation effects are described.

Energy imparted

The energy imparted ϵ is a stochastic quantiy and can be expressed by (Schlegel and Bille, 2002)

$$\epsilon = R_{in} - R_{out} + \sum Q, \text{ unit: J} \tag{2.7}$$

with

$R_{in} =$ incoming radiant energy of all charged and uncharged particles in the reference volume, without rest masses,
$R_{out} =$ radiant energy leaving the reference volume, without rest masses,
$\sum Q =$ sum of all changes in rest masses of all particles in the reference volume.

Absorbed dose

The absorbed dose D is a macroscopic quantity, i.e. it is differentiable in time and space. It is defined by

$$D = \frac{d\bar{\epsilon}}{dm}, \text{ unit: } \frac{\text{J}}{\text{kg}} \text{ or Gy} \tag{2.8}$$

with ϵ being the energy imparted and m being the mass of the reference volume (Attix, 2004).

The dose rate $\dot{D}$ is defined as (Schlegel and Bille, 2002)

$$\dot{D} = \frac{dD}{dt}. \tag{2.9}$$

Moreover, under the conditions that (1) radiative photons leave the reference volume and (2) secondary electrons are absorbed on the spot (or a charged particle equilibrium (CPE) exists), the absorbed dose in a medium D_{med} is related to the electron fluence spectrum by

$$D_{med} = \Phi_{med} \left(\frac{\overline{S}}{\rho}\right)_{med} \tag{2.10}$$

with $\left(\frac{\overline{S}}{\rho}\right)_{med}$ being the spectrum averaged collision stopping power of the medium (Podgorsak, 2005).

KERMA

The quantity kinetic energy released per unit mass (KERMA) K describes the first step in energy dissipation by indirectly ionizing radiation (photons, neutrons), i.e. the energy transfer to charged particles:

$$K = \frac{dE_{tr}}{dm}, \text{ unit: } \frac{\mathrm{J}}{\mathrm{kg}} \text{ or Gy} \tag{2.11}$$

where dE_{tr} represents the sum of the initial kinetic energies of all charged particles released by the indirectly ionizing radiation in the reference volume. KERMA can also be expressed as

$$K = \Psi \left(\frac{\mu_{tr}}{\rho} \right) = \Phi \left[E \left(\frac{\mu_{tr}}{\rho} \right) \right] \tag{2.12}$$

with Ψ being the energy fluence, Φ the fluence and $\frac{\mu_{tr}}{\rho}$ the mass energy transfer coefficient (Attix, 2004). When using KERMA the reference material has to be stated, e.g. air KERMA or water KERMA. The quantity also includes the energy fraction of secondary charged particles that is transformed into bremsstrahlung and leaves the reference volume. Hence, KERMA can be written as the sum of collision and radiation KERMA (Schlegel and Bille, 2002):

$$K = K_{col} + K_{rad} \tag{2.13}$$

K_{col} refers to the transferred energy fraction that is locally dissipated by ionizations and excitations of secondary charged particles, whereas K_{rad} describes the energy fraction that is transformed into bremsstrahlung or positron annihilation radiation.
Under CPE conditions, absorbed dose equals collision kerma (Schlegel and Bille, 2002)

$$D^{CPE} = K_{col}. \tag{2.14}$$

2.3.2 Cavity theory

Cavity theory relates the absorbed dose in a cavity medium to the absorbed dose in the surrounding medium containing the cavity. This relation is needed to determine absorbed dose in a medium, since for dose measurements a dosimeter, usually with a different sensitive material, is placed in the medium (Podgorsak, 2005).

Bragg-Gray cavity theory

The Bragg-Gray cavity theory was the first cavity theory relating an absorbed dose in a dosimeter to the absorbed dose in the medium embedding the cavity. Two conditions have to be fulfilled for this theory:

1. The cavity is small compared to the range of charged particles, i.e. the cavity does not perturb the electron fluence in the medium.

2. No photon interactions occur in the cavity - thus the absorbed dose in the cavity is deposited only by charged particles crossing the cavity.

Condition (1) implies that the electron fluences are the same and equal to the equilibrium fluence in the surrounding medium. Condition (2) demands that no electrons are produced or absorbed inside the cavity. The fulfilment of the two conditions depends on the cavity size (based on the electron range in the medium), the cavity medium and the electron energy (Podgorsak, 2005).
Under these conditions, the ratio of doses in the cavity and in the medium surrounding the cavity can be derived with equation 2.10 to

$$\frac{D_{med}}{D_{cav}} = \frac{\Phi(\overline{S}/\rho)_{med}}{\Phi(\overline{S}/\rho)_{cav}} = \left(\frac{\overline{S}}{\rho}\right)_{med,cav} \tag{2.15}$$

with the average unrestricted mass collision stopping power $(\overline{S}/\rho)$ (Attix, 2004).

If the cavity medium is a gas in which the charge Q is created by ionizing radiation, D_{med} can be derived by

$$D_{med} = \frac{Q}{m}\left(\frac{\overline{W}}{e}\right)_{cav}\left(\frac{\overline{S}}{\rho}\right)_{med,cav} \tag{2.16}$$

with the mean energy spent per unit charge produced in the cavity material $\left(\frac{\overline{W}}{e}\right)_{cav}$ (Attix, 2004).

Spencer-Attix cavity theory

Delta electrons produced in hard collisions in the sensitive cavity volume are not considered in the Bragg-Gray theory. A more general theory formulation, that takes delta electrons having enough energy to produce further ionization into account, was derived by Spencer and Attix (Spencer and Attix, 1955; Spencer, 1965, 1971). This theory is still based on the two Bragg-Gray conditions, but these two conditions also refer to the secondary particle fluence.

The secondary electron fluence is separated into two parts by means of a user defined energy threshold Δ. Secondary electrons with kinetic energies below Δ are *slow electrons* depositing their energy locally, while secondary electrons with energies equal or above the threshold are considered *fast electrons* that are part of the electron spectrum. Thus, the electron spectrum ranges from the lower threshold Δ to $E_{kin,0}$ with $E_{kin,0}$ being the initial kinetic energy of the electrons. To calculate the energy deposition, the restricted stopping power ratio with threshold Δ, $\frac{L_\Delta}{\rho}$, and the fluence of fast electrons, Φ^{e-e}_{med}, where $^{e-e}$ represents the delta electron contribution in the slowing down process, are used. Since the Bragg-Gray condition demands no electron generation in the cavity, Δ is connected to the cavity size: The threshold Δ is the energy of electrons whose range corresponds to the mean cord length of the cavity. The Spencer-Attix relation can be expressed as

$$\frac{D_{med}}{D_{cav}} = s^{\Delta}_{med,cav} \tag{2.17}$$

where $s^{\Delta}_{med,cav}$ represents the ratio of the mean restricted mass collision stopping powers of the medium and the cavity:

$$s^{\Delta}_{med,cav} = \frac{\int_{\Delta}^{E_{kin,0}} \Phi^{e-e}_{med}(E) \left(\frac{L}{\rho}\right)_{\Delta,med} dE + TE_{med}}{\int_{\Delta}^{E_{kin,0}} \Phi^{e-e}_{med}(E) \left(\frac{L}{\rho}\right)_{\Delta,cav} dE + TE_{cav}} \tag{2.18}$$

TE_{med} and TE_{cav} are so-called track end terms and consider the energy deposition caused by electrons, which fall below Δ while passing through the cavity.
The difference between the Bragg-Gray and the Spencer-Attix cavity theories is non-negligible, but generally not significant. The ratio of collision stopping powers for two media is a very slow varying function with energy, because the collision stopping powers of different media show similar trends in dependence of the particle energy. For ionization chambers, the choice of the cut-off energy has only a weak influence on the stopping power ratio of water to air. Usually, a threshold of 10 keV is used for Farmer-type ionization chambers in radiation therapy (Podgorsak, 2005).

In the case of a real ionization chamber in a high energy photon or electron beam placed in a water phantom, perturbation always occurs due to the finite volume of the detector and the materials differing from water. Thus, to determine the dose to water D_w at depth z, the dose measured with the chamber $D_{chamber}$ has to be corrected by a perturbation factor p_Q (Podgorsak, 2005):

$$D_w(z) = D_{chamber}\ s^{\Delta}_{w,air}\ p_Q = \frac{Q}{m}\left(\frac{\overline{W}}{e}\right)_{air} s^{\Delta}_{w,air}\ p_{repl}\ p_{cel}\ p_{wall}\ p_{stem}\ p_{\Delta} \tag{2.19}$$

with

- the replacement perturbation factor p_{repl} (which can be divided into fluence perturbation factor p_{cav}, correcting for scattering differences between the air cavity and the surrounding water, and the displacement correction p_{dis} of the effective point of measurement),
- the central electrode perturbation factor p_{cel},
- the chamber wall perturbation factor p_{wall},
- the chamber stem perturbation factor p_{stem} (usually ignored in the current dosimetry protocols),
- the cut-off energy perturbation p_{Δ} accounting for the ionization chamber specific cut-off energy Δ in the Spencer-Attix stopping power ratio calculations (new factor in the current German dosimetry protocol DIN 6800-2 (DIN, 2008)).

2.3.3 Clinical radiation dosimetry

Clinical radiation dosimetry can be divided into reference dosimetry and relative dosimetry. Reference dosimetry aims to determine the absolute dose to water D_w in well-defined reference conditions, usually performed with calibrated ionization chambers. In relative dosimetry, measured doses or signals are normalized to a certain value, used e.g. to obtain percentage depth dose (PDD) curves or profiles of the radiation field.

Generally, to determine the absorbed dose to the medium, any direct or indirect physical effect of ionizing radiation can be used. These effects can be e.g. ionization of gas or liquids in ionization chambers, light emission of solid state detectors, chemical changes in dosimetry gels, colorization of films or temperature changes of the medium in calorimeters (Podgorsak, 2005) .

Ionization chambers

For the determination of dose, usually calibrated air-filled ionization chambers are used. They are inexpensive, give a reproducible and direct reading and a precise result under defined conditions. In principle, ionizing radiation produces ion pairs in the air cavity (energy transfer during interactions with air molecules). The generated charge Q is collected by the electrodes (see figure 2.4).

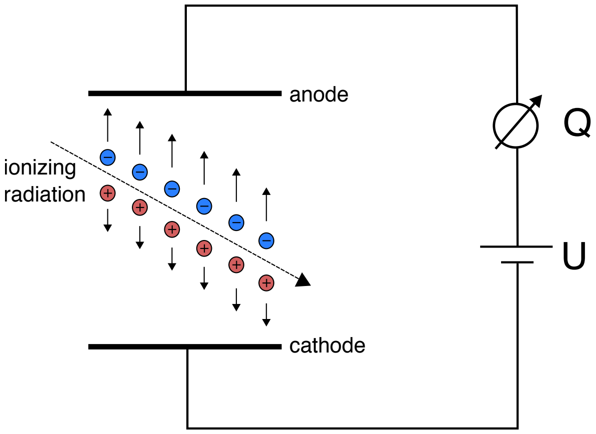

Figure 2.4: Schematic drawing of the basic principle of an ionization chamber: The incoming ionizing radiation generates positive and negative charge carriers, that are collected by the electrodes.

For the calculation of absorbed dose to the cavity D_{cav} the cavity volume V, the cavity gas density ρ, the measured charge Q and the energy needed to create an ion pair in air W_{air} are relevant (Podgorsak, 2005):

$$D_{cav} = \frac{Q}{\rho V} \cdot \frac{W_{air}}{e} \tag{2.20}$$

To determine the dose to water D_w at a point in the undisturbed water medium, cavity theory can be applied (see section 2.3.2).

In reality, cavity theory is not applied directly, but calibrated ionization chambers are used, because the exact dimensions of the cavity volume are usually unknown due to variations in the manufacturing process. Moreover, the chamber itself perturbs the radiation field. The procedures for reference dosimetry are described in national and international "dosimetry protocols" or "codes of practice" (Andreo et al., 2006; DIN, 2008; Almond et al., 1999): The absorbed dose to water for a reference beam quality Q_0 at a reference depth z_{ref} in absence of the chamber is given by

$$D_{w,Q_0} = M_{Q_0} N_{D_w,Q_0}. \tag{2.21}$$

The calibration coefficient N_{D_w,Q_0} is traceable to a primary standard laboratory. It connects the dosimeter reading M_{Q_0} to dose to water D_w under reference conditions. These references conditions refer to the radiation field size, the measurement depth, phantom size, beam quality Q_0 of the incident beam, but also air pressure and temperature (see table 2.2).

Table 2.2: Reference conditions for the determintion of absorbed dose according to Andreo et al. (2006).

Influencing quantity	Reference value
phantom size	30 x 30 x 30 cm^3
measurement depth	10 cm for 6 MV photons / 5 cm for ^{60}Co
field size	10 x 10 cm^2
source to surface distance (SSD)	100 cm
temperature T_0	293.15 K
pressure P_0	101.325 kPa

Since not all of these reference conditions can be established in the user's beam with beam quality Q, correction factors are applied:

$$D_{w,Q} = M_Q \; k_{T,P} \; k_{pol} \; k_s \; k_{Q,Q_0} \; N_{D_w,Q_0} \tag{2.22}$$

with

- the temperature and pressure correction $k_{T,P} = \frac{T}{T_0}\frac{P_0}{P}$ for vented chambers, since temperature and pressure have an impact on the mass of air in the cavity volume,
- the polarity correction $k_{pol} = \frac{|M_+| \, + \, |M_-|}{2M}$ with M_+ and M_- being the chamber readings for positive and negative polarity,
- the correction of incomplete charge collection due to ion recombination in the cavity k_s; for pulsed beams it can be calculated with the two-voltage method via $k_s = a_0 + a_1 \left(\frac{M_1}{M_2}\right) + a_2 \left(\frac{M_1}{M_2}\right)^2$ with constants a_i given in the TRS-398 dosimetry protocol and chamber readings M_1 and M_2 for voltages V_1 and V_2 with $V_1/V_2 \geq 3$,

- the beam quality correction factor that corrects for the difference between user beam quality Q and the reference quality Q_0. It is defined as the ratio of the calibration factors $k_{Q,Q_0} = \frac{N_{D_w,Q}}{N_{D_w,Q_0}} = \frac{D_{w,Q}/M_Q}{D_{w,Q_0}/M_{Q_0}}$. Moreover, it can be calculated theoretically by means of Bragg-Gray theory as $k_{Q,Q_0} = \frac{(s_{w,air})_Q}{(s_{w,air})_{Q_0}} \frac{p_Q}{p_{Q_0}}$ (Andreo et al., 2006).

The beam quality correction factor k_{Q,Q_0} is provided in the dosimetry protocols for various ionization chambers and beam qualities. In DIN and TRS, the beam quality Q is defined via the tissue phantom ratio $(\text{TPR})_{20,10}$ as the ratio of dosimeter reading in 10 cm and 20 cm depth with a constant source to chamber distance (SCD) in a water phantom (DIN, 2008; Andreo et al., 2006). In TG-51, the beam quality is defined as the percentage value of relative dose in 10 cm depth normalized to the depth dose maximum $\%dd(10)_x$ (under absence of contaminant electrons) (Almond et al., 1999).

For the determination of PDD curves, the so-called EPOM needs to be taken into account. The chamber placed into a water phantom displaces a certain amount of water. On the one hand, the reduced attenuation in air compared to water will cause an increased reading of the chamber. On the other hand, less scatter in air than in water results in the opposite effect. This can be corrected by shifting the position of the chamber, so that the effective point of measurement is placed at measurement depth when recording PDDs (Podgorsak, 2005). For cylindrical chambers, a shift of $0.6 \cdot r$ is recommended by the IAEA TRS protocol (Andreo et al., 2006), while the DIN protocol uses a shift of $0.5 \cdot r$ (DIN, 2008).

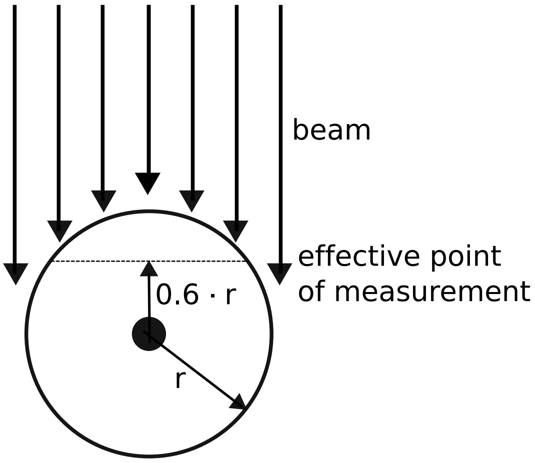

Figure 2.5: Schematic illustration of the effective point of measurement of cylindrical ionization chambers (with radius r) according to the TRS-398 protocol (Andreo et al., 2006).

Optically stimulated luminescence detectors

For relative or in-vivo dosimetry, OSLDs are used. They are easy-to-handle, have a high sensitivity and the fast read-out allows re-estimating the dose. The basic principle of OSLDs is the excitation of electrons from the valence to the conduction band by ionizing radiation, forming holes in the valence band. These holes and electrons can move freely in their valence and conduction band, until they either recombine or are captured in localized energy levels, so-called traps. The amount of trapped charge is a measure for the absorbed dose. By stimulating the trapped charges back to the conduction band, the electron-hole pairs recombine and generate luminescence which can be correlated to the trapped charge concentration and thus to the absorbed dose (Yukihara and McKeever, 2008).

Different read-out techniques can be used: In continuous-wave OSL (CW-OSL) the detectors are illuminated continuously while recording the OSL signal, whereas in pulsed OSL (POSL) the detectors are stimulated with short light pulses while monitoring the signal between the pulses and integrating it over many pulses. The OSL reader consists of a light source for stimulation, filters for wavelength selection of the light source, detection filters to block the stimulation light and a photomultiplier tube (PMT) as a light detector. Besides the use as passive detectors, OSL probes can be combined with optical fibers delivering the stimulation light to the detector and the OSL signal back to the reader allowing for real-time dosimetry.

In radiotherapy, mainly Al_2O_3:C detectors (Akselrod et al., 1998) are used. Their OSL signal is very stable at room temperature, hence room temperature fading is negligible over several months (Bøtter-Jensen et al., 1997). Additionally, the OSL response of Al_2O_3:C is approximately linear over a wide range of dose (up to ≈ 50 Gy with a small supralinearity above 2 Gy for 6 MV photon beams) (Yukihara and McKeever, 2006; Yukihara et al., 2007). The detectors are light sensitive and consequently have to be protected from light before read-out. The effective atomic number of Al_2O_3:C dosimeters is 11.28 which causes an overresponse to low-energy x-rays (Bos, 2001; Akselrod et al., 1990). However, the dependence on beam quality in the MV range is very small (Jursinic, 2007; Yukihara et al., 2007).

OSL detectors can be used for precise 1D point measurements (Yukihara et al., 2005), but also for high resolution 2D dosimetry using OSL films with a dedicated laser-scanning read-out system (Ahmed et al., 2014, 2016, 2017).

2.3.4 Dosimetry in magnetic fields

In hybrid MRgRT devices, the permanent magnetic field has to be considered for dosimetry. The magnetic field influences the secondary electrons by means of the Lorentz force (see section 2.2.3) and thus affects the dose distribution in water as well as the response of radiation detectors. These effects are dependent on the beam energy, magnetic field strength, the orientation between photon beam, magnetic field and detector and the detector type.

For a magnetic field perpendicular to the primary photon beam (see figure 2.6a), the dose maximum of the PDD curve is shifted towards shallower depths with increasing magnetic field. This is due to the shortened electron range in beam direction. For a 1.5 T field, this shift is about 4 - 5 mm and the dose behind the dose maximum is decreased by about 0.5% compared to the dose without magnetic field. The lateral profile is shifted approximately 1 mm in the direction of the Lorentz force (O'Brien and Sawakuchi, 2017). Profiles in the direction parallel to the magnetic field are not substantially influenced by the magnetic field. At high-density to low-density boundaries, electrons returning into the high-density medium due to the Lorentz force cause a dose increase (electron return effect (ERE)) (Raaijmakers et al., 2005, 2007, 2008).
The change in the dose distribution may also affect the beam quality specifiers: The $\%dd(10)_x$ decreases by about 2.4% for a 1.5 T perpendicular magnetic field, while the $\text{TPR}_{20,10}$ changes only by about 0.3%. Thus, the $\text{TPR}_{20,10}$ is recommended to be used for dosimetry in magnetic fields as a beam quality specifier insensitive to the magnetic field (O'Brien et al., 2016).
For a parallel magnetic field (see figure 2.6b), the surface dose might be increased due to contaminant electrons (Ghila et al., 2017). Behind the dose maximum no substantial changes in the PDD can be observed, while the penumbra of the radiation field can be controlled by the magnetic field strength (Bielajew, 1993).

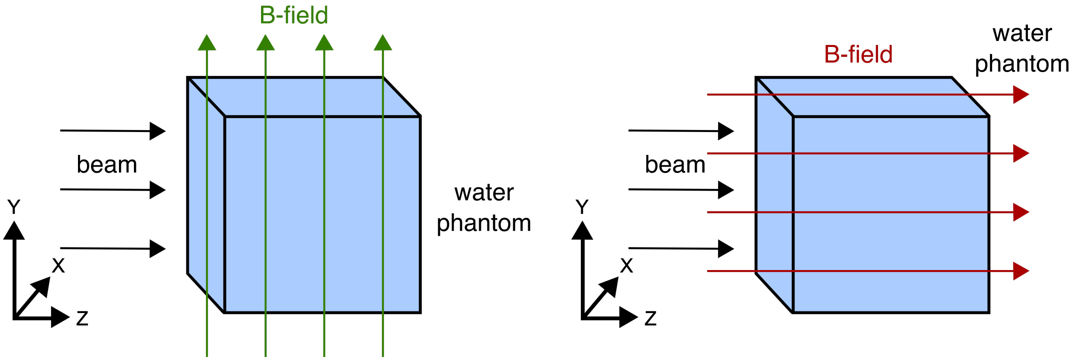

(a) (b)

Figure 2.6: Orientation of beam and magnetic field for the hybrid MRgRT systems: (a) Magnetic field and beam are aligned perpendicular to each other and (b) the magnetic field is aligned parallel to the beam.

In the air cavity of an ionization chamber, the electrons exhibit a large mean free path length. With a perpendicular magnetic field, the secondary electrons travel on helical paths inside the air volume. Consequently, the mean path length of electrons inside the chamber volume is changed compared to the path length in absence of a magnetic field. Thereby also the chamber response is altered in a magnetic field.

Several research groups investigated a variety of radiation detectors for dosimetry in magnetic fields: Large Farmer-type ionization chambers showed an increase in response of up to 7 - 11%, depending on the orientation to the magnetic field and beam (Meijsing et al., 2009; Smit et al., 2013; Reynolds et al., 2013, 2015). Meijsing et al. (2009) could correlate this change in chamber response to the number of electrons reaching the chamber cavity times the average path length of electrons inside the cavity. Moreover, the angular response of ionization chambers is changed in a magnetic field (Reynolds et al., 2017).
A magnetic field correction factor k_B^Q can be calculated by

$$k_B^Q = \frac{D_{w,Q}^B / M_Q^B}{D_{w,Q}/M_Q} = \frac{D_{w,Q}^B / D_{chamber,Q}^B}{D_{w,Q}/D_{chamber,Q}}, \tag{2.23}$$

assuming that the mean energy deposited in air per released charge W_{air}/e does not change in a magnetic field (O'Brien et al., 2016). For a direct measurement of magnetic field correction factors a transportable magnetic field compatible water calorimeter was designed (De Prez et al., 2016a,b).

Diodes and diamond detectors showed a considerable change in response of up to 20% for a 1.5 T perpendicular magnetic field (Reynolds et al., 2014). For relative dosimetry, ionization chamber arrays and diode arrays were found to be suitable to use in magnetic fields (Smit et al., 2014a; Houweling et al., 2016). Grafchromic$^{\mathrm{TM}}$ 2 radiochromic films exhibited a dose-dependent underresponse of up to 15% for a 0.35 T magnetic field (Reynoso et al., 2016), while the newer Gafchromic$^{\mathrm{TM}}$ 3 films were not influenced (Barten et al., 2017). The response of plastic scintillation detectors (PSDs) changed by about 7% (Stefanowicz et al., 2013), while thermoluminescent detectors (TLDs) revealed a small influence of the magnetic field strength in the order of a few percent (Mathis et al., 2014; Wang et al., 2016). Dosimetry gels that can be read-out with an MRI can be potentially used for real-time 4D dosimetry in MRgRT devices (Lee et al., 2016; Ibbott et al., 2016).

When performing dosimetry measurements in magnetic fields, also the choice of the phantom has to be reconsidered: Small air gaps close to the detector, which are inherent to plastic slab phantoms, have a substantial effect on the measurement result (Hackett et al., 2016; Agnew et al., 2017; O'Brien and Sawakuchi, 2017). Therefore, these air gaps have to be filled with water or water phantoms have to be used. A prototype magnetic field compatible scanning water phantom has already been investigated by Smit et al. (2014b).

2.4 Detectors

In this section, the detectors that were investigated in magnetic fields are described: The technical specifications of the Farmer-type ionization chambers, the MR-compatible chambers and the OSLDs are presented.

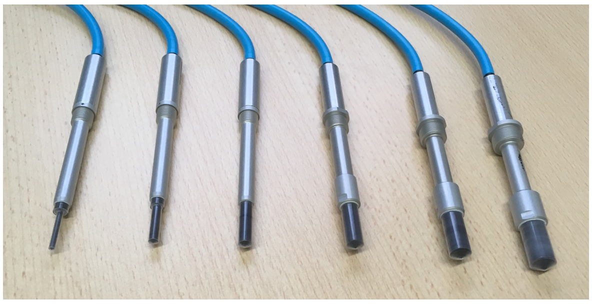

Figure 2.7: Photograph of the set of Farmer-type ionization chambers, from left to right R_1 to R_6.

2.4.1 Farmer-type ionization chambers

The behavior of six Farmer-type ionization chambers, the $PTW\,30013$ (inner radius of 3 mm, PTW, Germany) and five custom-built chambers having the same design but varying inner radius (from 1 mm to 6 mm) were investigated in magnetic fields. All chambers exhibit a cavity length of 23 mm. The chamber walls are made of a 0.335 mm thick PMMA layer coated with a 0.09 mm thick graphite layer. The central electrodes consist of aluminum and have a diameter of 1.15 mm and a length of 21.2 mm. The chamber stems are made of various layers of material including PMMA, graphite and aluminum among others (PTW, 2017; Legrand et al., 2012a,b). In the following, these chambers are denoted as R_i (where i = [1,6] corresponds to their inner radius). Figure 2.7 depicts a photograph and figure 2.8 shows µCT images (Inveon®, Siemens, Germany) of the chambers.

The EPOM of these chambers in ^{60}Co and 6 MV photon beams were investigated by Legrand et al. (2012a,b).

2.4.2 MR-compatible ionization chambers

In 2016, Standard Imaging (WI, USA) launched dedicated MR-compatible Exradin® ionization chambers for hybrid MRgRT devices. Three of these chambers were used for measurements in this project: The Farmer-type $A19MR$, the scanning $A28MR$ and the slimline miniature $A1SLMR$. Technical specifications of these chambers are summarized in table 2.3. The central electrode, guard and wall of all chambers are made of air-equivalent plastic (C552). The chamber stems consist of aluminum, teflon and polycarbonate.

A photograph of the MR-compatible chambers is shown in figure 2.9.

2.4.3 Al_2O_3:C optically stimulated luminescence detectors

In order to investigate the behavior of detectors of a higher density material, Al_2O_3:C OSLDs were used. The detectors were punched-out of a Al_2O_3:C film sheet with a diameter of 7 mm and 0.2 mm thickness. The sensitive layer of the OSLDs is made of the same powder used in the commercial Luxel® or InLight® dosimetry systems, but with a smaller grain size and a more homogeneous printing process.

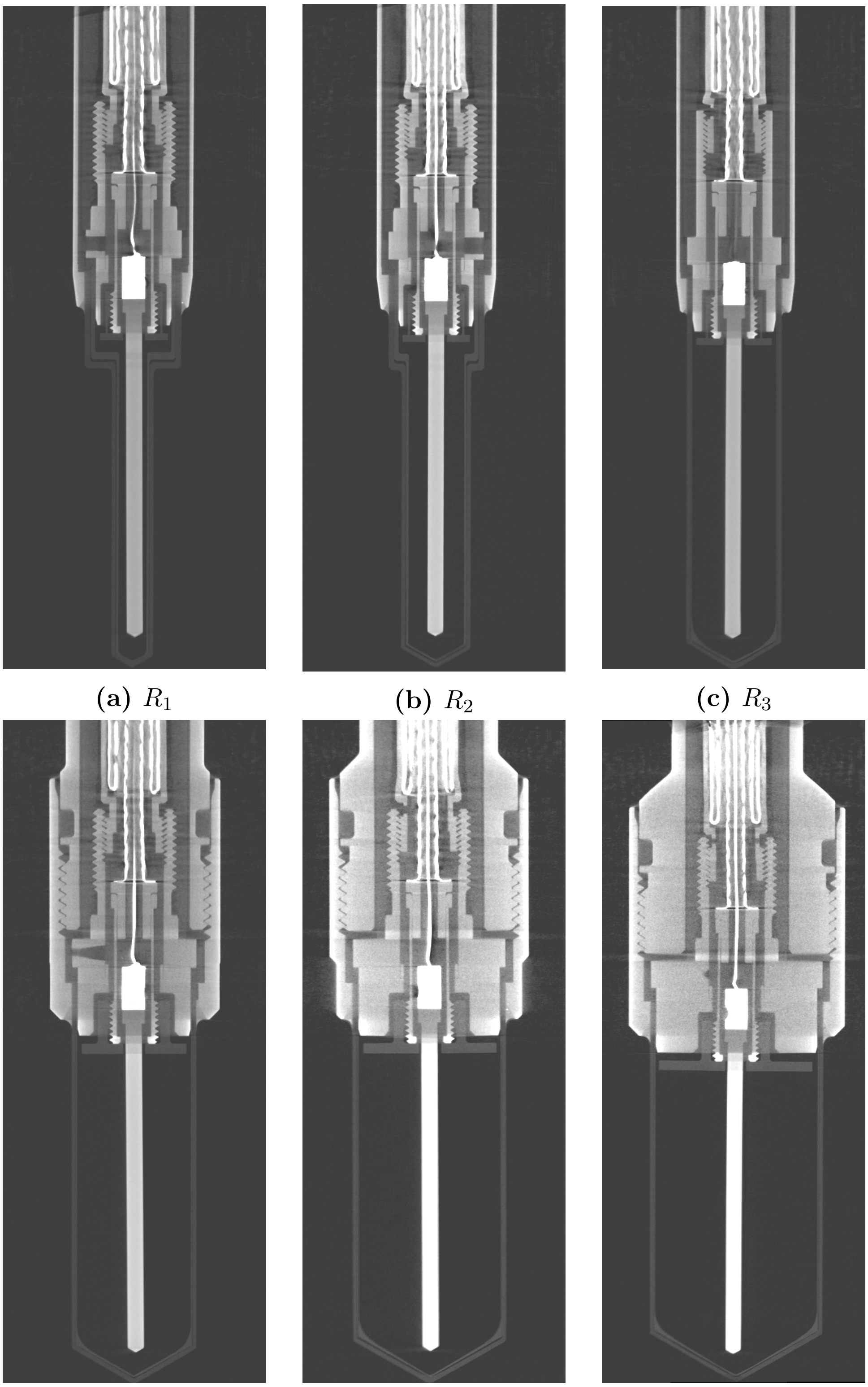

(a) R_1 **(b)** R_2 **(c)** R_3

(d) R_4 **(e)** R_5 **(f)** R_6

Figure 2.8: µCT images of the Farmer-type chambers.

Table 2.3: Technical specifications of the MR-compatible Exradin® chambers according to their data sheet (Standard Imaging, 2016).

Specifications	$A19MR$	$A28MR$	$A1SLMR$
Collecting volume [cm^3]	0.62	0.125	0.053
Outside diameter of shell [mm]	7.1	8.0	6.35
Shell wall thickness [mm]	0.5	1.1	1.1
Collector diameter [mm]	1.0	1.0	1.0
Collector length [mm]	21.6	6.4	4.4

Figure 2.9: Photograph of the MR-compatible chambers, from left to right $A19MR$, $A28MR$, $A1SLMR$.

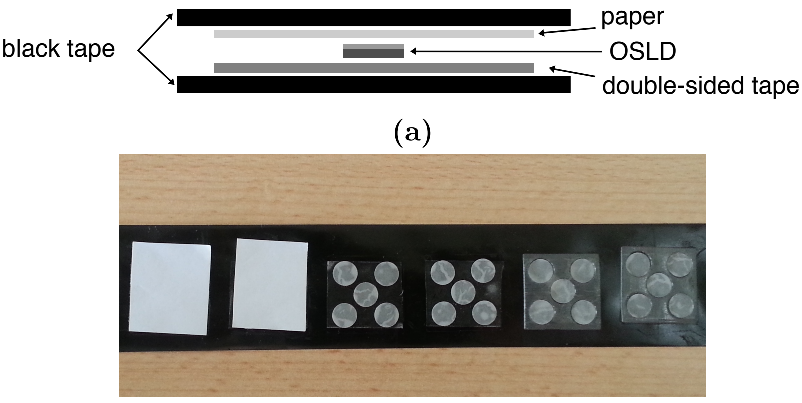

(a)

(b)

Figure 2.10: Schematic drawing and photograph of OSLD packages. Reprinted from Spindeldreier et al. (2017a).

As the detectors are light-sensitive, they were packaged in removable double-sided tape (3M Scotch Double Sided Tape, 3M Scotch, MN, USA, mass thickness (6.1 ± 0.5) mg cm^{-2}) and dark, light-proof tape (3M Scotch Super 88, 3M Scotch, MN, USA, mass thickness (28.3 ± 0.5) mg cm^{-2}). An additional paper sheet (mass thickness (8.10 ± 0.02) mg cm^{-2}) was used in front of the sensitive layer of the detectors to prevent the thin detectors from being damaged when removing the tape (see figure 2.10). It was taken care that air pockets were avoided in the detector packages, as small air gaps influence the measurement in a magnetic field. The detector shape and integrity were visually inspected.

For detector read-out, two different readers were used: The first read-out system was a portable, custom-built OSL reader (Yukihara et al., 2015). It consists of green light-emitting diodes (LEDs) (LXHL-LM5C, Philips, Lumileds, CA, USA) with long-pass glass filters (GG-495, 3 mm thickness, Schott AG, Germany). The OSL signal is separated from the stimulation light by band-pass glass filters (Hoya U-340, 1.0 cm thickness, Hoya Cooperation, Japan) and recorded with a PMT (P25PC-02, Electron Tubes Ltd., UK). The reader is able to record the main blue emission band associated with F-centers as well as the UV emission band of Al_2O_3:C (Yukihara and McKeever, 2006). In this work, the blue emission band was used for analysis, since the UV signal exhibits a time-dependence (Yukihara et al., 2015; Yukihara and McKeever, 2006).

The second reader was the automated Risø TL/OSL-DA-15 (Risø National Laboratory, Denmark) with green LEDs and a PMT (9235 QB, Electron Tubes Ltd., UK) for signal detection. A schematic drawing of this reader is shown in figure 2.11. To filter the OSL signal from the stimulation light and to block UV light, a Hoya U-340 filter (7.5 cm thickness) as well as a Schott WG-360 filter (2 mm thickness) is used. The Risø reader is equipped with a built-in ^{90}Sr/^{90}Y β-source. This source can be used to perform reference irradiations of the individual detectors after the first OSL read-out.

Thus, the ratio of the OSL signals from the first read-out and the second read-out of the reference irradiation S/S_R can be used to consider variations in detector mass and equipment sensitivity. In this way, a higher degree of precision can be achieved (Yukihara et al., 2005).

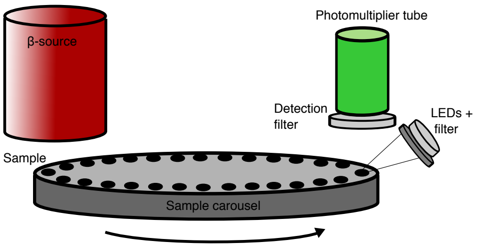

Figure 2.11: Schematic drawing of the automatic Risø reader: The OSL sample is irradiated by the LEDs and the stimulated luminescence is recorded with the PMT.

2.5 Components of the experimental set-up

The following sections describe the components used for the experiments. The technical specifications of the water tank, the electromagnet and the radiation devices are presented.

2.5.1 Water tank

The water tank (approx. 3.5 x 10 x 15 cm^3) was developed by Bakenecker (2014). The tank was printed in a 3D-printer with the material Vero Clear RGD 810 (ρ = 1.18 - 1.19 g/cm^3). It was designed to fit between the pole shoes of an electromagnet (a description of the magnet can be found in section 2.5.2).
To minimize the increase of the water temperature due to heating of the magnet, a water circulation system of 260 ml per minute was installed in the tank (see figure 2.12a). Moreover, the contact surface between tank and magnet was reduced by placing roof-shaped nubs on the outside of the tank. Heated air was carried away with a fan during the irradiations.
In accordance with the dosimetry protocol TRS-398 (Andreo et al., 2006), the detectors were placed in 10 cm water equivalent depth by means of 3D-printed holders (see figure 2.12a). The wall thickness of 5 mm was considered by density scaling (see figure 2.12b). A layer with 5 cm water equivalent thickness was used as backscatter material.

2.5.2 Electromagnet

For the generation of variable magnetic field strengths an electromagnet was used (Schwarzbeck Mess-Elektronik OHG, Germany; see figure 2.13). The magnet consists of two coils with 2000 wire windings each. The technical data specifications can be found in table 2.4. The coil wires consist of copper and the conical pole shoes are made of iron (Schwarzbeck Mess-Elektronik).

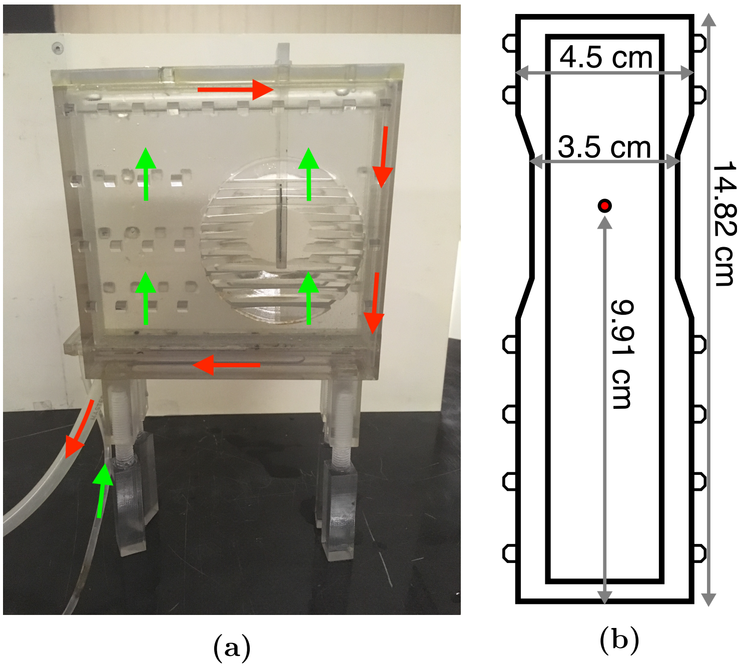

(a) (b)

Figure 2.12: (a) Picture of the water tank with an OSLD package positioned in 10 cm water equivalent depth. Due to the integrated water circulation system, the water flows from bottom to top through the tank (green arrows) and is removed via pipes in the wall (red arrows). (b) Schematic drawing of the water tank with dimensions (view from top). The red dot indicates the detector position.

Table 2.4: Technical specifications of the electromagnet (Schwarzbeck AGEM 5520) (Schwarzbeck Mess-Elektronik).

Specifications	
Number of turns	2000
Resistance at room temperature	14 Ω
Maximum coil current	20 A (1 min)
Air gap between the poles	0...95 mm
Maximum magnetic flux density	< 2.2 T
Coil diameter	335 mm
Pole diameter	30 mm - 75 mm
Total height	410 mm
Remanent flux density	typ. 5-8 mT
Weight	118 kg

The electromagnet was connected to a DC power supply (PTN 250 - 20, Heinzinger electronic GmbH, Germany), which can produce currents up to 20 A at a maximum voltage of 250 V. The maximum achievable magnetic field strength depends on the size of the air gap between the pole shoes. Consequently, a trade off between maximum magnetic field strength and radiation field size had to be taken. In this work, the distance between the pole shoes was set to 3.5 cm and therefore a maximum magnetic field strength of 1.1 T could be applied. The corresponding current values for this air gap can be found in table 2.5. A comparison of measured (hall probe CYHT201, ChenYan Technologies GmbH & Co. KG, Germany) and expected magnetic field values is shown in figure 2.14. The power supply was operated from the control room via a serial connection and a self-written software.

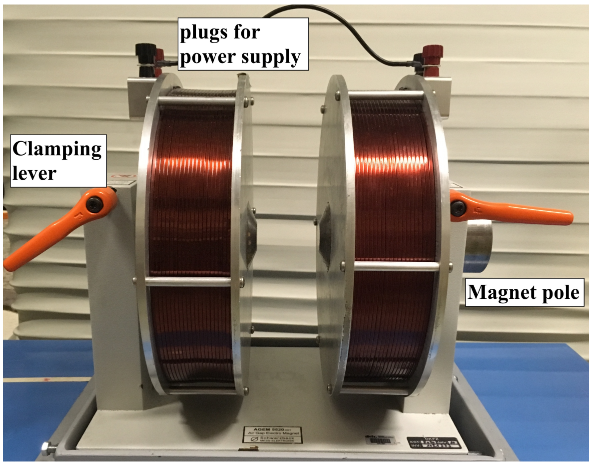

Figure 2.13: Photograph of the electromagnet.

Table 2.5: Coil current values for given magnetic field strengths at a pole shoe distance of 3.5 cm (Schwarzbeck Mess-Elektronik).

Magnetic field strength [T]	Coil current [A]
0.1	0.70
0.2	1.43
0.3	2.20
0.4	3.02
0.5	3.91
0.6	4.89
0.7	6.00
0.8	7.32
0.9	8.96
1.0	11.19
1.1	14.11

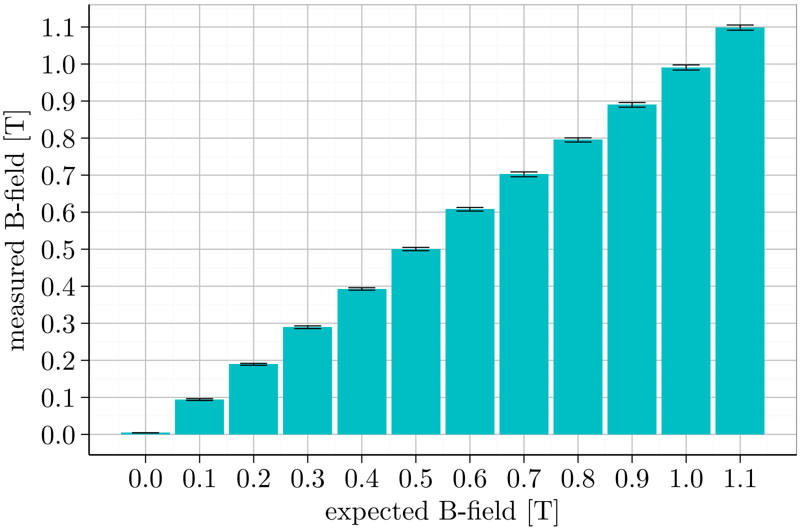

Figure 2.14: Expected and measured magnetic field strength values for the coil currents in table 2.5. The errorbars present the standard deviation of three measurements.

The field homogeneity was investigated previously by means of Finite Element Methods Magnetics simulations (Bakenecker, 2014; Meeker, 2015): At a distance of 6 mm (radius of the largest ionization chamber used) the magnetic field varied around 1% (see figure 2.15).

2.5.3 Linear accelerator

If not stated otherwise, the measurements were performed at a linac (Artíste, Siemens Medical Solutions Inc., USA). The primary electrons are produced by an electron gun and are accelerated by a high frequency field (standing wave accelerator). In the linac head the electrons are deflected by magnets and hit on a high Z target to produce bremsstrahlung photons (Schlegel and Bille, 2002).

When using the electromagnet at the linac, a maximum magnetic field strength of below 1 mT was measured at the linac head. Therefore, no interference in beam generation due to the magnetic field was assumed.

2.5.4 MRIdian Cobalt

Some experiments were performed at the MRIdian® device (ViewRay® Inc., OH, USA; site: Washington University, St. Louis). This hybrid MRgRT device is equipped with three ^{60}Co heads on a ring gantry, each with MLCs. A 0.35 T split-magnet MRI system is used for volumetric and multi-planar imaging (ViewRay, 2015). Magnetic field and radiation beam are aligned perpendicular to each other.

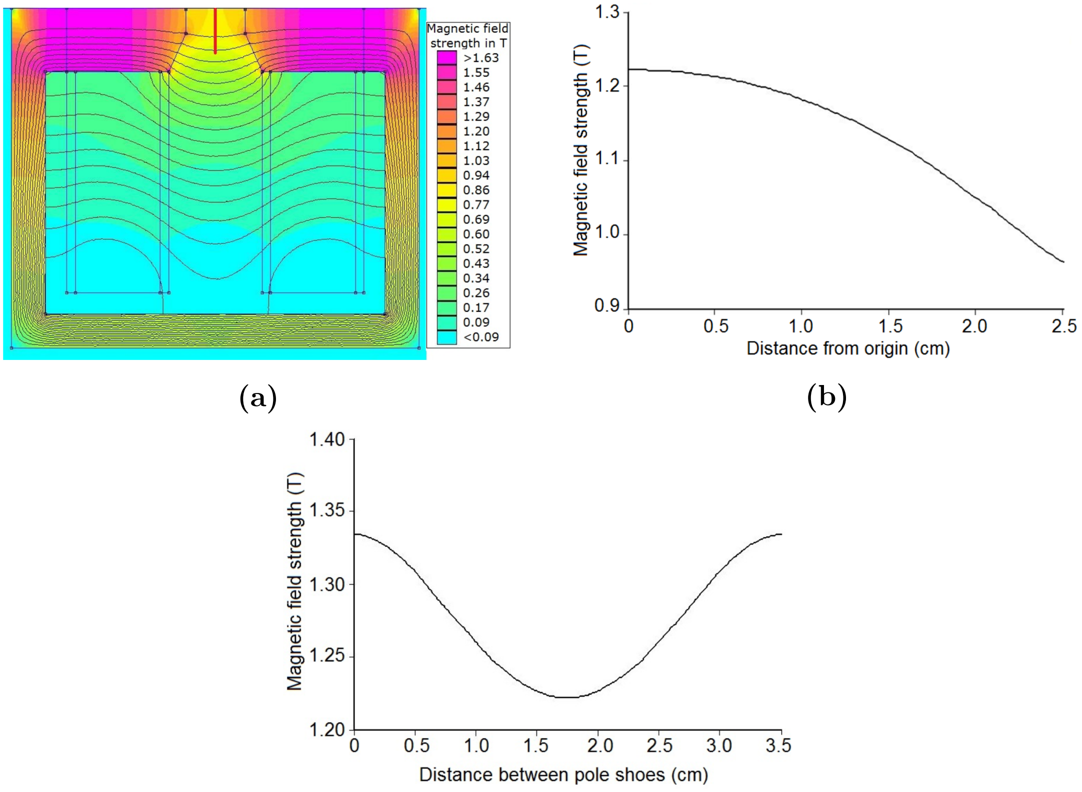

(a) **(b)**

(c)

Figure 2.15: Simulation of the magnetic field homogeneity: (a) Simulation model. (b) The magnetic field strengths between the pole shoes (along the red line in panel (a)). (c) The magnetic field strengths in the center of the pole shoes. Reprinted from Bakenecker (2014).

2.6 Monte Carlo simulation of particle transport

Generally speaking, the Monte Carlo method is a statistical sampling method for numerical integration using random numbers. First descriptions and applications of this method were presented by Comte de Buffon already in 1777 (Comte de Buffon, 1777; Kalos and Whitlock, 2008). The term Monte Carlo itself was given only in 1947 (Seco and Verhaegen, 2013).

For the Monte Carlo simulation of radiation transport, all microscopic particle interactions with matter are simulated with their corresponding probability distribution, in order to obtain a macroscopic distribution of quantities such as dose. The random particle trajectories are calculated by sampling from the probability distributions that are based on the differential cross sections of the interaction processes. According to the central limit theorem, the calculated result follows a Gaussian distribution and the uncertainty of the estimated mean σ decreases with increasing sampling size, thus number of primary particles N (Bielajew, 2001):

$$\sigma \propto 1/\sqrt{N} \tag{2.24}$$

With the help of Monte Carlo simulations, not only macroscopic quantities such as dose can be calculated and compared to measurements, but also quantities that are not accessible in measurements can be investigated, e.g. the fraction of particles entering a specific region or undergoing a certain interaction process.

In medical physics, Monte Carlo simulations are particularly used for dose calculations in treatment planning. Dose distributions in geometries with heterogeneous densities can be accurately calculated with this method, while other dose calculation algorithms based on analytical, simplified solutions face difficulties with such scenarios (Fogliata et al., 2007). Moreover, Monte Carlo simulations of clinical linear accelerators and ionization chamber measurements are frequently performed, in order to e.g. calculate correction factors for the beam quality or for small field dosimetry (Muir and Rogers, 2010; Gomà et al., 2016; Benmakhlouf et al., 2014; Crop et al., 2009; Czarnecki and Zink, 2013; Wang and Rogers, 2009). In radiology, Monte Carlo calculations of diagnostic x-ray examinations are performed, e.g. for image corrections and patient dose calculation (DeMarco et al., 2005; Chan and Doi, 1985).

2.6.1 Monte Carlo simulation software

In this thesis, the Monte Carlo simulation software EGS (Electron Gamma Shower) was used. It is a general purpose Monte Carlo code for the simulation of coupled electron-photon transport in arbitrary geometries for particles with energies above a few keV up to several hundreds of GeV (Kawrakow et al., 2017). The first version of EGS was released in the 1970s at the Stanford Linear Accelerator Center (Ford and Nelson, 1978). During the 1980s the EGS4 system was developed, which was then used for medical physics applications. The EGSnrc code system, developed at the National Research Council of Canada (NRC), is the most recent version and features many improvements, like the new implemented electron transport algorithm (Kawrakow, 2000a,b).

Several dedicated user codes are available (Rogers et al., 2017a,b; Walters et al., 2017), e.g. for stopping power calculation, calculation of fluence and particle spectra or dose calculations in arbitrary geometries, where the user can define the geometry, source and scoring quantities. All relevant photon and electron interactions (described in section 2.2) are implemented in EGSnrc. The main code is written in Mortran; in 2005 the C++ class library egs++ was released. This library allows complex geometry and source definitions (Kawrakow et al., 2009). The C++ user codes are connected to the Mortran back-end, where the physics mechanisms are implemented.

The particle transport consists of four steps:

1. The calculation of the distance to the next interaction.
2. The transport to the interaction point.
3. The selection of the interaction type.
4. The simulation of the interaction itself.

These steps are repeated until all particles have left the defined simulation geometry or until their energy is below a defined cut-off energy. If the particle energy falls below this cut-off energy (called ECUT for electrons/positrons and PCUT for photons), the particle is assumed to stop and deposits its energy locally. Prior to the simulation, cross-section tables for photon and electron interactions for all materials used in the geometry are initialized. These tables can be generated with the PEGS program, the cross section data preprocessor of EGS (Kawrakow et al., 2017).

2.6.2 Ionization chamber simulations

The accuracy of ionization chamber simulations with the EGSnrc code was shown in various publications by comparing them to measurements (Kawrakow, 2000a,b; La Russa and Rogers, 2008; Borg et al., 2000). In 2009 the user code egs_chamber dedicated to ionization chamber simulations in phantoms was released (Wulff et al., 2008b). Since the required uncertainties for ionization chamber simulations and correction factor calculations are in the order of below 1%, variance reduction techniques (VRTs) to reduce the computation time are crucial.

2.6.3 Variance reduction techniques

Due to the stochastic properties of the Monte Carlo method an inherent statistical uncertainty has to be added to the results. The uncertainty can be decreased by increasing the number of statistical independent particles (see section 2.6), but as a consequence the computation time increases as well. A quantity to assess the efficiency of the Monte Carlo calculation is defined as

$$\epsilon = \frac{1}{\sigma^2 T} \tag{2.25}$$

with σ^2 the variance of the simulation result and T the computation time required to obtain this variance. T is directly proportional to the number of simulated particles N. In order to increase the efficiency, VRTs exist that aim to decrease the time needed to reach a specific variance (Bielajew, 2001).
In the following, the VRTs implemented in the user code egs_chamber (Wulff et al., 2008b), that is used in this work, are briefly explained.

Photon splitting:
A photon is split into N photons with statistical weights of $1/N$ and a uniform distribution of interaction sites along the initial direction. The split particles contribute only with $1/N$ to the scored quantity like dose, but the probability of dose deposition is increased due to the increased number of particles (Kawrakow and Fippel, 2000).

Russian roulette:
This technique results in the opposite effect compared to photon splitting: The number of particles is reduced and hence the simulation time. If a particle survives the Russian roulette "game", its weight is increased by the inverse surviving probability and it carries the physics of all other particles that did not survive (Kawrakow et al., 2017).

Range rejection:
A charged particle is discarded whenever its kinetic energy is too small to leave the current region. Since possible bremsstrahlung is neglected, this technique is an approximation of the charged particle transport physics. The user has to define a threshold energy, below which range rejection is performed (Kawrakow et al., 2017).

Range-based Russian roulette:
In this VRT, electrons that cannot reach the ionization chamber cavity undergo a Russian roulette game with a user defined survival probability $1/N_r$. If the electron survives, its statistical weight is increased by a factor of N_r. These high weight electrons, also called "fat" electrons, may produce "fat" photons e.g. through bremsstrahlung. These are split N_r times, to avoid that fat photons reach the cavity and potentially cause large statistical variations. Range-based Russian roulette is only played with non-fat electrons. Since no approximations are needed for this technique, it is a true VRT, in contrast to range rejection (Wulff et al., 2008b).

Photon cross section enhancement:
The photon cross sections are increased by a user defined parameter. This leads to a decrease of the mean free path length of the photons and subsequently to a larger amount of electrons generated along the photon trajectory. Generally, the technique is similar to photon splitting leading to an increased amount of photon interaction sites. The enhancement factor can be set on a region-by-region basis by the user, enabling larger factors close to the chamber cavity (Wulff et al., 2008b).

Correlated sampling and intermediate phase space scoring (IPSS):
For the ionization chamber calculation of depth dose curves or profiles in a water phantom, a large amount of chamber positions inside the phantom has to be simulated. However, only a small part of the total geometry changes due to the new chamber positions. With IPSS the user can define a virtual geometry that includes all chamber positions and the phase space of all particles that enter this volume is stored. The simulations of the different chamber positions are performed subsequently, using the stored phase space as source.
The simulation of a changing geometry fraction can also be used for perturbation factor calculation, e.g. a simulation with and without central electrode. To do so, a correlated sampling scheme is used that stores not only the phase space but also the random number generator state, every time a particle enters a defined volume that surrounds the changing geometry. For the calculation of the statistical uncertainty of the dose ratio, the correlation of the two dose values, caused by using the same particles in both geometries and by using the same random numbers, needs to be considered (Wulff et al., 2008b).

2.6.4 Fano cavity test

The Fano cavity test is one of the most stringent tests of a Monte Carlo calculation (Rogers, 2006). The Fano theorem states that "in a medium of given composition exposed to a uniform flux of primary radiation (such as x-rays or neutrons), the flux of secondary radiation is also uniform and independent of the density of the medium as well as of the density variations from point to point" (Fano, 1954). Thus, in a medium which is in CPE, the electron fluence spectrum is independent of local density variations provided that the cross sections are independent of the density (Rogers, 2006). This theorem can be used to compare the simulated ionization chamber response to the expected result from the application of the Fano theorem.
The dose to the ionization chamber cavity D_{cav} irradiated by photons of energy E and fluence Φ_0 is given by

$$\frac{D_{cav}}{\Phi_0} = A_{wall} A_{fl} \left(\frac{\overline{L}}{\rho}\right)^{cav}_{wall} \left(\frac{\overline{\mu}_{en}}{\rho}\right)_{wall} E \tag{2.26}$$

with A_{wall} being the correction for attenuation and scatter in the wall, A_{fl} being the fluence perturbation correction of the cavity, $\left(\frac{\overline{L}}{\rho}\right)^{cav}_{wall}$ being the Spencer-Attix stopping power ratio and $\left(\frac{\overline{\mu}_{en}}{\rho}\right)_{wall}$ being the mass energy absorption coefficient in the wall (Kawrakow, 2000b). Using a Fano cavity, i.e. cavity and wall have identical cross sections but a difference in density of about 1000, results in $A_{fl} = \left(\frac{\overline{L}}{\rho}\right)^{cav}_{wall} = 1$. Moreover, in a Monte Carlo simulation, photon scatter and attenuation can be removed by regenerating the photon properties (energy and direction) after an interaction.

If additionally, radiation due to bremsstrahlung and atomic relaxation is discarded, this yields $A_{wall} = 1$ and $\left(\frac{\overline{\mu}_{en}}{\rho}\right)_{wall} = \left(\frac{\overline{\mu}_{tr}}{\rho}\right)_{wall}$, where $\left(\frac{\overline{\mu}_{tr}}{\rho}\right)_{wall}$ represents the mass energy transfer coefficient of the wall. Therefore, equation 2.26 simplifies to (Kawrakow, 2000b)

$$\frac{D_{cav}}{\Phi_0} = \left(\frac{\overline{\mu}_{tr}}{\rho}\right)_{wall} E. \tag{2.27}$$

The Monte Carlo calculation is usually directly normalized to the primary fluence and Φ_0 does not need to be calculated. The Fano cavity test can be considered independent of the uncertainties in cross sections, if μ_{tr} is derived from the same cross section database used for the D_{cav} calculation.

An alternative way to implement the Fano test is to circumvent the primary photons and directly simulate the secondary electrons as source. If the electron source is uniform per unit mass, i.e. it emits a constant number I of electrons per unit mass with an initial energy of E_0, the absorbed dose D is constant regardless of the local mass density variations (Sempau and Andreo, 2006):

$$D = IE_0 \tag{2.28}$$

Equations 2.27 and 2.28 can be used to test the condensed history implementation of the Monte Carlo code. Kawrakow showed that EGSnrc passes the Fano cavity test at a 0.1% level (Kawrakow, 2000b).

Fano cavity test in a magnetic field

In a magnetic field, the assumptions of the Fano cavity test as described in 2.6.4 are broken (Bouchard et al., 2015). Only with additional special conditions can a modified Fano cavity test in presence of a magnetic field be used: These additional conditions are either (1) using a source of electrons which is isotropic and uniform per unit mass or (2) applying a magnetic field of which the strength scales with the mass density of the material (Bouchard and Bielajew, 2015).

De Pooter et al. (2015) applied the first version of the Fano cavity test in presence of a magnetic field in the PENELOPE Monte Carlo code and found a limited accuracy at high energies for a 1.5 T field (deviations up to 1% for 4.0 MeV electrons), with an overall accuracy of 0.3%. Malkov et al. tested EGSnrc with a self-written magnetic field macro and obtained an agreement within 0.1% (Malkov and Rogers, 2016). The same accuracy was found for the Geant4 Monte Carlo code (O'Brien et al., 2016).

Chapter 3

Experiments and simulations

The experiments and simulations performed to investigate the different detectors in magnetic fields are described in the following sections. The results are presented in section 4 and discussed in section 5.

3.1 Validation of the Monte Carlo particle transport in magnetic fields

The Fano cavity test in magnetic fields, explained in 2.6.4, was used to test the consistency of the simulation transport including the magnetic field macro. The dose to the cavity of the R_3 simulation model was scored using the egs_chamber user code (Wulff et al., 2008b). The chamber model was placed at the center of a cylinder consisting of water, PMMA or graphite (the main materials used in ionization chambers), respectively. The chamber wall and chamber stem were set to the surrounding medium, while the cavity and the central electrode consisted of the same medium as the enclosing cylinder, but with a 1000 times smaller density (see section 2.6.4). As beam source, electrons of 1.25 MeV were used, which were distributed isotropically and uniform per unit mass.
The dose to the cavity was scored without a magnetic field and with a homogeneous magnetic field of 1.0 T and 3.0 T in -X-, -Y- and -Z-direction, respectively. The results were compared to the expected value of $D = I \cdot E_0$ (see section 2.6.4), where I is the number of electrons per unit mass and E_0 is the initial electron energy.

3.2 Measurements with ionization chambers in magnetic fields

The measurements with ionization chambers in magnetic fields were performed with the experimental set-up described in section 2.5: The water tank (details see section 2.5.1) was positioned with its surface in the isocenter of the linac with an SSD of 100 cm. The detectors were placed at 10 cm water equivalent depth with 3D-printed

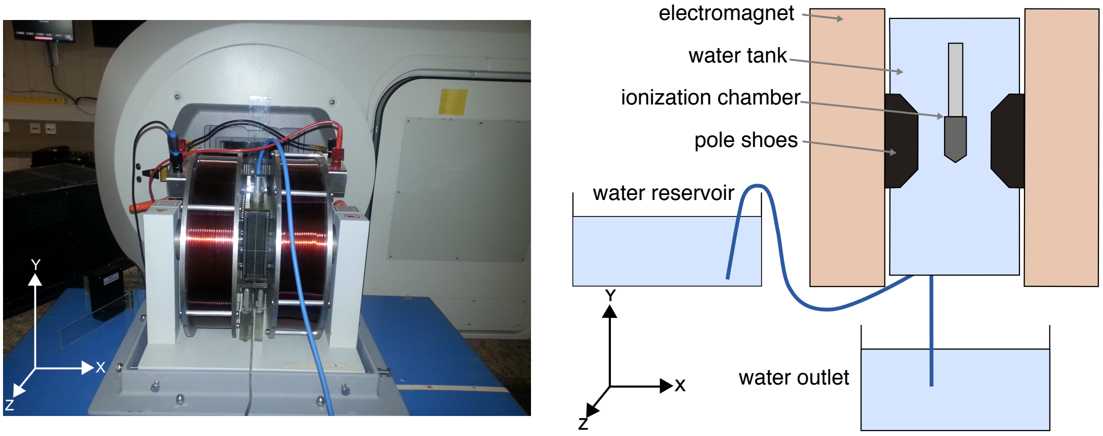

Figure 3.1: Photograph (a) and schematic drawing (b) of the experimental set-up. Reprinted from Spindeldreier et al. (2017b).

holders and irradiated with 100 MU of a horizontal beam. A flattened photon beam of 6 MV (Artíste, Siemens Medical Solutions Inc., USA) collimated to a field size of 3 x 10 cm^2 was used, in order to avoid substantial back scatter from the pole shoes of the electromagnet. Magnetic fields between 0.0 T and 1.1 T were generated with the electromagnet (described in section 2.5.2). Read-out was performed with an Unidos electrometer (PTW, Germany). A photograph and a schematic drawing of the experimental set-up is shown in figure 3.1.

3.2.1 Polarity and recombination correction

In order to perform dosimetry with ionization chambers in magnetic fields, the influence of the magnetic field on the correction factors in equation 2.22 needed to be examined. Since the temperature and pressure correction coefficient was measured before each measurement series and was independent of the magnetic field, only the polarity correction k_{pol} and the recombination correction k_s were investigated. These factors were determined for the set of Farmer-type ionization chambers R_1 to R_6 and for a magnetic field of 0.5 T in X-direction as well as without magnetic field.

The polarity correction factor is determined by

$$k_{pol} = \frac{|M_+| \ + \ |M_-|}{2M} \tag{3.1}$$

where M_+ and M_- denote the chamber readings for positive and negative polarity. In this study, the bias voltage was set to +400 V and -400 V, respectively, and the charge collected during irradiation was measured. For the recombination factor, the two-voltage-method was used and k_s was calculated by

$$k_s = a_0 + a_1 \left(\frac{M_1}{M_2}\right) + a_2 \left(\frac{M_1}{M_2}\right)^2 , \tag{3.2}$$

where the constants a_i are taken from the TRS-398 dosimetry protocol and M_1 and M_2 present the chamber readings for the bias voltages $V_1 = 400$ V and $V_2 = 100$ V.

3.2.2 Response of ionization chambers

The response curves of the Farmer-type chambers R_1 to R_6 (details see section 2.4.1) as well as of the MR-compatible $A19MR$, $A28MR$ and $A1SLMR$ (details see section 2.4.2) in magnetic fields, i.e. the signal measured in presence of a certain magnetic field relative to no magnetic field, was measured for field strengths up to 1.1 T in steps of 0.1 T. The bias voltage was set to +400 V for the PTW Farmer-type chambers and to +300 V for the Standard Imaging MR-compatible chambers. The order of magnetic field strengths was randomized, in order to minimize hysteresis effects. The direction of the magnetic field was reversed by changing the polarity of the electromagnet. Each magnetic field strength was measured three times. For the $k_{T,P}$ correction factor, temperature and pressure were determined for each measurement series (consecutive charge measurement for all magnetic field strengths of one field direction and one chamber). The temperature variations during one measurement series due to the electromagnet heating was measured exemplarily for several chambers and was included in the measurement uncertainty.

The reproducibility was tested by measuring the chamber response of the R_3 chamber three times independently on different days. Moreover, to test the influence of chamber-to-chamber variations, the response measurement was repeated with a second PTW30013 chamber (R_3 chamber).

3.3 Monte Carlo simulation of ionization chambers in magnetic fields

The EGSnrc user code egs_chamber (see section 2.6.2, Wulff et al. (2008b); Kawrakow (2000a)) was used to simulate the response of the ionization chambers in magnetic fields. The chambers were modeled with the C++ class library egs++ (Kawrakow et al., 2009). The chamber materials and dimensions were taken from data sheets provided by PTW and Standard Imaging. Additionally, µCT images (Inveon®, Siemens, Germany) of the chambers were acquired, to obtain all details, e.g. the amount of air in the chamber stem (see figure 2.8). The chamber models were placed in a 50 x 50 x 50 cm^3 water box with their reference points at 10 cm depth. A 6 MV spectrum (Mohan et al., 1985) collimated to a 3 x 10 cm^2 field was used as beam source. The SSD was set to 100 cm. Homogeneous magnetic fields between 0.0 T and 3.0 T were applied, using a customized magnetic field macro (provided by I. Kawrakow, see section 3.1 and section 4.1 for Fano cavity test results). The electron step length was set to a maximum of 0.025 times the electron gyration radius. The dose to the sensitive volume of the chambers was calculated with an uncertainty below 0.2%. For calculation time reduction, VRTs such as local photon cross-section enhancement and range-based Russian Roulette were applied (see section 2.6.3).

The maximum global energy loss of an electron step (ESTEPE) and the maximum first elastic scattering moment (XIMAX) were set to 10%. The default values for the cut-off energies (ECUT = 0.521 MeV, PCUT = 0.01 MeV) were used. Spin-off effects were not simulated.

Since no specifications on the geometry of the sensitive volume was given in the data sheets of the PTW Farmer-type chambers, the sensitive volume was simulated as the whole air volume above the guard electrode. In the data sheets of the MR-compatible chambers, the sensitive volume was exactly delineated. Consequently, the dose was only scored in these regions of the chamber air volume. The response was calculated for the Farmer-type and MR-compatible chambers for a magnetic field in ±X-direction and compared to the measurements.

3.3.1 Influence of the sensitive volume

The dose distribution within the air volume, exemplarily for the R_3 chamber, was examined in more detail. The dose scoring air volume was divided into small ring-shaped volumes (radii 0.100, 0.150, 0.200, 0.250, 0.305 cm and heights of either 0.01 cm or 0.05 cm). In an additional simulation, the ring around the reference point of the chambers was divided into six azimuthal sections. Homogeneous magnetic fields of 0.0 T, -1.0 T and +1.0 T were applied, respectively.

Since the electric field in the chambers may not be perfectly uniform, especially close to the chamber stem, a small part of the air volume may be "dead volume". Charge produced within this volume is not collected. To mimic the dead volume in the simulation, cylindrical slabs of the air volume adjacent to the guard electrode were excluded from the scoring volume. The height of the dead volume was adapted in steps of 0.01 cm, until the simulated and measured response agreed.

3.3.2 Influence of the magnetic field orientation

The response of the ionization chambers was simulated for magnetic field orientations, which could not be realized with the experimental set-up: The magnetic field in ±Y-direction (perpendicular to the beam and parallel to the chamber) and in ±Z-direction (the magnetic field parallel to the beam). The response was calculated for magnetic field strengths up to 3.0 T.

3.3.3 Magnetic field correction and perturbation factors

In order to take into account the changes in ionization chamber response, magnetic field correction factors k_B^Q (see section 2.3.4) have to be used. These factors were calculated for the six Farmer-type chambers and the MR-compatible chambers for magnetic fields up to 3.0 T in ±X-, ±Y- and ±Z-direction by

$$k_B^Q = \frac{D_{w,Q}^B / D_{chamber,Q}^B}{D_{w,Q} / D_{chamber,Q}}. \tag{3.3}$$

Moreover, the perturbation factors of the chamber stem p_{stem}, the central electrode p_{cel}, the chamber wall p_{wall} and the replacement perturbation factor p_{repl} (see equation 2.19) were determined for the six Farmer-type chambers according to the calculation scheme presented in figure 3.2.

To determine the k_B^Q correction and perturbation factors under reference conditions, the IAEA phase space of a 6 MV Primus linac with a reference radiation field of 10 x 10 cm^2 was used as beam source (Pena et al., 2007). For the calculation of the dose to water at the point of measurement, the dose was scored in a water cylinder of 1.0 cm radius and 0.025 cm height. The user code SPRRZnrc (Rogers et al., 2017a) was used to determine the averaged stopping-power ratio of water and air in a water phantom with an electron cut-off energy of 10 keV (Wulff et al., 2008a).

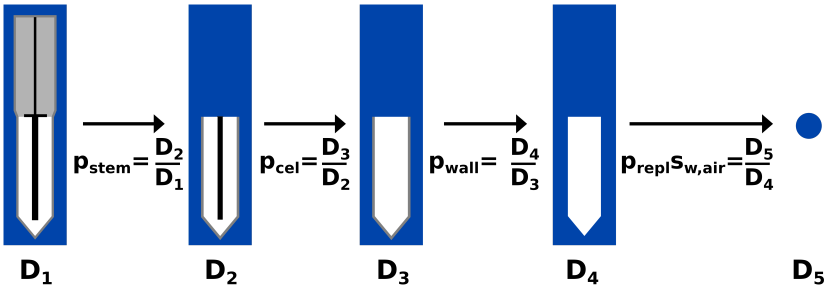

Figure 3.2: Calculation scheme of the perturbation factors of the chamber stem p_{stem}, the central electrode p_{cel}, the chamber wall p_{wall} and the replacement of water with air p_{repl}.

Influence of the spectrum

To investigate the influence of small changes in the spectrum on the k_B^Q factor, this correction factor was calculated with different 6 MV spectra (produced from the IAEA phase space files of a Siemens Primus and a Varian Clinac 600C linac (Pena et al., 2007; Brualla et al., 2009), a spectrum from an Elekta SL25 linac (Sheikh-Bagheri and Rogers, 2002) and the "reference" spectrum (Mohan et al., 1985)). The k_B^Q correction factors were exemplarily calculated for the R_3 chamber with a 10 x 10 cm^2 reference field at 10 cm depth for magnetic fields from 0.0 T to 3.0 T in ±X-direction.
Moreover, the depth-dependence of the k_B^Q factor was determined on the central beam axis for the R_3 chamber and magnetic fields in ±X-, ±Y- and ±Z-direction, calculated with the "reference" 6 MV spectrum (Mohan et al., 1985).

Influence of the magnetic field gradients

If dosimetry is performed during imaging, the local magnetic field strength at the chamber position might be slightly changed compared to the B_0 field due to the magnetic field gradients of the imaging sequences. Since field gradients reach their maximum in the order of 40 mT/m (Fallone et al., 2009) with a field of view of 50 cm (Mutic and Dempsey, 2014), a maximum change of ±10 mT at ±25 cm from the isocenter can be expected. The response, exemplarily for the R_3 chamber, in magnetic fields was calculated in a 6 MV spectrum (Mohan et al., 1985) for a change of ±10 mT in magnetic fields up to 3.0 T.

3.3.4 Effective point of measurement

The EPOM of the ionization chambers (see section 2.3.3) was determined according to the method presented by Kawrakow (2006) for the six Farmer-type chambers in magnetic fields of 0.0 T, 0.35 T, 0.5 T, 1.0 T and 1.5 T in ±X-, ±Y- and ±Z-direction. As presented in section 2.3.3, when measuring with thimble ionization chambers the dose to water at position $\vec{x}$ is related to the chamber dose by $D_w(\vec{x}) = kD_{chamber}(\vec{x}')$ (k being a series of correction factors). The EPOM shift is selected in such a way, that the overall correction factor k is as depth-independent as possible. For the determination, depth dose curves in water $D_w(z)$ with a statistical uncertainty below 0.2% and chamber depth dose curves $D_{chamber}(z_i)$ (mid-point of the chamber at z_i) with an uncertainty below 0.1% are calculated for a 10 x 10 cm^2 field generated with a 6 MV spectrum (Mohan et al., 1985) and different magnetic field strengths. The dose to water is calculated in voxels of 1.0 x 1.0 x 0.1 cm^3 with a depth resolution of 0.1 cm. The chamber doses are determined with a 0.1 cm resolution until the dose maximum and in 0.5 cm to 1.0 cm steps to a depth of 20 cm. The EPOM shift is determined by varying Δz until the ratio $D_w(z_i + \Delta z)/D_{chamber}(z_i)$ is as position independent as possible. This is achieved by minimizing

$$\chi^2 = \sum_{i=1}^{N} \frac{(f_i - k)^2}{\Delta f_i^2}, \text{ with } f_i = \frac{D_w(z_i + \Delta z)}{D_{chamber}(z_i)} \tag{3.4}$$

with respect to k and the EPOM shift Δz. N denotes the number of calculated chamber positions and Δf_i the statistical uncertainty of the f_i ratios. As presented in Kawrakow (2006), the minimization for a given Δz yields

$$k = \frac{s_1}{s_2},\ \chi^2 = s_2 - \frac{s_1^2}{s_0} \text{ with } s_n = \sum_{i=1}^{N} \frac{f_i^n}{\Delta f_i^2}. \tag{3.5}$$

By scanning over Δz, the minimum χ^2_{min} and thus the optimal Δz can be determined numerically. The uncertainty in Δz is estimated by covering the range for which $\chi^2 < \chi^2_{min} + 1$ (Tessier and Kawrakow, 2009).

The lateral EPOM can be determined in the same way, comparing the profiles calculated in water and in the chamber. Therefore, profiles in water voxels (0.1 cm resolution) and with the R_3 chamber (0.25 cm resolution in penumbra, 0.5 cm in plateau) were calculated at 10 cm depth with a statistical uncertainty of below 0.2% in the plateau region and below 0.5% in the penumbra.

3.4 Measurements with OSLDs in magnetic fields

3.4.1 Response of OSLDs

Irradiation
The response of OSLDs was investigated in high magnetic fields up to 1.0 T with the set-up described in section 3.2. The magnetic field was aligned perpendicular to the 6 MV beam and parallel to the detectors. The water tank described in section 2.5.1 and 3D-printed holders were used for this experiment. The detectors were placed in 10 cm water-equivalent depth and irradiated with 100 MU of the 3 x 10 cm^2 radiation field. Two measurements series were performed:

(i) Packages of five detectors were irradiated at varying magnetic field strengths (see figure 2.10b). Each magnetic field strength was measured three times in a randomized order. To compare the read-out with the portable reader and the Risø reader (described in section 2.4.3), the measurement was performed twice.

(ii) Only one detector in the central position was used per package. 20 irradiations per magnetic field were performed. The detectors were read-out with the automated Risø reader.

Calibration
The OSL signal increases linearly with dose in the dose range of this experiment. Thus, for the read-out with the portable reader, no conversion from OSL signal to dose was needed for the calculation of the detector response relative to 0 T.
However, for the read-out with the Risø reader a calibration curve was obtained: Because of sensitivity changes induced in the detectors, the S/S_R ratio features a saturating exponential relationship to deposited dose (Yukihara et al., 2005). The calibration curve was recorded with the in-built β-source of the Risø reader. A reference irradiation with 1 Gy of three detector packages with five detectors each was used to determine a calibration factor. Still, in the dose range of this study, the calibration curve is approximately linear.

Read-out
For the read-out with the portable reader, the pulsed-mode stimulation (POSL) was used. The detectors were stimulated for 20 s. Due to the time-dependence of the UV signal, only the blue emission band was used for further analysis (Yukihara et al., 2015; Yukihara and McKeever, 2006). Since the PMT background was in the order of 0.02% of the OSL signal, the background signal during read-out was considered negligible and no background subtraction was done.
The OSL read-out with the Risø TL/OSL-DA-15 reader was carried out in continuous-wave mode (CW-OSL). Therefore, the OSL signal S was recorded for 600 s, while stimulating the detectors. Following the first read-out, the detectors were irradiated with 2.35 Gy of the ^{90}Sr/^{90}Y source of the reader and the S_R signal was recorded with a second read-out for 600 s. In this 600 s read-out time, the OSL signal decayed completely.

For background subtraction, the last 50 data points were used. The ratio S/S_R was calculated for each detector and used for the analysis. In this way, detector and equipment sensitivity variations were considered.
The time between irradiation and read-out was in the order of 1 - 2 weeks. The read-outs were performed successively within several days, limited by the capacity of the reader. Thus, no influence of signal fading on the obtained results was expected (Bøtter-Jensen et al., 1997).

3.4.2 Angular dependence of OSLDs

For phantom measurements, the angular dependence of the OSLDs in strong magnetic fields is of interest. In order to investigate, if the magnetic field has an influence on the angular dependence, the OSLDs were rotated around their vertical axis and irradiated at five different angles ranging from 0° (detector perpendicular to beam, Al_2O_3:C-side facing beam) to 180° (see figure 3.3a), while different magnetic field strengths were applied.

The angular dependence was measured in a 6 MV beam (Siemens Artíste^{TM}, DKFZ) and a ^{60}Co beam (ViewRay MRIdian$^{®}$, Washington University).
For the 6 MV irradiations, packages of five detectors in a row (see figure 3.3b) were positioned with a rotatable 3D-printed holder in the water tank at 10 cm water equivalent depth (see section 3.2). The radiation field size of 3 x 10 cm^2 and 100 MU per irradiation were used. Magnetic fields of 0.0 T, 0.5 T and 1.0 T were applied. Each combination of detector angle and magnetic field was measured four times.
For the ^{60}Co measurement at 0.35 T, three detectors with a smaller diameter of 5 mm were irradiated at 5 cm depth in a slab phantom of Plastic Water (CNMC, TN, USA) at 100 cm SSD. A 10.5 x 10.5 cm^2 radiation field was used. The detectors were positioned with a cylindrical holder that fitted into the bore originally used for ionization chambers. The measurement was repeated three times per detector angle.

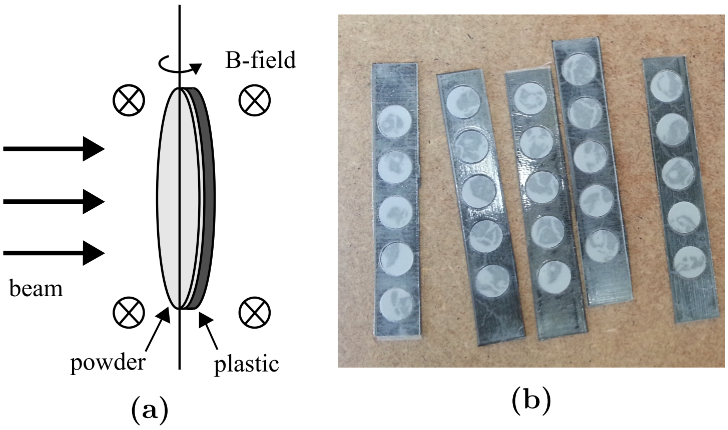

(a) (b)

Figure 3.3: Experimental set-up of the angular measurement: (a) Schematic drawing of the set-up geometry. (b) Photograph of the detector packages preparation.

3.4.3 OSLDs in a heterogeneous phantom

The OSLD response in a heterogeneous phantom in the MRIdian® MR-^{60}Co device was investigated. Three detectors were packaged in a row and positioned with plastic holders in the two bores for ionization chambers of the heterogeneous phantom (see figure 3.4a). One holder was placed in the upper part of the phantom surrounded by cork, the other holder was positioned in the center of the phantom, surrounded by polystyrene. A CT image of the phantom (with ionization chambers instead of the OSLD holders) is shown in figure 3.4b.
Three simple treatment plans were used:

(a) 2.1 x 27.3 cm^2 field, 90 s irradiation time
(b) 6.3 x 6.3 cm^2 field, 60 s irradiation time
(c) 21 x 21 cm^2 field, 60 s irradiation time

Each plan was measured five times. The dose to the phantom was calculated with the treatment planning system (TPS) system (Monte Carlo calculation with 1% accuracy) with electron density overrides of the CT at the ionization chamber positions. The OSLD doses, read-out with the Risø reader as explained in section 3.4.1, were compared to the TPS dose at the different positions. This was done by contouring the detector positions in the CT and reading the dose at this position with the software Slicer (version 4.6.2, Fedorov et al. (2012)).

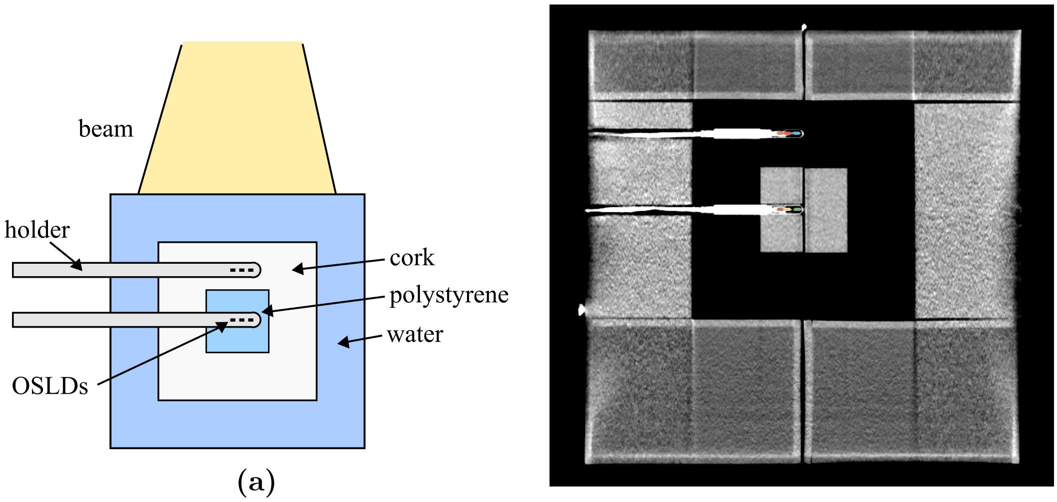

(a)

(b)

Figure 3.4: (a) Schematic drawing of the experimental set-up of the heterogeneous phantom. (b) CT image of the phantom (with ionization chambers instead of the OSL holders) with the contours of the OSLD positions.

3.5 Monte Carlo simulations of OSLDs in magnetic fields

3.5.1 Response of OSLDs

The response measurement was simulated using the simulation geometry and parameters described in section 3.3. The detectors were modelled as a 47 µm thick layer of Al_2O_3 and a 75 µm thick layer of PMMA in a water phantom at 10 cm depth. A 6 MV beam spectrum (Mohan et al., 1985) collimated to 3 x 10 cm^2 field size was used as beam source. The dose to Al_2O_3 was scored for homogeneous magnetic fields up to 1.0 T perpendicular to the beam and compared to the measurements.

3.5.2 Magnetic field correction factors for OSLDs

To correct the detector response in magnetic fields (calibrated without magnetic field), k_B^Q factors can be used, as explained in section 2.3.4. These factors were calculated by means of Monte Carlo simulations. The 10 x 10 cm^2 phase space of a Primus linac (Pena et al., 2007) was used. The dose to the detector and the dose to a small water cylinder in 10 cm depth (1 cm radius, 0.025 cm height) were scored for magnetic fields up to 3.0 T perpendicular (X-direction) and parallel (Z-direction) to the beam.

3.5.3 Angular dependence of OSLDs

The angular dependence was simulated with the detector model and beam source described in section 3.4.1. Homogeneous magnetic fields of 0.0 T, 0.35 T, 0.5 T and 1.0 T were applied. As in the experiment, the detector was rotated around its vertical axis in steps of 45° at 10 cm depth in a water phantom.

Chapter 4

Results

4.1 Validation of the Monte Carlo particle transport in magnetic fields

Figure 4.1 shows the deviation from the expected value of $D = I \cdot E_0$ from the Fano cavity test (see section 2.6.4) for the simulations in water, PMMA and graphite. For all magnetic field strengths and orientations investigated, the simulated results agree to within 0.13% with the expected value. It can be concluded that the magnetic field macro does not perturb the consistency of the simulations.

4.2 Measurements with ionization chambers in magnetic fields

4.2.1 Polarity and recombination correction

The polarity and recombination correction factors for the Farmer-type chambers without magnetic field and in presence of a 0.5 T magnetic field are presented in tables 4.1 and 4.2. No substantial changes in the correction factors can be observed and thus the influence of the magnetic field on both correction factors can be considered negligible.

Table 4.1: The polarity correction factor k_{pol} of the six Farmer-type chambers without magnetic field and with a magnetic field of 0.5 T. The uncertainty is in the order of ±0.002.

B-field	R_1	R_2	R_3	R_4	R_5	R_6
0.0 T	1.003	1.000	1.000	1.000	0.999	1.001
0.5 T	1.003	1.001	0.998	1.000	0.999	1.000

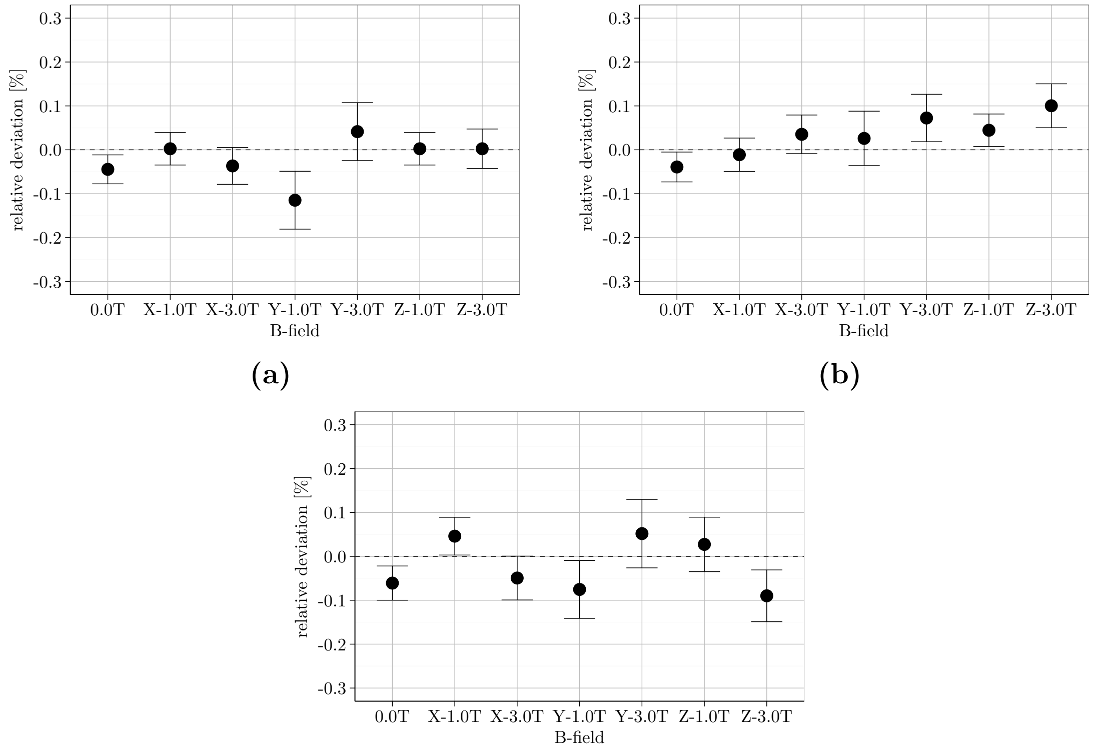

(a) **(b)**

(c)

Figure 4.1: Fano cavity test results showing the deviation from the expected value of $D = I \cdot E_0$ for the geometry with water (a), PMMA (b) and graphite (c). Reprinted from Spindeldreier et al. (2017b).

Table 4.2: The recombination correction factor k_s of the six Farmer-type chambers without magnetic field and with a magnetic field of 0.5 T. The uncertainty is in the order of ±0.002.

B-field	R_1	R_2	R_3	R_4	R_5	R_6
0.0 T	1.003	1.001	1.001	1.003	1.004	1.007
0.5 T	1.003	1.001	1.003	1.004	1.005	1.008

4.2.2 Response of ionization chambers

Farmer-type chambers

Figure 4.2 shows the relative signal in presence of the magnetic field normalized to the signal without magnetic field for the six Farmer-type chambers and both magnetic field orientations perpendicular to the beam and the chamber axis (±X-direction). A complex dependency of the chamber response on the magnetic field strength, the chamber radius and the orientation of the magnetic field can be observed. In the measured range of magnetic fields, the relative signal increases up to a certain field strength and subsequently decreases for all chambers except the small R_1 and R_2 chambers. The maximum increase in response is observed for the R_4 chamber at 0.9 T (8.8%) in +X-direction and for the R_3 chamber at 1.0 T (7.0%) in -X-direction. Reversing the magnetic field orientation causes only a minor change in response for the small chambers (R_1 to R_3, around 1%), while it changes the response of the large R_6 chamber by up to 6%. Moreover, the magnetic field strength of the maximum response decreases for larger chamber radii.

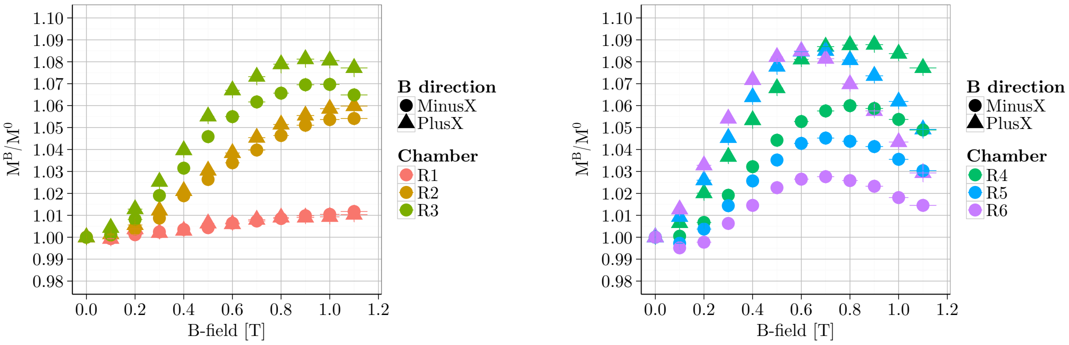

Figure 4.2: The response of the six Farmer-type ionization chambers in magnetic fields up to 1.1 T in ±X-direction. The errorbars represent the measurement uncertainties (standard deviation of three measurements plus the uncertainty for temperature, pressure and reading). The horizontal errorbars depict the uncertainty of the magnetic field strength. Reprinted from Spindeldreier et al. (2017b).

The results of the reproducibility of the R_3 response is presented in figure 4.3a. The three response curves measured on different days agree very well. A root mean square difference of 0.1% between the three measurement series is obtained with a maximum difference of 0.3%. Therefore, a very good reproducibility is achieved.

Figure 4.3b shows the comparison of a measurement with the R_3 chamber and a second $PTW30013$ Farmer-type chamber. The root mean square difference between the two measurement series is 0.3% with a maximum difference of 0.8%. The response of the two chambers of the same type differs slightly, which can be explained by differences in the dead volume of the chambers (see section 3.3.1).

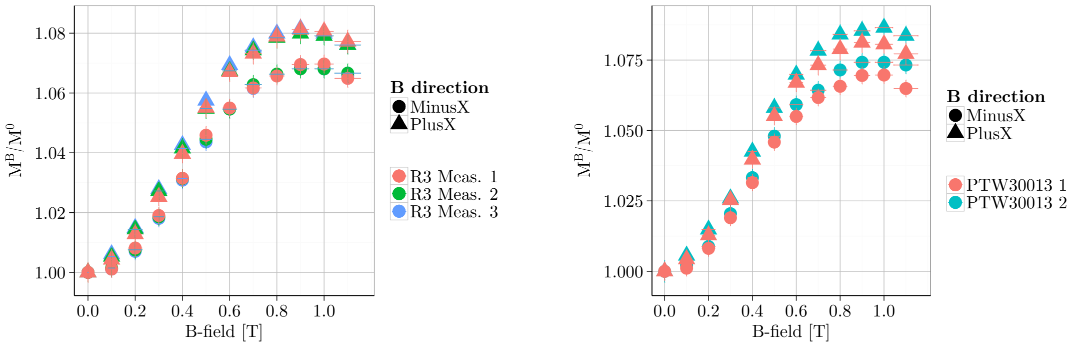

(a) **(b)**

Figure 4.3: (a) Reproducibility of the response measurement: Comparison of three measurements of the R_3 response in magnetic fields on different days. (b) Comparison of the response in a magnetic field of two $PTW30013$ ionization chambers.

MR-compatible chambers

The measured response of the MR-compatible chambers in magnetic fields is displayed in figure 4.4. The response of the Farmer-type $A19MR$ rises for both field directions to a maximum (+8.4% for 0.9 T in +X, +6.6% for 0.9 T in -X-direction). For the $A1SLMR$ and the two $A28MR$, the response describes a maximum for a field in +X-direction and a minimum for a field in -X-direction. The response of the $A1SLMR$ increases by +3.7% at +1.1 T and decreases by -1.1% at -0.5 T. For the two $A28MR$, the responses rise up to +6.8% at +0.9 T, while they decrease maximally by -3.0% at -0.6 T.

4.3 Monte Carlo simulation of ionization chambers in magnetic fields

Farmer-type chambers

Figure 4.5 shows the measured response of the six Farmer-type chambers compared to the simulated response, when the whole air volume below the guard electrode is considered to be part of the sensitive volume. A large disagreement between simulation and measurement results was obtained: Contrary to the measurement, the response increase in the simulation is slightly higher in the -X-direction than in the +X-direction. Additionally, the large difference in the measured response for the two magnetic field orientations could not be reproduced by the simulations.

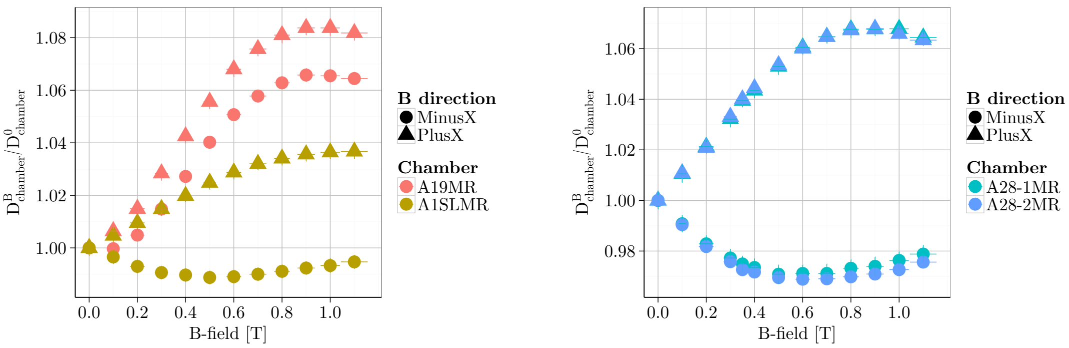

Figure 4.4: The response of the MR-compatible ionization chambers *A*19*MR* and *A*1*SLMR* (Shukla, 2017) (a) and the two *A*28*MR* chambers (b) in magnetic fields up to 1.1 T in ±X-direction. The errorbars represent the measurement uncertainties (standard deviation of three measurements plus the uncertainty for temperature, pressure and reading). The horizontal errorbars depict the uncertainty of the magnetic field strength.

Small volumes at the guard electrode are suspected to act as dead volumes due the electric field distribution in the chamber, i.e. charge that is produced in these volumes is not collected by the central electrode but e.g. by the guard electrode. The influence of these dead volumes is investigated in detail in the following section 4.3.1. By adjusting the thickness of the dead volume of all six Farmer-type chambers, the simulation results could be adapted to the measurements. The resulting response curves are depicted in figure 4.6. The thicknesses of the dead volumes are 0.08 cm, 0.09 cm, 0.11 cm, 0.19 cm, 0.22 cm and 0.26 cm for the chambers R_1 to R_6, respectively. When comparing measurement and simulation, a root mean squared deviation of only 0.2% and a maximum deviation of 0.9% at 1.1 T in +X-direction for the R_4 chamber was found.

MR-compatible chambers

In the technical drawings of the MR-compatible chambers, dead volumes are explicitly delineated. Therefore, no manual adaptation of the sensitive volume to the measurement needed to be performed as described in the above section. The comparison of measured and simulated response for magnetic fields up to 1.1 T in ±X-direction is shown in figure 4.7. For the *A*19*MR* and the *A*1*SLMR* chambers a very good agreement between measurement and simulation with a root mean square difference below 0.3% and below 0.2% (maximum difference of -0.5% at +0.1 T and +0.3% at -1.0 T) is obtained, respectively. The simulated responses of the *A*28*MR* chambers differ maximally by +0.6% (at -1.1 T) and +0.4% (at +0.5 T) from the measured response of the two chambers, with a root mean square difference of below 0.3% and below 0.2%.

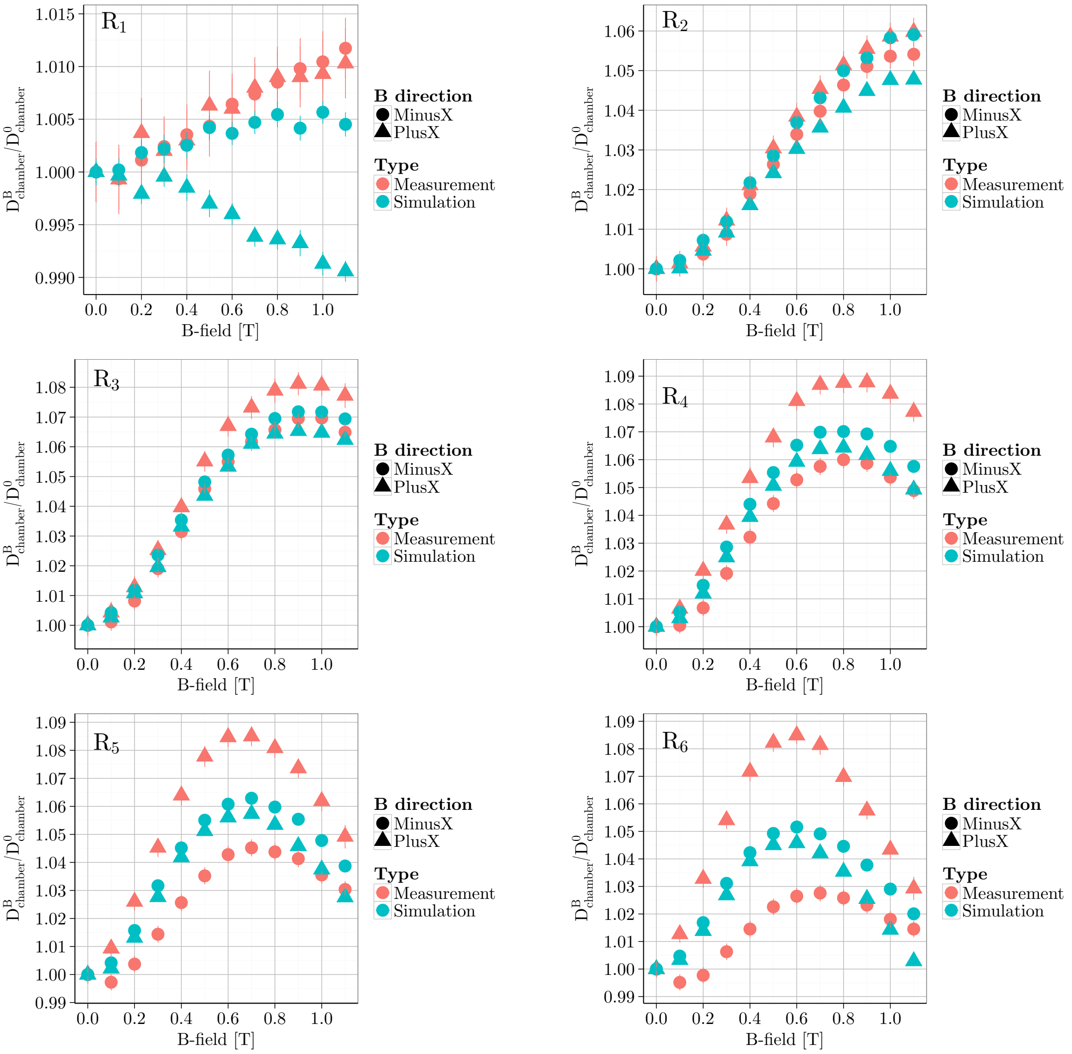

Figure 4.5: Measured and simulated response of the six Farmer-type chambers in magnetic fields in ±X-direction, when the whole air volume below the guard electrode is considered to be part of the sensitive volume. Reprinted from Spindeldreier et al. (2017b).

4.3.1 Influence of the sensitive volume

The influence of dead volumes was investigated by simulating the spatial dose distribution in the air volume of the R_3 chamber. Figure 4.8 shows the result for magnetic fields of 0.0 T, -1.0 T and +1.0 T in X-direction. The spatial dose maps integrated over the azimuthal angle are depicted in figures 4.8a, 4.8b, 4.8c. The statistical uncertainty in the scoring regions is below 0.4%. Without magnetic field, the dose distribution is nearly homogeneous. For a -1.0 T magnetic field, hot spots of up to +35% and cold spots of -20% relative to the mean dose without magnetic field arise at the guard electrode and the chamber tip. These hot and cold spots are caused by the electron deflection towards the chamber stem due to the Lorentz force. For a +1.0 T magnetic field the opposite effect occurs leading to low dose regions at the guard electrode and high dose regions at the chamber tip.

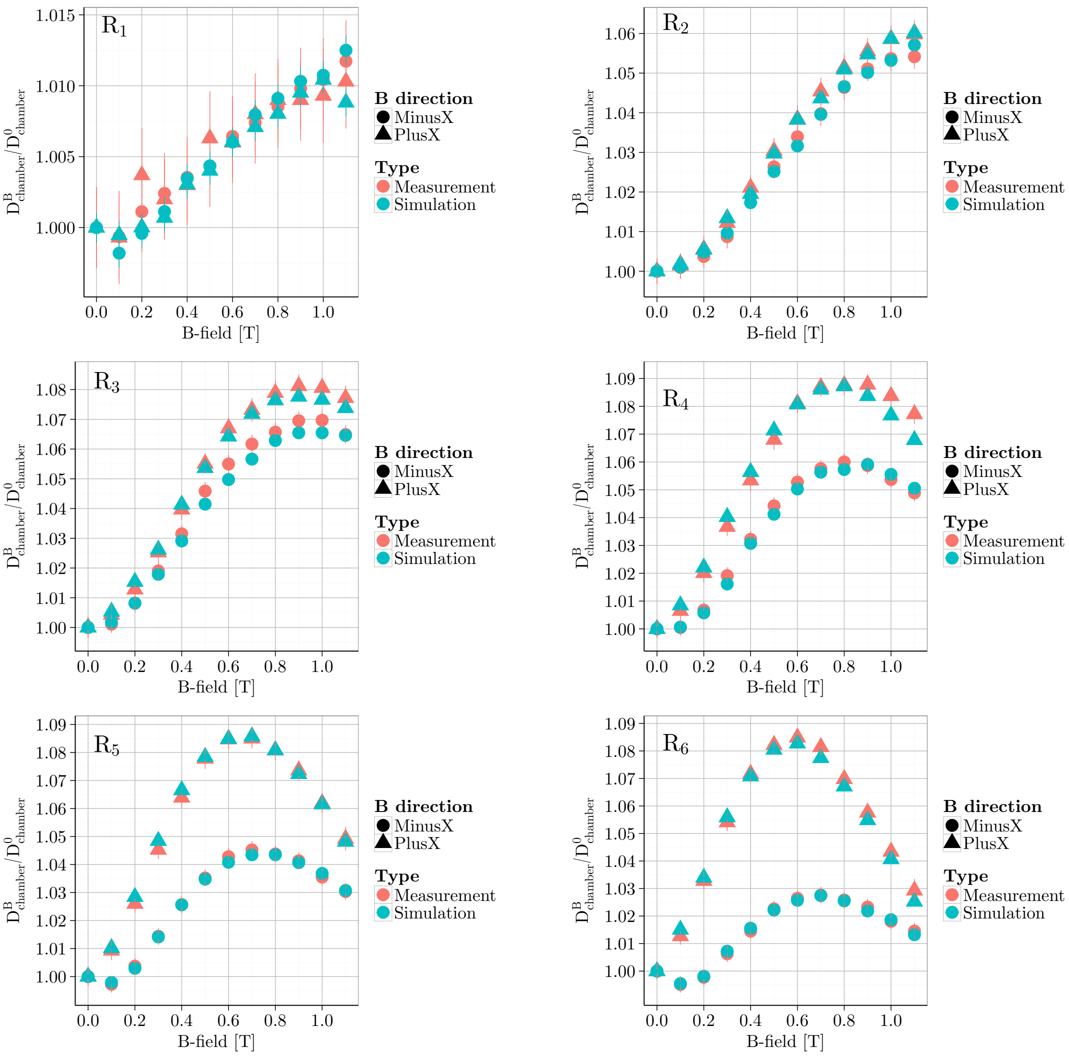

Figure 4.6: Measured and simulated response of the six Farmer-type chambers in magnetic fields in ±X-direction with the adapted sensitive volumes considering a cylindrical dead volume adjacent to the guard electrode. Reprinted from Spindeldreier et al. (2017b).

The dose distributions in the transversal plane at the reference point discritized in azimuthal segments are displayed in figures 4.8d, 4.8e, 4.8f. The statistical uncertainty in the scoring regions is below 0.7%. If no magnetic field is applied, the dose distribution is again rather homogeneous. A small dose decrease behind the central electrode at the beam exit side is visible. With magnetic field, the dose at the beam entrance side is increased by up to +35%, while dose cold spots of -26% are visible at the beam exit side. This dose concentration in the first half of the chamber is caused by the lateral deflection of the secondary electrons by the Lorentz force.

Due to the inhomogeneous dose distribution close to the guard electrode, an exclusion of a small air volume from the sensitive scoring volume - the dead volume - may lead to a substantial change in the calculated response in magnetic fields.

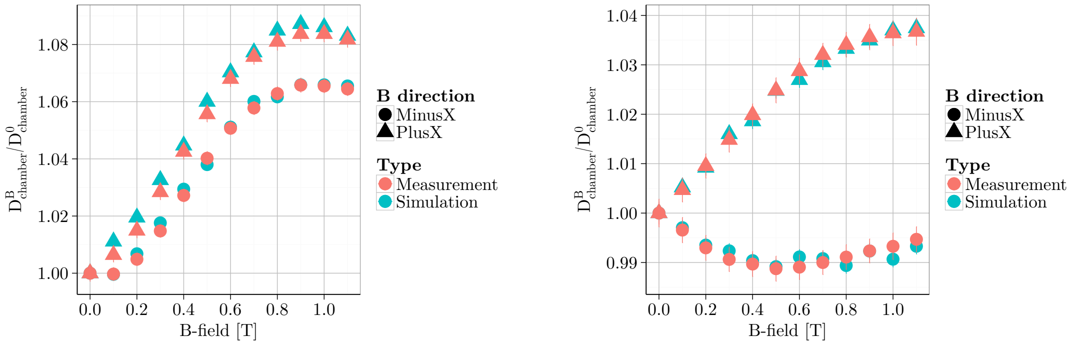

(a) *A*19*MR* **(b)** *A*1*SLMR*

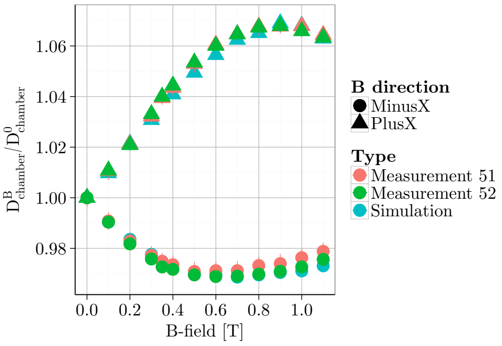

(c) *A*28*MR*

Figure 4.7: Measured and simulated response of the MR-compatible chambers (a) *A*19*MR*, (b) *A*1*SLMR* (Shukla, 2017) and (c) *A*28*MR* in magnetic fields in ±X-direction.

The influence of cylindrical dead volumes of different thicknesses at the guard electrode on the response of the R_3 chamber is shown in figure 4.9. For an increasing dead volume thickness, the response curves for the magnetic fields in +X- and -X-direction grow apart. The response curve for the +X magnetic field increases with larger dead volumes, because the low dose region at the guard electrode is excluded. In contrast, the high dose region is excluded for the -X magnetic field, leading to a decrease in the response for larger dead volumes.

4.3.2 Influence of the magnetic field orientation

Farmer-type chambers

The response of the six Farmer-type chambers for magnetic fields in ±Y- (parallel to the chamber axis and perpendicular to the beam) and ±Z-direction (parallel to the beam) is shown in figure 4.10. For the ±Y magnetic field, the response increases up to +1.3% at 3.0 T for the small R_1 and R_2 chambers, while it increases up to a certain magnetic field and decreases again for larger chambers. The magnitude and position of the maximum response decrease with increasing chamber radius. For the R_6 chamber the maximum response of +0.3% can be found at 0.7 T. Reversing the magnetic field orientation in Y-direction has no substantial influence on the response.

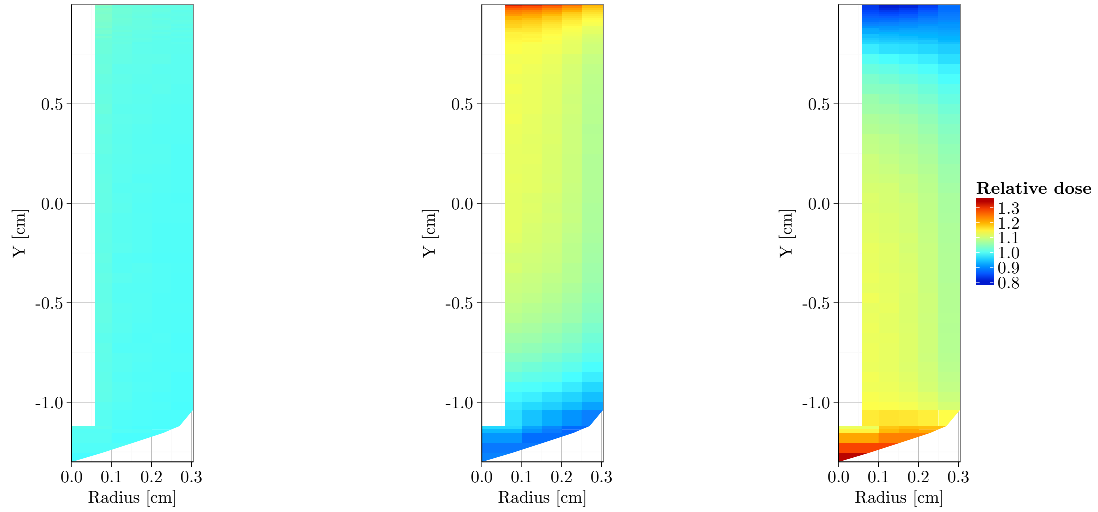

(a) 0.0 T **(b)** -1.0 T **(c)** +1.0 T

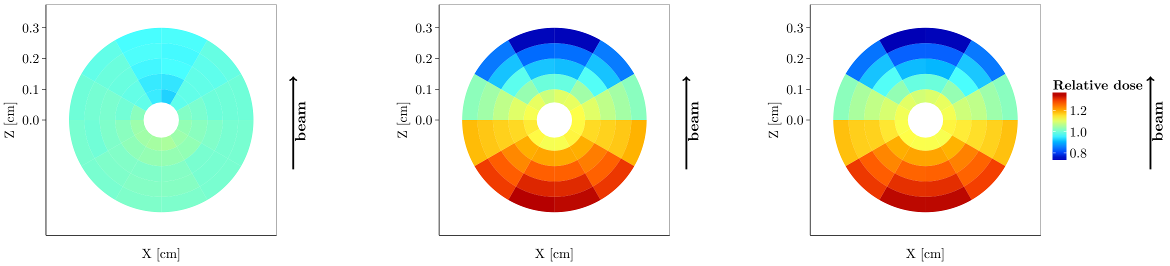

(d) 0.0 T **(e)** -1.0 T **(f)** +1.0 T

Figure 4.8: Spatial dose distributions of the R_3 chamber for magnetic fields of 0.0 T, -1.0 T and +1.0 T in X-direction. Panels (a)-(c) display the dose integrated over azimuthal rings around the chamber axis, panels (d)-(f) show the dose scored in azimuthal sections around the reference point (located at Y = 0 in panels (a)-(c)). The doses are normalized to the mean dose for 0.0 T. Reprinted from Spindeldreier et al. (2017b).

For a magnetic field in ±Z-direction, a monotonous increase of the response for all chambers with increasing magnetic field strengths can be observed. The chamber response increases by around 0.5% for the R_1 and by +1.0% for the R_6 chamber at 1.0 T. Reversing the magnetic field orientation in Z-direction, again has no influence on the response.

The dose distributions within the air volume of the R_3 chamber for a 0.0 T and a ±1.0 T magnetic field in Y- and Z-direction are depicted in figures 4.11 and 4.12. In the longitudinal plane, the magnetic fields cause only a small dose increase near the central electrode, independent of the field orientation. The dose distribution in the transversal plane is perturbed according to Lorentz force. For a ±Y magnetic field, hot (up to +34%) and cold dose regions (down to -39%) arise at the ±X sides of the chamber, since the Lorentz force points in ±X-direction for electrons traveling along the beam direction. For a ±Z magnetic field, a dose increase of up to +9% at the beam entrance side can be observed.

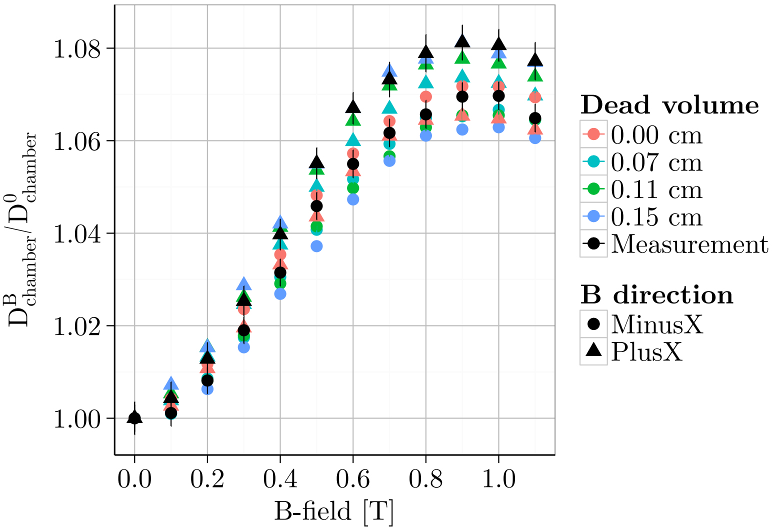

Figure 4.9: Response of the R_3 chamber simulated for different thicknesses of the dead volume and magnetic fields in ±X-direction. Reprinted from Spindeldreier et al. (2017b).

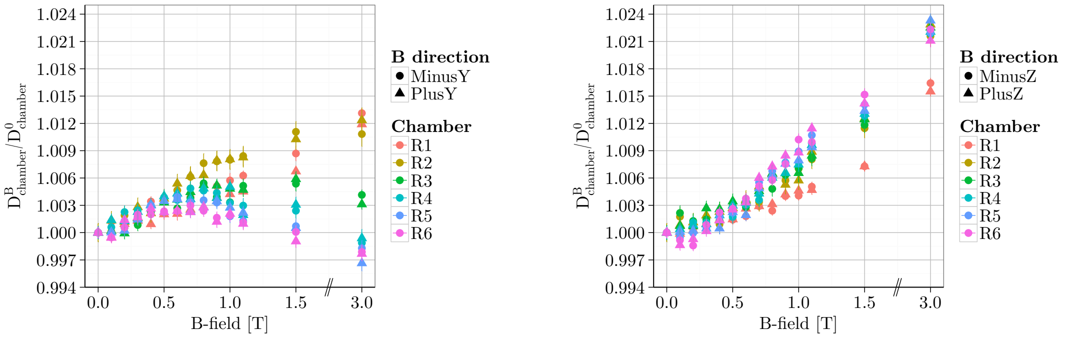

(a) Y B-field.

(b) Z B-field.

Figure 4.10: Simulated response of the Farmer-type chambers for magnetic fields in (a) ±Y- and (b) ±Z direction. Reprinted from Spindeldreier et al. (2017b).

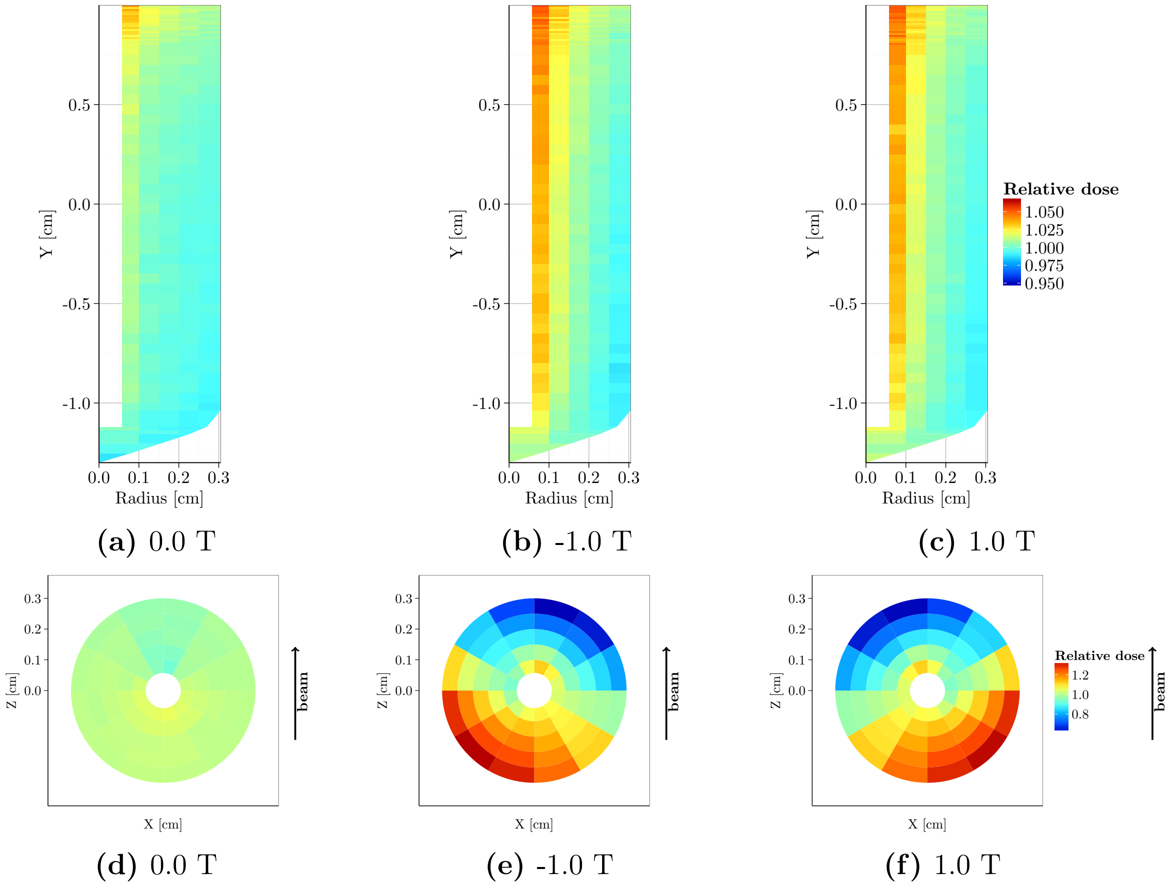

Figure 4.11: Spatial dose distributions of the R_3 chamber for magnetic fields of 0.0 T, -1.0 T and +1.0 T in Y-direction. Panels (a)-(c) display the dose integrated over azimuthal rings around the chamber axis, panels (d)-(f) show the dose scored in azimuthal sections around the reference point (located at Y = 0 in panels (a)-(c)). The doses are normalized to the mean dose for 0.0 T. Reprinted from Spindeldreier et al. (2017b).

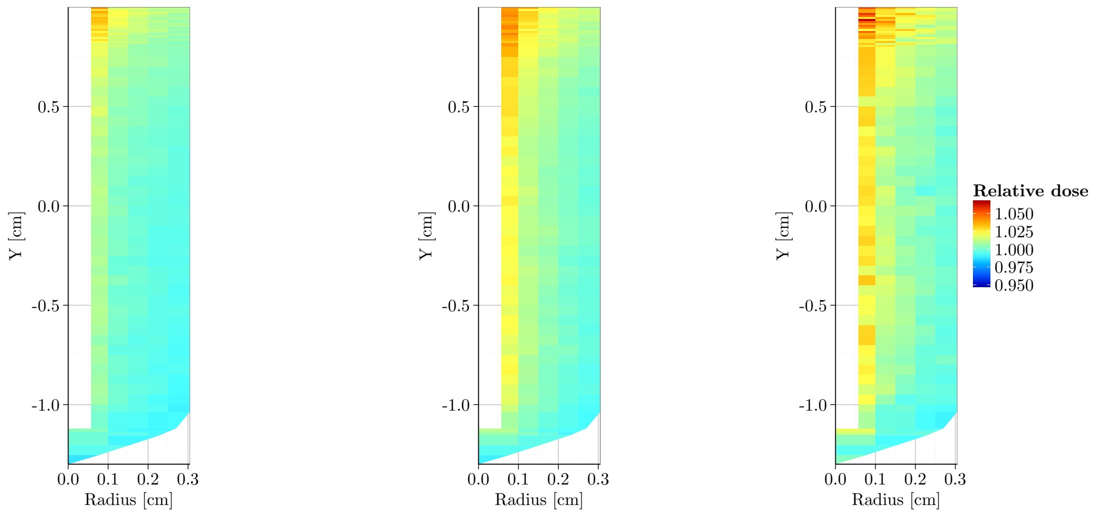

(a) 0.0 T **(b)** -1.0 T **(c)** 1.0 T

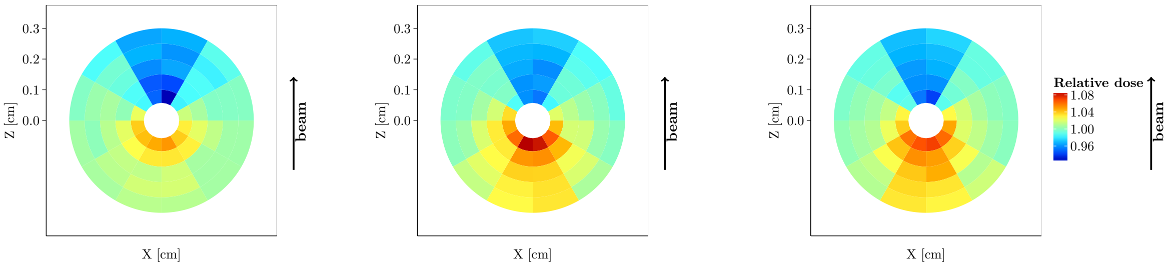

(d) 0.0 T **(e)** -1.0 T **(f)** 1.0 T

Figure 4.12: Spatial dose distributions of the R_3 chamber for magnetic fields of 0.0 T, -1.0 T and +1.0 T in Z-direction. Panels (a)-(c) display the dose integrated over azimuthal rings around the chamber axis, panels (d)-(f) show the dose scored in azimuthal sections around the reference point (located at Y = 0 in panels (a)-(c)). The doses are normalized to the mean dose for 0.0 T. Reprinted from Spindeldreier et al. (2017b).

MR-compatible chambers

For the MR-compatible chambers, the chamber response decreases with increasing magnetic field in ±Y-direction (see figure 4.13a). No substantial influence of the field orientation on the response curves can be observed. The larger the air volume of the chamber (the length of the cavity), the larger is the decrease in response. For a 3.0 T magnetic field in Y-direction, the response is reduced by -0.5%, -0.9% and -1.2% for the $A1SLMR$, $A28MR$ and $A19MR$ chamber, respectively.
For a magnetic field parallel to the beam (in ±Z-direction), the chamber response rises monotonously with increasing magnetic field strength. Again, no dependence of the field orientation on the chamber response can be found. The largest response increase occurs for the largest chamber ($A19MR$) with 1.6% at 3.0 T, while the smaller $A28MR$ and $A1SLMR$ chambers exhibit an increase of 1.4% and 1.0% at the same field strength, respectively.

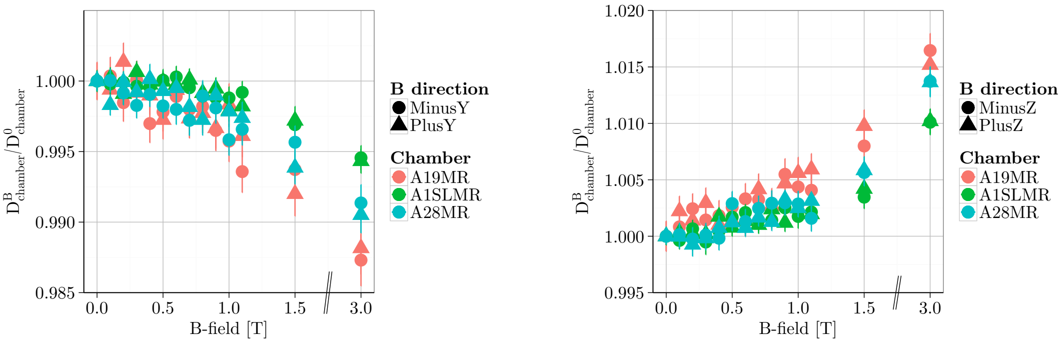

(a) Y B-field. **(b)** Z B-field.

Figure 4.13: Simulated response of the MR-compatible chambers for magnetic fields in (a) ±Y- and (b) ±Z direction.

4.3.3 Magnetic field correction and perturbation factors

Farmer-type chambers

Figure 4.14 shows the k_B^Q magnetic field correction factors for magnetic fields in ±X-, ±Y- and ±Z-direction. The k_B^Q factors resemble approximately the inverse shape of the response curves, since the dose to water changes only slightly with varying magnetic field. For a 1.0 T magnetic field in ±X-direction, it decreases by around -0.3%, for a magnetic field in ±Y-direction, it decreases by -0.2% and for a field in ±Z-direction, it rises by +0.1%.

For a ±X magnetic field, k_B^Q decreases until a certain magnetic field strength depending on the chamber radius and increases for higher field strengths. The R_4 chamber revealed the maximum change of -7.6% at +0.8 T. With a magnetic field in ±Y-direction, the k_B^Q factor again describes a minimum depending on the chamber radius. The smaller the chamber radius, the larger is the decrease: For the R_1 chamber k_B^Q

decreases by -2.5% at 3.0 T, for the R_6 chamber it decreases by -0.5% at 0.7 T and rises again for higher field strengths. A magnetic field in ±Z-direction leads to a decrease in k_B^Q with increasing field strength (about -0.8% at 1.0 T) with a minor influence of the chamber radius.

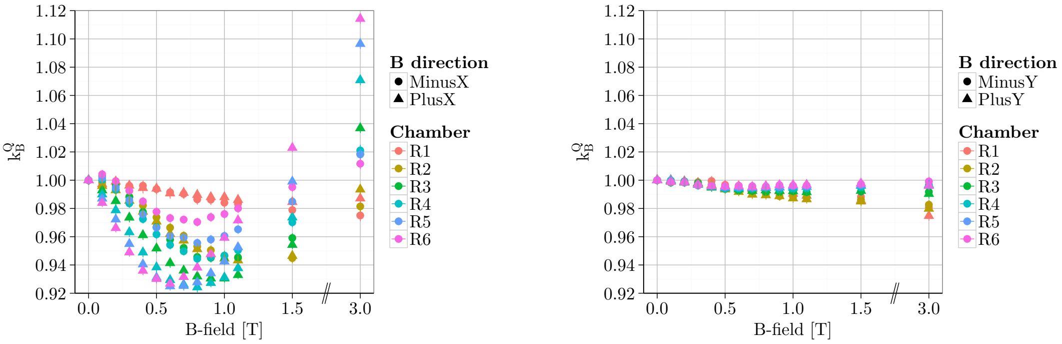

(a) X B-field.   **(b)** Y B-field.

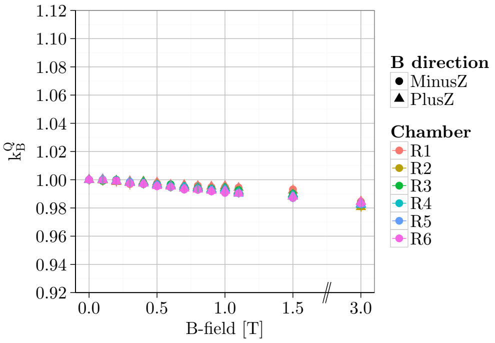

(c) Z B-field.

Figure 4.14: Calculated magnetic field correction factors k_B^Q of the six Farmer-type chambers and magnetic fields in (a) ±X- (b) ±Y- and (c) ±Z direction. Reprinted from Spindeldreier et al. (2017b).

The perturbation factors p_{stem}, p_{cel}, p_{wall} and p_{repl} of the six Farmer-type chambers and all three magnetic field directions are presented in figures 4.15 and 4.16. The chamber radius has an influence on all perturbation factors, but only for a magnetic field in X-direction a dependence on the field orientation can be observed.

The p_{stem} perturbation factor increases for a ±X magnetic field towards higher field strengths. This increase is larger for the +X-direction, because electrons in the water region that replaces the stem are bent into the cavity and deposit additional dose. The p_{stem} factors of the small R_1 and R_2 chambers are slightly shifted compared to the other chambers, which might be due to small changes in their chamber stems, which were made to fit the small cavities. A maximum increase in p_{stem} is found for the R_6 chamber with +0.7% at 1.1 T in +X-direction. With a magnetic field in ±Y-direction, p_{stem} decreases for the R_1, R_2 and R_3 chambers (by -0.7% at 3.0 T for the R_2 chamber at maximum) and increases monotonically for the larger chambers (by 0.9% at 3.0 T for the R_6 chamber at maximum). For a magnetic field in ±Z-direction, p_{stem} tends towards unity for high field strengths and all chamber radii.

The p_{cel} perturbation factors for a ±X magnetic field undergo a maximum, which is dependent on the chamber radius. The largest increase can be found for the R_1 chamber with +3.6% at 1.5 T for this field direction. For a magnetic field in ±Y-direction, p_{cel} decreases to a certain field strength (maximally by -1.5% at 3.0 T for the R_1 chamber), before increasing again towards higher field strengths. A magnetic field in ±Z-direction causes a monotonous decrease in p_{cel} for all chambers (by -1.4% at 3.0 T for the R_3 chamber at maximum). The smaller the chamber radius, the larger is the deviation of p_{cel} from unity for fields in ±Y- and ±Z-direction.
The p_{wall} perturbation factor rises for all chambers and magnetic field directions towards higher field strengths by 1 - 2% at 3.0 T, except for fields in +X-direction. This field direction causes a small decrease of -0.2% at 0.7 - 0.8 T for the R_3 to R_6 chambers, followed by an increase towards higher field strengths. In +X-direction the electrons enter the cavity from the chamber stem side, so they do not have to cross the wall material (less perturbation) as for the -X-direction. Therefore, p_{wall} increases less for +X magnetic fields compared with fields in -X-direction. The smaller the chamber radius, the smaller is the absolute value of p_{wall}.
The p_{repl} factor in ±X fields exhibits a minimum that depends on the chamber radius. The largest decrease of -8.0% is found at 0.6 T for the R_5 chamber. p_{repl} contributes most to the k_B^Q factor and thus presents a very similar shape. Magnetic fields in ±Y- and ±Z-direction cause only a small monotonous decrease with increasing field strengths in p_{repl} by about -0.2% to -0.3% at 3.0 T.

MR-compatible chambers

The magnetic field correction factors k_B^Q for the MR-compatible chambers and magnetic fields in ±X-, ±Y- and ±Z-direction are shown in figure 4.17. For a magnetic field in ±X-direction, a complex dependence on the magnetic field strength, orientation and chamber volume can be observed. For the $A19MR$ chamber, k_B^Q decreases until 1.0 T by up to -6.1% (-X) and -7.4% (+X). The maximum decrease is -5.8% and -2.9% for the $A28MR$ and $A1SLMR$ at 0.9 - 1.0 T for a field in +X-direction, while for a -X magnetic field k_B^Q increases for these chambers up to +3.3% and +1.2% at 0.7 T, respectively. For a magnetic field in in ±Y-direction, the magnetic field correction factor increases for all chambers, maximally by 1.0% for the $A19MR$ chamber at 3.0 T. k_B^Q decreases monotonously for a magnetic field in ±Z-direction by around -0.9% at 3.0 T.

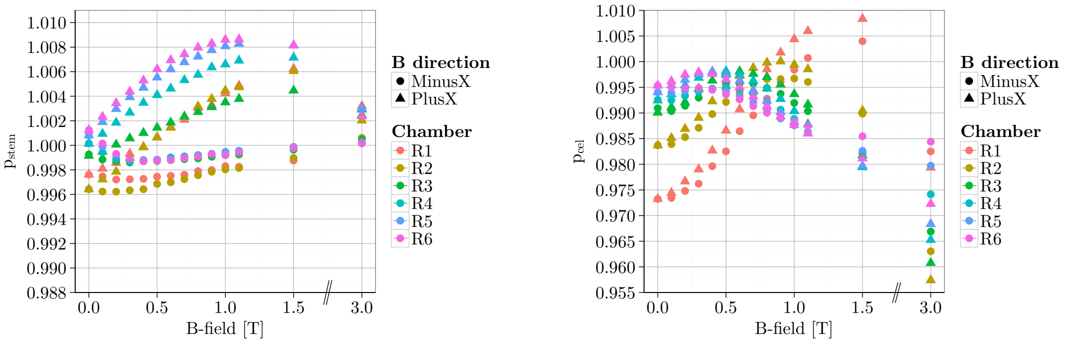

(a) X B-field.

(b) X B-field.

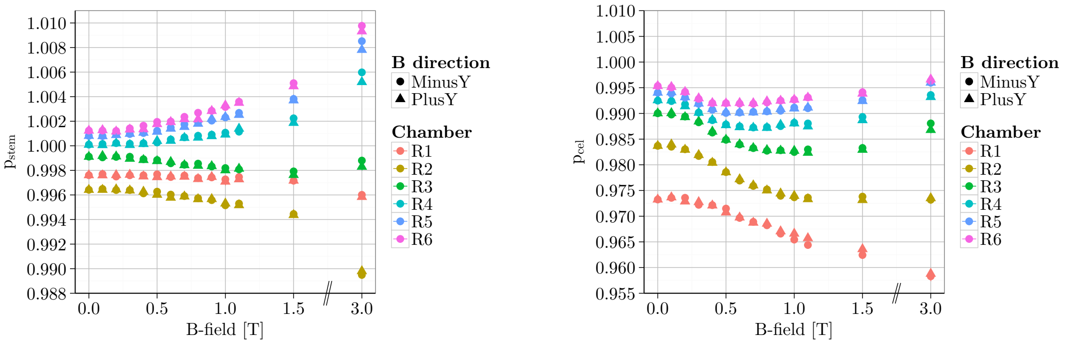

(c) Y B-field.

(d) Y B-field.

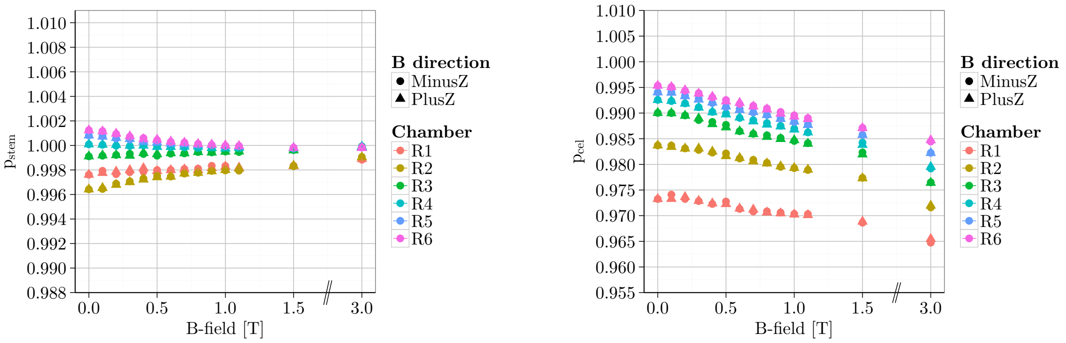

(e) Z B-field.

(f) Z B-field.

Figure 4.15: Perturbation factors of the chamber stem p_{stem} (a,c,e) and the central electrode p_{cel} (b,d,f) for the six Farmer-type chambers and magnetic fields in ±X- (a,b), ±Y- (c,d) and ±Z-direction (e,f). Most errorbars are smaller than the symbol sizes. Reprinted from Spindeldreier et al. (2017b).

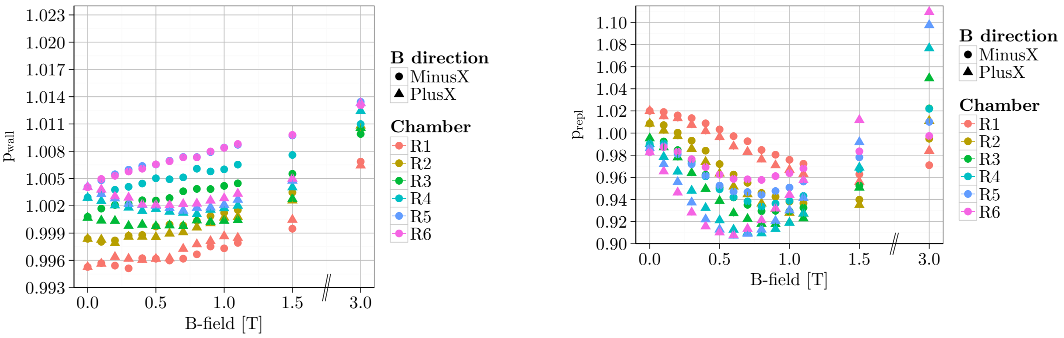

(a) X B-field. **(b)** X B-field.

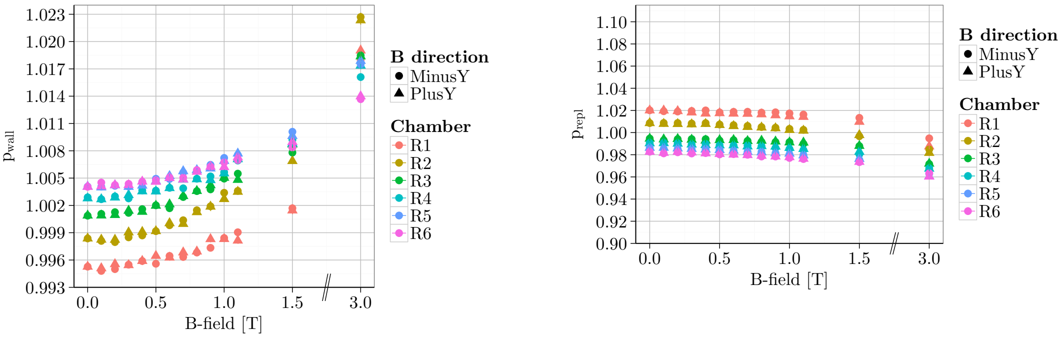

(c) Y B-field. **(d)** Y B-field.

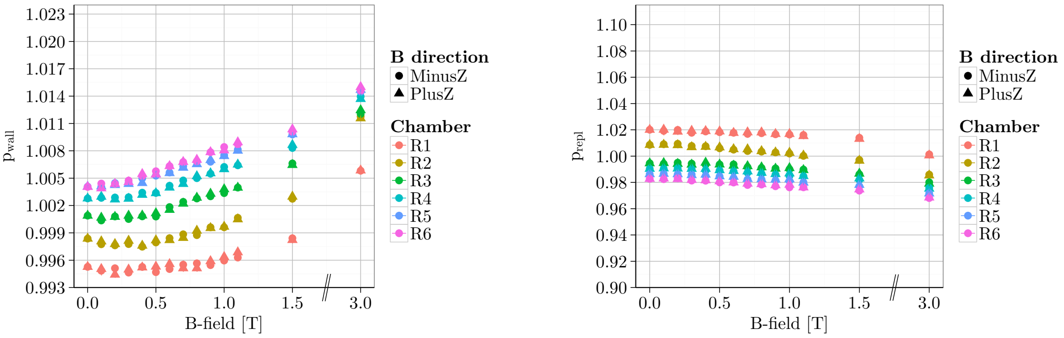

(e) Z B-field. **(f)** Z B-field.

Figure 4.16: Perturbation factor of the chamber wall p_{wall} (a,c,e) and the replacement perturbation factor p_{repl} (b,d,f) for the six Farmer-type chambers and magnetic fields in ±X- (a,b), ±Y- (c,d) and ±Z-direction (e,f). Most errorbars are smaller than the symbol sizes. Reprinted from Spindeldreier et al. (2017b).

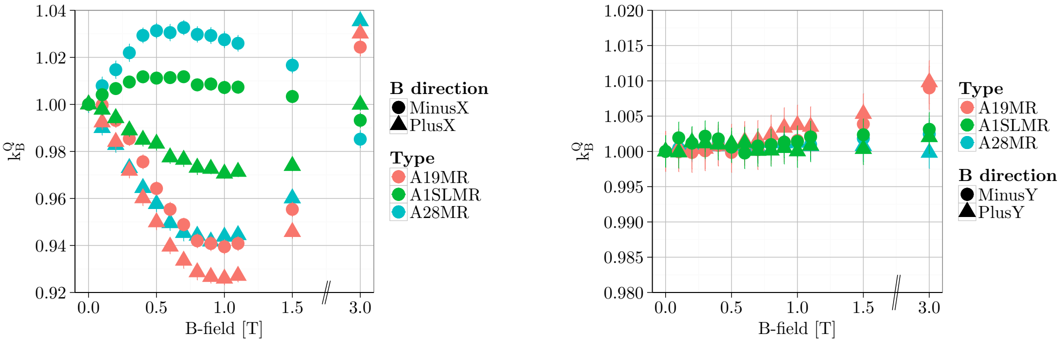

(a) X B-field. **(b)** Y B-field.

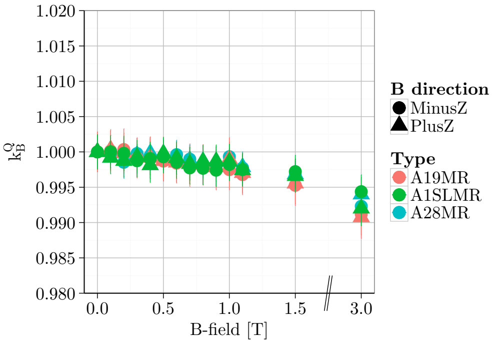

(c) Z B-field.

Figure 4.17: Calculated magnetic field correction factors k_B^Q of the MR-compatible chambers and magnetic fields in (a) ±X- (b) ±Y- and (c) ±Z direction.

Influence of the spectrum

The photon spectra used are depicted in figure 4.18a: The energy distribution of the "reference spectrum" from Mohan et al. (1985) is shown in black, while the spectra for comparison are drawn in color. The Elekta SL25 spectrum and the Siemens Primus spectrum yield more low energy photons (0 - 500 keV), while the Varian Clinac 600C spectrum has a very similar energy distribution as the reference spectrum.
Figure 4.18b shows the calculated k_B^Q correction factors as well as the differences of these factors to the one calculated with the reference spectrum for all magnetic field strengths in ±X-direction. A maximum deviation of around 0.5% can be observed for factors calculated with the Elekta SL25 and the Siemens Primus spectra, while root mean square differences lie in the range of 0.2%. The differences for the Varian Clinac 600C calculated factors are small (within 0.2%).

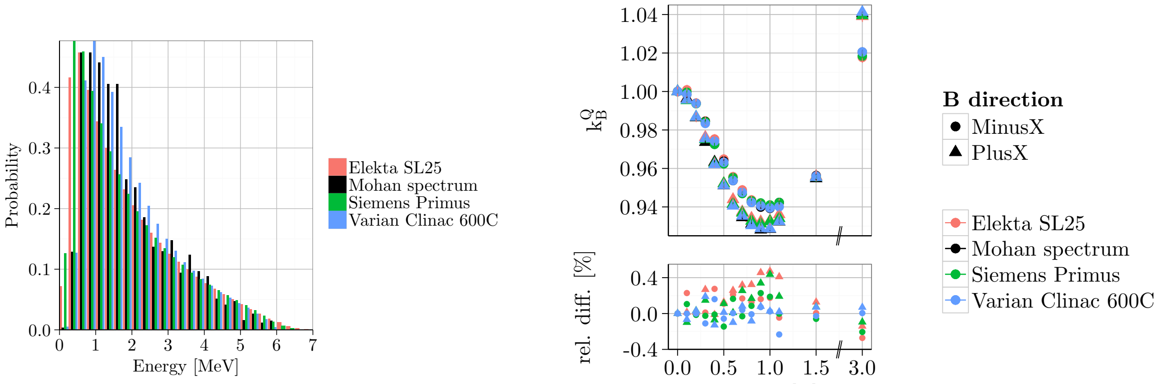

(a)

(b)

Figure 4.18: Influence of different 6 MV spectra on the k_B^Q factor of the R_3 chamber for magnetic fields in ±X-direction.

The k_B^Q factor calculated with the reference 6 MV spectrum in dependence of the depth position is shown in figure 4.19 for magnetic fields of 1.5 T in ±X, ±Y and ±Z-direction. Behind a depth of approximately 1.5 cm, the k_B^Q factor stays rather constant (within 0.4%) for each magnetic field direction.

Influence of the magnetic field gradients

The response of the R_3 chamber in ±X magnetic fields with a change of ±10 mT is depicted in figure 4.20. No substantial differences in the response curves can be observed. The root mean square difference between the changed curve and the reference curves is about 0.1% with a maximum difference of 0.3%.

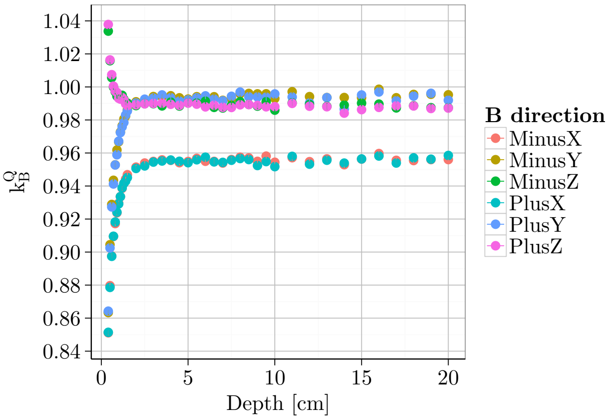

Figure 4.19: The magnetic field correction factor k_B^Q of the R_3 chamber in different depth for 1.5 T magnetic fields in ±X-, ±Y- and ±Z-direction.

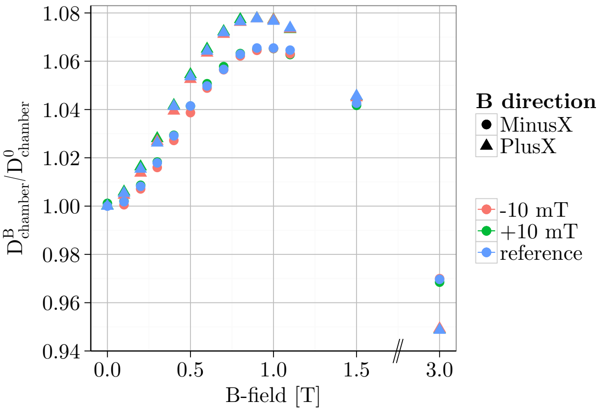

Figure 4.20: Response of the R_3 chamber for magnetic fields in ±X-direction, varied by ±10 mT.

4.3.4 Effective point of measurement

Figure 4.21 depicts the depth dose curves in a water voxel as well as calculated with the R_3 chamber with and without a magnetic field of 1.5 T in -X-, -Y- and -Z-direction. A small shift between the water and the chamber curves, which represents the EPOM shift Δz, can be observed.

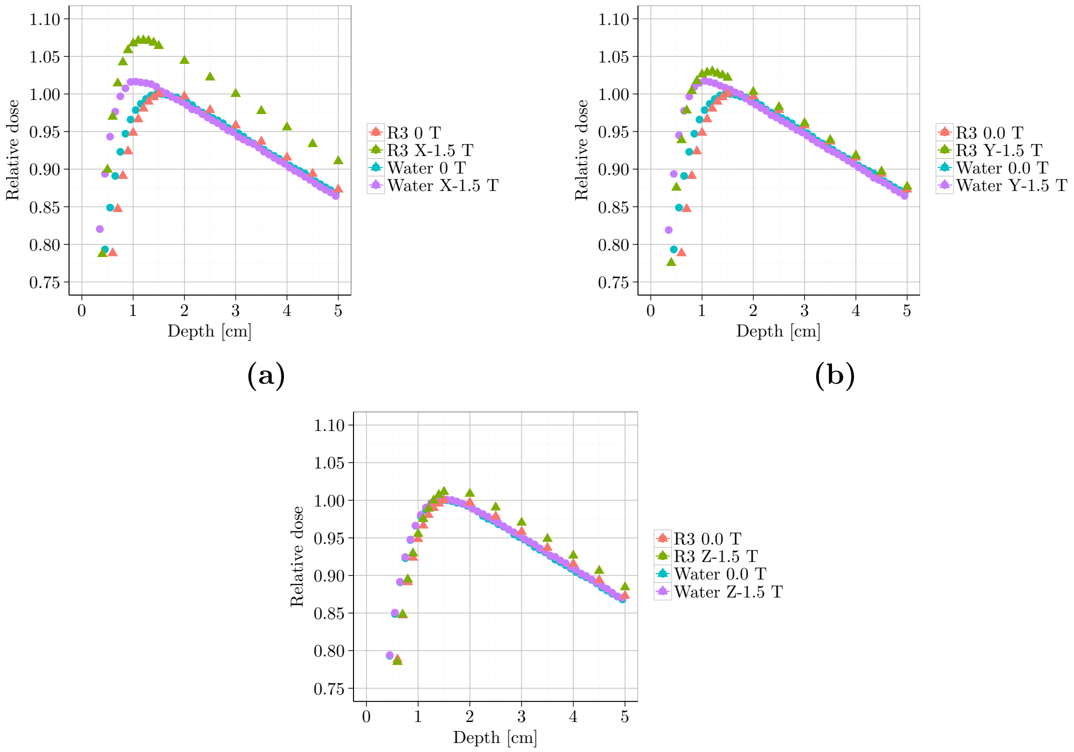

(a)

(b)

(c)

Figure 4.21: The PDD curves in a water voxel and in the R_3 chamber with and without a 1.5 T magnetic field in (a) -X-, (b), -Y- and (c) -Z-direction. The curves are normalized to the dose maximum in water and the chamber without magnetic field, respectively.

The χ^2 minimization is exemplarily shown for 0.0 T and a field of -1.5 T in Y-direction in figure 4.22a. The minimum χ^2 with magnetic field is clearly formed at smaller Δz shifts. The ratios of dose to water and dose to the chamber in dependence of the depth for the optimal Δz shift is displayed in figure 4.22b. They vary slightly around the constant k value, drawn as a dashed line.

The EPOM shifts Δz of all chambers and magnetic fields are depicted in figure 4.23. In general, the shift depends not only on the chamber radius, i.e. without magnetic field the R_1 chamber exhibits an EPOM shift of $0.1 \cdot r$, while the R_6 chamber has a Δz of $0.6 \cdot r$. With a magnetic field in ±X- and ±Y-direction, Δz decreases with increasing field strength, e.g. from $0.5 \cdot r$ to $0.3 \cdot r$ at 1.5 T for the R_3 chamber. In contrast, the shift increases for a ±Z magnetic field for all chambers, e.g. up to $0.6 \cdot r$ at 1.5 T for the R_3 chamber.

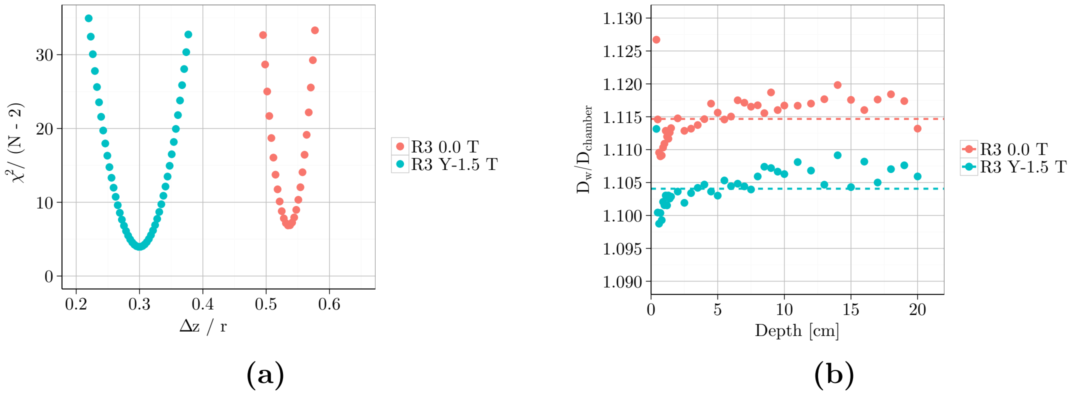

Figure 4.22: Determination of the optimal Δz for the R_3 chamber with and without a 1.5 T magnetic field in -Y-direction: (a) Minimization of χ^2 per degrees of freedom (N = number of calculated chamber positions) in dependence of Δz. (b) Ratio of dose to water and dose to the chamber (f) in different depths.

Figure 4.24 shows the profile of the radiation field in a water voxel and in the R_3 chamber with and without a -1.5 T magnetic field in Y-direction. Due to the magnetic field, the profile is slightly asymmetric towards the -X-direction. The lateral EPOM shift Δx is depicted in figure 4.25. For the smallest R_1 chamber no substantial shift is observable. The lateral shift increases with increasing magnetic field strengths for the R_2, R_3 and R_4 chambers. The largest Δx can be found for the R_6 chamber with around ±0.2 cm at ±1.0 T. For the R_5 and R_6 chamber, the shift Δx decreases again slightly for even higher magnetic fields at ±1.5 T. In general, for a magnetic field in +Y-direction, the Δx shift is in +X-direction and for a magnetic field along -Y the Δx shift is in -X-direction.

4.4 Measurements with OSLDs in magnetic fields

4.4.1 Response of OSLDs

The S/S_R to dose curve of the Risø reader is shown in figure 4.26. The curve through the data points was obtained by least-squares fitting of a saturated exponential function. This curve was used to convert the measured S/S_R values into dose values.
Figure 4.27 presents the results of the detector response measurement with detector packages, containing five detectors each, in dependence of the magnetic field. For the read-out with the portable reader, the standard deviation of the packages is 1 - 2%. The mean OSL signal for different field strengths stays within ±2.3% of the signal without magnetic field. For the read-out with the automated Risø reader, a standard deviation of around 1% is obtained for the detector packages. The mean S/S_R value stays within ±1.4% of the value without magnetic field. Calculating the correlation coefficient of dose per detector and magnetic field strength, reveals a value of -0.2 for the read-out with the portable reader and of -0.4 for the read-out with the Risø reader.

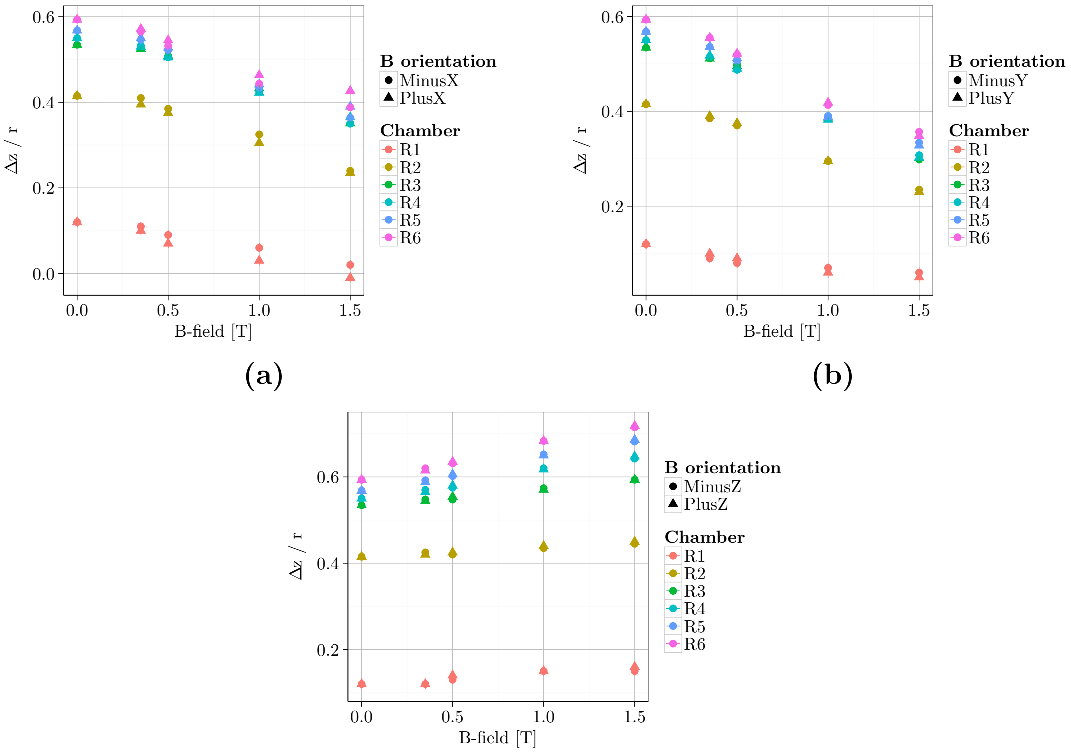

(a)

(b)

(c)

Figure 4.23: The shift of the longitudinal EPOM Δz of the Farmer-type chambers for a magnetic field in (a) ±X-, (b) ±Y- and (c) ±Z-direction.

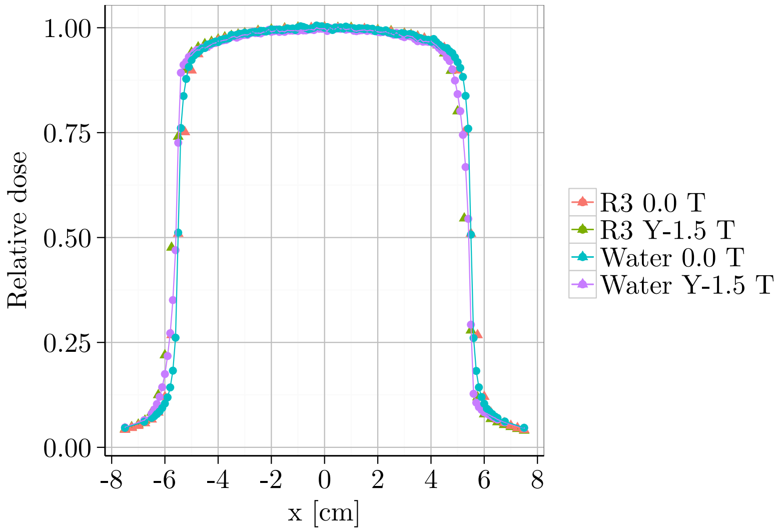

Figure 4.24: Profile in a water voxel and in the R_3 chamber with and without a 1.5 T magnetic field -Y-direction. The curves are normalized to the central dose value without magnetic field.

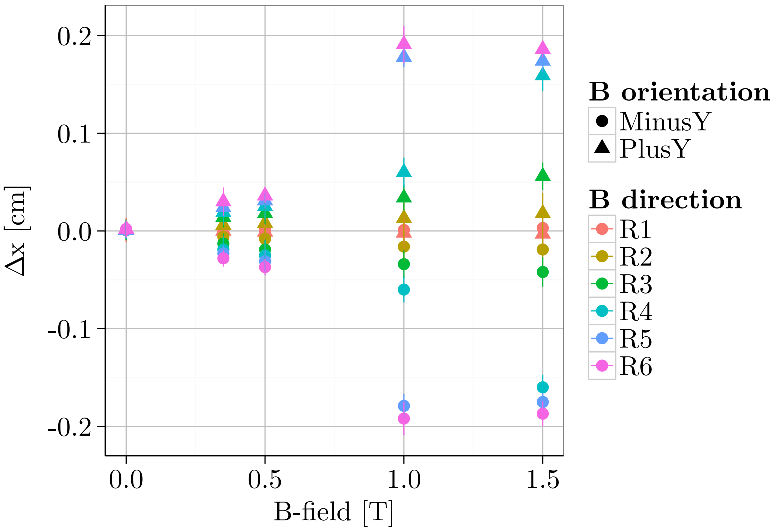

Figure 4.25: The lateral EPOM Δx shift of the Farmer-type chambers for a magnetic field in Y-direction.

Since the outer detectors of the detector packages were close the radiation field penumbra, a second measurement was performed using only one detector in the center of the radiation field and the automated Risø reader for read-out. For this measurement, the correlation coefficient of dose and magnetic field strength is found to be -0.3. Figure 4.28 depicts the comparison of measurement 1 (five detectors per package) and measurement 2 (one detector per package) as well as the simulation results. The standard uncertainty of the mean value per magnetic field strength is below 0.4% for measurement 1 and 2.

To investigate the dependence of magnetic field strength and deposited dose, a statistical test on linear regression was performed with the statistics software R (R Core Team, 2016). For measurement series 1, read-out with the portable reader, no significant result is obtained (p-value: 0.115). However, for the read-out with the automated reader, a significant linear regression between dose and magnetic field strength is found for measurement series 1 (p-value: $6.4 \cdot 10^{-5}$) and measurement series 2 (p-value: $5.9 \cdot 10^{-5}$). The linear regression test detected a decrease in response of -1.3% per Tesla with a 95% confidence interval between -1.8% and -0.9%. However, the dependence of the response on the magnetic field strength may be non-linear in reality. The results of the simulation are described in section 4.5.1.

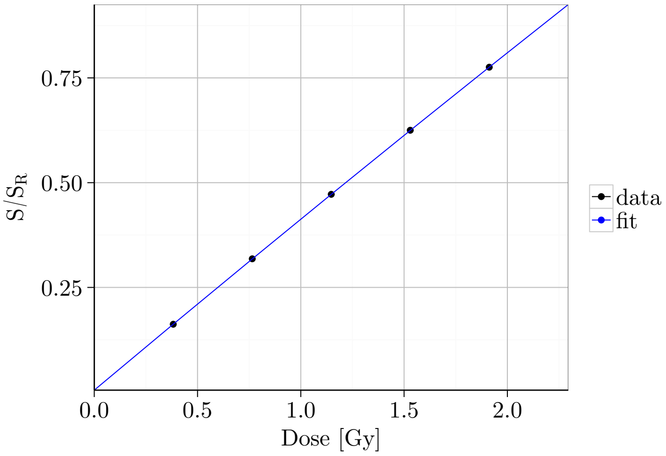

Figure 4.26: S/S_R to dose curve for the Risø reader acquired with the built-in β-source. Each data point was obtained by averaging over five detectors. The uncertainties are smaller than the symbol sizes. Reprinted from Spindeldreier et al. (2017a).

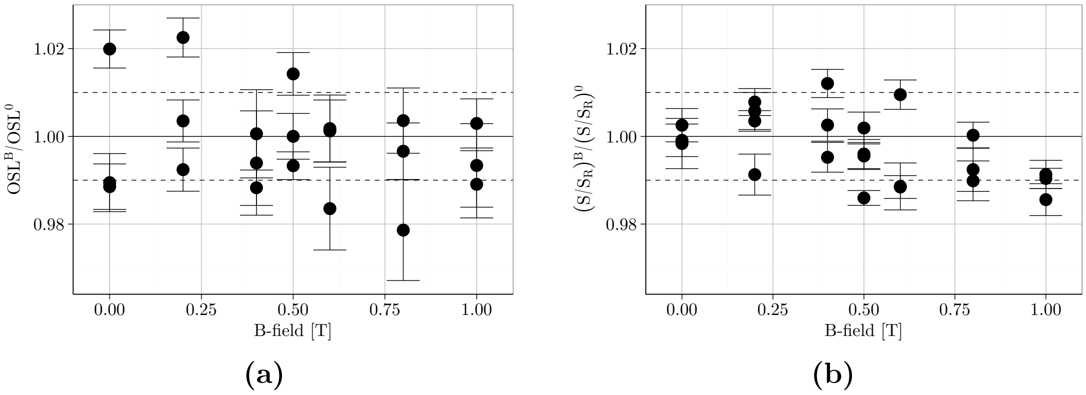

Figure 4.27: (a) Mean OSL signal and (b) mean S/S_R per detector package in dependence of the magnetic field normalized to the mean value at 0 T of all detectors. Read-out was performed with the portable reader (a) and with the automated Risø reader (b), respectively. The errorbars represent the standard deviation of the mean value of the detector packages. Reprinted from Spindeldreier et al. (2017a).

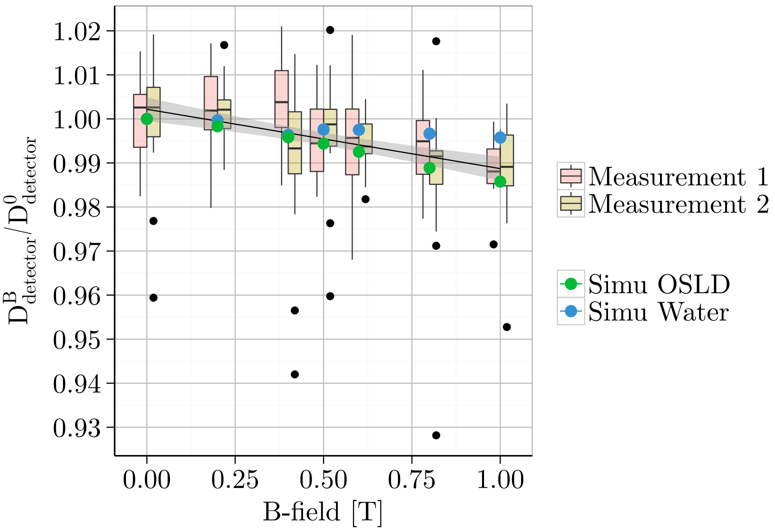

Figure 4.28: Boxplot of the results of measurement series 1 (five detectors per package) and series 2 (one detector per package), read-out with the automated reader. The lines in the boxes represent the median and the boxes display the first and third quartiles (25^{th} and 75^{th} percentiles). The whiskers extend until the lowest and largest values, but no further than $1.5 \cdot IQR$, with IQR being the inter-quartile range. Data points beyond the whiskers are depicted individually. Further, the linear regression curve with 95% confidence interval is plotted.
For comparison, the simulated dose in the detector as well as in a water voxel is shown.

4.4.2 Angular dependence of OSLDs

The results of the angular dependence measurement and simulation in magnetic fields are shown in figure 4.29. The dose decreases by around -3% to -4% for a parallel irradiation (90°). For a 180° irradiation, a dose increase of around 2% was observed. Moreover, a very good agreement between the results of the ^{60}Co (0.35 T) and the 6 MV angular dependence measurement was found.

Within the measurement uncertainty no change in the angular dependence due to the magnetic field can be detected. The simulation results are described in section 4.5.3.

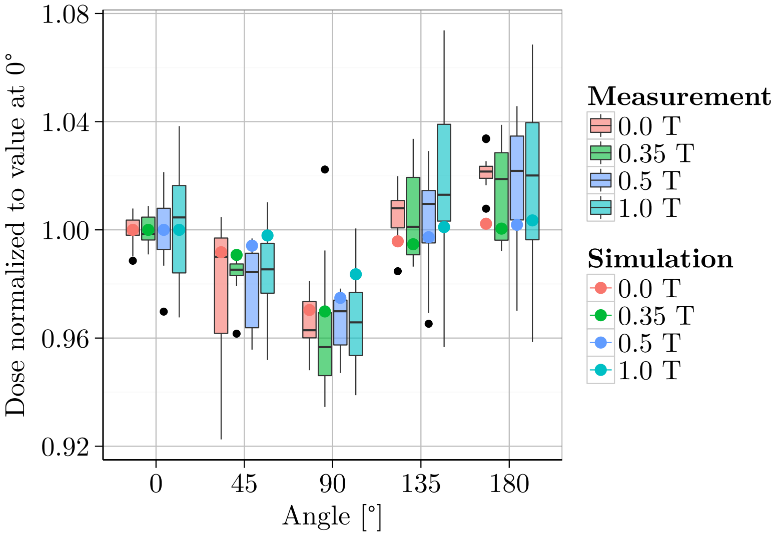

Figure 4.29: Angular response of the OSLDs in different magnetic fields: The measured signals relative to the value at 0° are displayed as boxplots. The median values are shown as lines in the boxes and the boxes represent the first and third quartiles (25th and 75th percentiles). The whiskers extend until the lowest and largest values, but no further than $1.5 \cdot IQR$, with IQR being the inter-quartile range. Data points beyond the whiskers are depicted individually.
The simulated results are displayed for comparison.

4.4.3 OSLDs in a heterogeneous phantom

In figure 4.30 the TPS dose and the OSL dose of the measurement in the heterogeneous phantom are compared. All measured OSL doses agree within 5% with the TPS doses. The standard uncertainty of the mean of the OSL measurements is between 0.2% to 1.3%.

For the large 21 x 21 cm^2 field (field c) all OSL doses are higher (+0.2% to +3.7%) than the TPS doses, whereas the OSL doses of the smaller 6.3 x 6.3 cm^2 field (field b) are by trend lower than the TPS doses (-3.3% to +0.5%). For the slit field of 2.1 x 27.3 cm^2 size (field a), the OSL doses in the upper part of the phantom are about -2% lower than the TPS doses, while the OSL doses in the center of the phantom are about +4% higher.

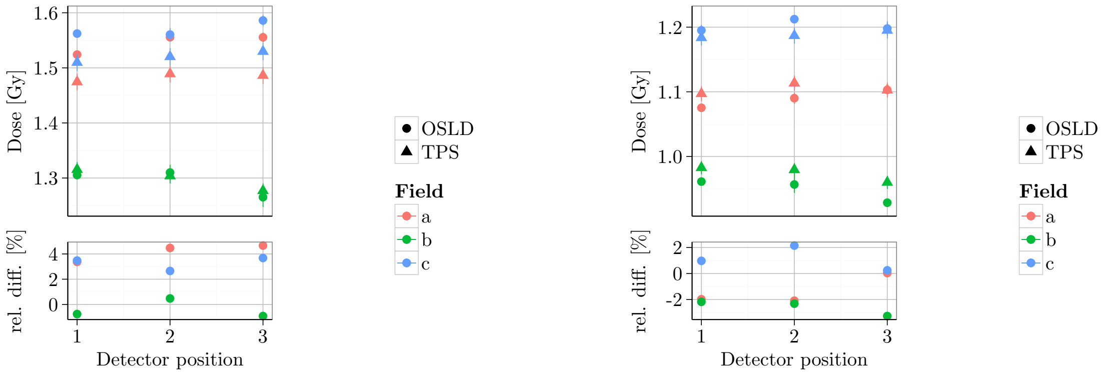

(a) (b)

Figure 4.30: Comparison of TPS dose and OSL dose in the heterogeneous phantom for the detectors (a) in the upper part and (b) in the center of the phantom. The uncertainty is smaller than the symbol dimensions.

4.5 Monte Carlo simulation of OSLDs in magnetic fields

4.5.1 Response of the OSLDs

The simulated response of the OSLD in magnetic fields up to 1.0 T is shown in figure 4.28. Furthermore, the dose to a water voxel in presence of a magnetic field is depicted. Statistical analyses of the detector simulation results by means of a linear regression obtained a dose decrease of -1.5% per Tesla (p-value: $1.3 \cdot 10^{-5}$, 95% confidence interval: -1.7% to -1.2%). This agrees well with the measurement results (see section 4.4.1). However, the linear regression of dose to water detected a decrease of -0.4% (p-value: 0.01), but with a 95% confidence interval of -0.7% to +0.1%. As already mentioned in section 4.4.1, the dependence on the magnetic field strength may not be strictly linear.

4.5.2 Magnetic field correction factors

The calculated k_B^Q factors are displayed in figure 4.31. For a magnetic field perpendicular to the beam (X-direction), k_B^Q increases monotonically up to +2.4% at 3.0 T. For a magnetic field parallel to the beam (Z-direction), k_B^Q agrees with unity within the simulation uncertainty. No substantial influence of the magnetic field orientation can be observed for both cases.

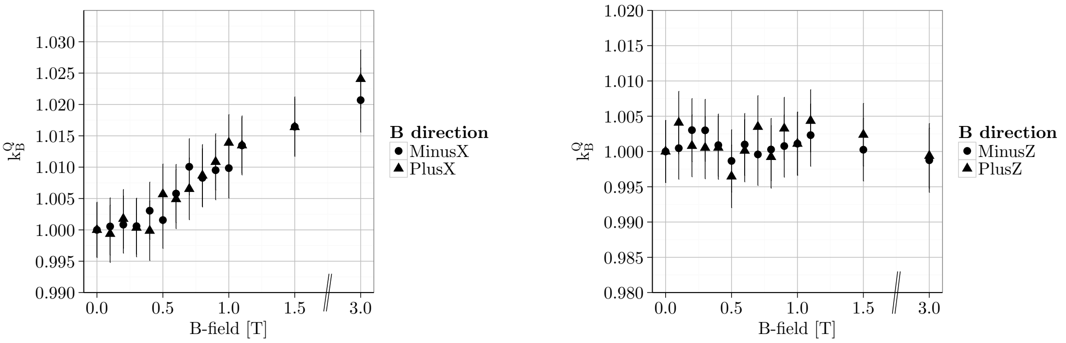

(a) **(b)**

Figure 4.31: Magnetic field k_B^Q correction factors for OSLDs in magnetic fields perpendicular (a) and parallel to the beam (b).

4.5.3 Angular dependence of OSLDs

In agreement with the measurement, the simulated angular dependence shows a decrease for a 90° irradiation (see figure 4.29). However, no increase at 180° was obtained, in contrast to the measured results. Moreover, in the simulation small differences in the angular dependence for the different magnetic field strengths were found. For a 90° irradiation, the dose decreases by 3.0% without magnetic field, while it decreases by only 1.6% with a 1.0 T magnetic field.

Chapter 5

Discussion

MR-guided radiation therapy has the potential to further improve radiation therapy outcome by employing ionization-free imaging with excellent soft-tissue contrast before and during treatment. This technique is expected to enable real-time adaptive therapy and a better dose conformation to the target while sparing normal tissue. For clinical implementation of hybrid MRgRT devices, precise dosimetry in presence of the magnetic field has to be performed.

The aim of this work was to investigate the behavior of two types of dosimeters, ionization chambers and OSLDs, in magnetic fields. Ionization chambers are routinely used for reference dosimetry. Within the low-density air medium of the chamber cavity, electrons can be strongly deflected by the Lorentz force, resulting in a potentially large change in chamber response. Because of the higher density of the sensitive medium of OSLDs, the mean free path length of secondary electrons is smaller and therefore smaller effects due to the magnetic field are expected.
In this work, the influence of the magnetic field strength and orientation as well as of the sensitive volume on the response of ionization chambers was studied. Magnetic field correction factors and the EPOM were calculated. Moreover, the dependence of the OSLD response on the magnetic field strength and angular detector orientation was examined. In the following sections, the results and their implications for precise dosimetry in the presence of a magnetic field are discussed.

5.1 Ionization chambers in magnetic fields

5.1.1 Response of ionization chambers

In the response measurements and simulations, a substantial change in the chamber response in magnetic fields was found that depends on the chamber itself, the magnetic field strengths and the field direction. Concerning the Farmer-type chambers, the responses of the R_3 and the $A19MR$ agreed well - also with data of the $NE2571$ chamber investigated by Meijsing et al. (2009). All chambers showed a maximum increase in response of $+8\%$ around 1.0 T for a magnetic field in +X-direction, although construction details and materials were different.

Smit et al. (2013) measured a signal increase of 4.9% in the 1.5 T MR-linac with the $NE2571$ chamber, compared with a signal increase of 4.3% in our simulation. The difference was presumably caused by the different beam qualities - the MR-linac uses a flattening filter free beam, while in this project a flattened 6 MV spectrum was used in the simulations.

Meijsing et al. (2009) explained the altered response with changes in the number of electrons reaching the sensitive cavity volume and the path length of the electrons within this volume. The analysis of the electrons in the chamber cavity of the six Farmer-type chambers confirms this explanation: The mean track length of electrons increases with increasing magnetic field strength in ±X-direction up to a chamber-dependent field strength (see figure 5.1a). The electrons are deflected on circular paths inside the air volume and thus travel larger distances than without magnetic field. The maximum increase in track length is smaller for the large R_6 chamber than e.g. for the smaller R_3 chamber. This may be explained by the surface to volume ratio, which decreases with increasing chamber radius. At a certain field strength, the electron radii get so small that the average path length decreases again. Only a minor influence of the magnetic field orientation on the mean electron track length can be observed.
In contrast, the relative number of electrons is highly dependent on the field orientation and thus is the reason for the field orientation dependence of the chamber response (see figure 5.1b). For a magnetic field in +X-direction, the number of electrons reaching the sensitive cavity volume exhibits a maximum. Electrons in the chamber stem or the dead air volume are deflected towards the sensitive volume (see figure 5.2b). Therefore, the number of electrons first rises for all chambers with an increasing magnetic field in +X-direction (see figure 5.1b). At a certain field strength, a maximum number of electrons entering the cavity is reached and the number decreases again due to the pronounced lateral deflection of electrons. For a field in -X-direction, the electrons are deflected from the chamber tip towards the chamber stem (see figure 5.2a) and the relative number of electrons reaching the sensitive volume decreases towards higher magnetic field strengths. The difference in the relative number of electrons between the two field orientations is larger for larger chamber radii.

In contrast to the Farmer-type chambers, the response of the MR-compatible $A1SLMR$ and $A28MR$ chamber decreases for a magnetic field in -X-direction until a certain field strength and increases again for even higher magnetic fields. This can be explained by their smaller cavity length. The mean track length rises only slightly with increasing magnetic field strength, thus the decreasing amount of electrons reaching the cavity for a field in -X-direction dominates the chamber response.

Moreover, no substantial influence of a 0.5 T magnetic field on the polarity and recombination correction of the Farmer-type chambers was observed. This agrees with the findings of Smit et al. (2013) for a $NE2571$ Farmer-type chamber in a 1.5 T field.

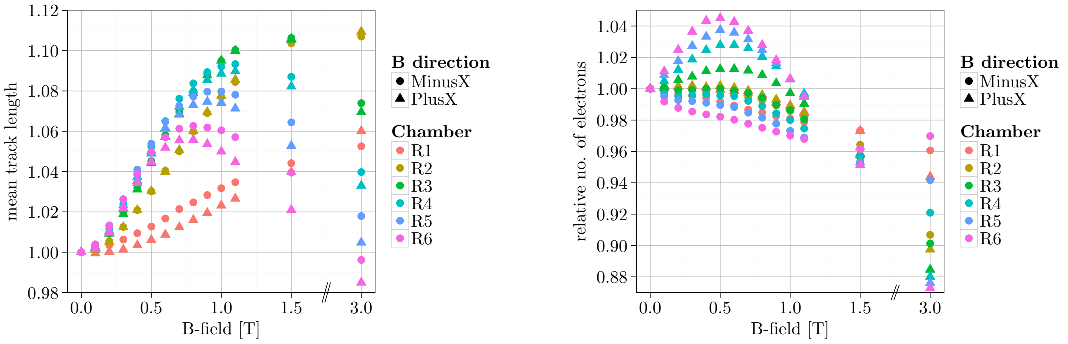

(a) **(b)**

Figure 5.1: (a) Mean track length and (b) number of electrons in the sensitive cavity volume of the Farmer-type chambers as a function of field strengths in ±X-direction normalized to 0 T. Reprinted from Spindeldreier et al. (2017b).

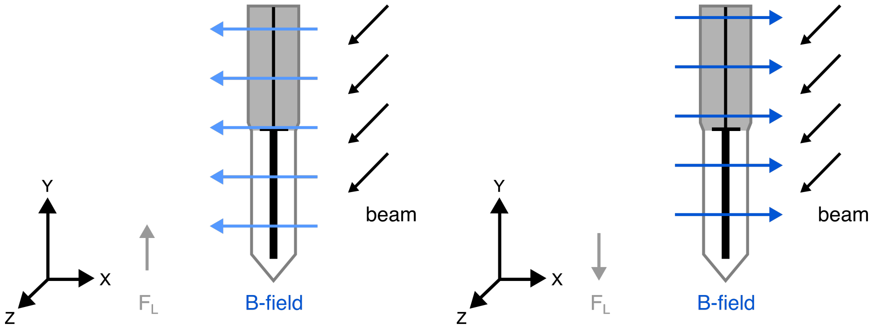

(a) **(b)**

Figure 5.2: Schematic drawing of the response measurement in magnetic fields: (a) The magnetic field is directed along the -X-axis, (b) along the +X-axis. F_L represents the direction of the Lorentz force for electrons traveling along the Z-axis (beam direction).

5.1.2 Influence of the sensitive volume

The exact response of the Farmer-type chambers in a magnetic field in +X- or -X-direction can only be reproduced in the simulation when a small dead volume at the guard electrode is added. Dead volumes can occur, since the electric field at the guard electrode may be slightly disturbed and charges produced in this volume are not collected by the central electrode but e.g. by the guard electrode. Butler et al. (2015) observed such a signal reduction, i.e. a dead volume, near the chamber stem of the PTW30013 chamber that corresponds to the R_3 chamber used in this study. The dead volumes need to be taken into account for simulations in magnetic fields, especially when the electrons are bent towards or away from the dead volume. If the average Lorentz force is directed along the chamber axis, hot and cold dose spots can be found at the guard electrode. Therefore, excluding these regions from the sensitive volume has a substantial effect on the chamber response in magnetic fields. This was confirmed by Malkov and Rogers (2017). They found that small changes in the simulated sensitive volume of several chambers (0.0 mm, 0.5 mm and 1.0 mm dead volume) can lead to large variations in the response in magnetic fields.

To account for the dead volume, these regions are excluded from the sensitive chamber volume in the simulations. In the presented simulations, the dead volumes are assumed to be cylindrical-shaped. Since the electric field lines in the air volume adjacent to the chamber stem are bent towards the guard electrode, realistic dead volumes may be rather toroidal-shaped.
The simulated dead volume may also be affected by inherent limitations of an efficient Monte Carlo transport, e.g. the cut-off energies. However, the scope of this investigation was not to model the dead volumes in detail, but to understand their influence on the chamber response.

In principle, the orientation between magnetic field and chamber may also influence the dead volume in the Monte Carlo simulation, since electrons below the cut-off energy are discarded locally. In a measurement, the magnetic field orientation affects the angular distribution of these low-energy electrons and hence the measured charge. However, the residual range of the low-energy electrons is of minor importance, if the average direction of the Lorentz force is perpendicular to the chamber axis. In this case, the electrons are not bent towards or away from the dead volume at the guard electrode and the dose distribution is rather homogeneous in this region.

The dead volume can be measured by scanning a chamber across a small slit beam or a step-like dose profile (Butler et al., 2015; Ketelhut and Kapsch, 2015). The recorded signal can be mapped to a two- or three-dimensional response map showing regions of reduced signal as dead volumes. Since dead volumes below 1 mm thickness (for the R_1 chamber) need to be detected, the experiment has to be very precise. In this work, the aim was to develop virtual chamber models that reproduce the measured response, rather than to determine the exact sensitive chamber volume. Therefore, the dead volume of the Farmer-type chambers was adjusted by excluding 0.1 mm slabs of air from the sensitive volume, until the measured and simulated responses agreed.

Comparing the response of a $PTW30013$ chamber in a ^{60}Co beam by Agnew et al. (2017) to simulations with a ^{60}Co spectrum (Rogers et al., 1988) yields a root mean square difference of 0.4%, with a maximum difference of 0.7% (see figure 5.3). This again confirms the validity of the developed simulation model of the R_3 chamber.

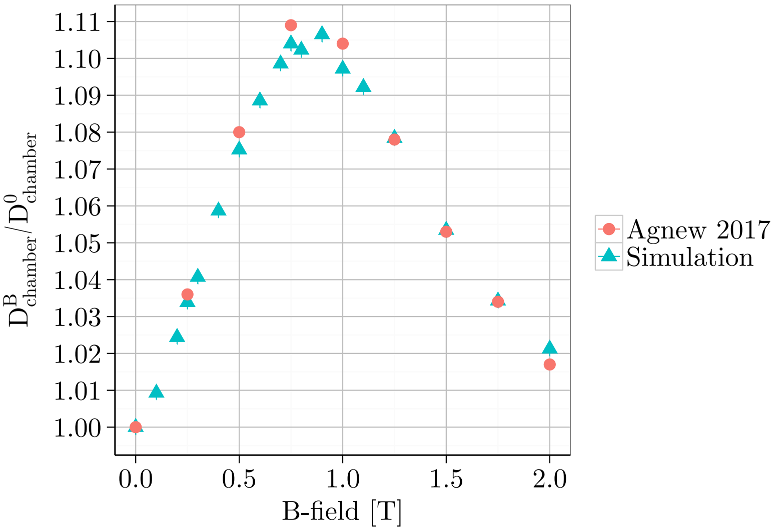

Figure 5.3: Comparison of measured (Agnew et al., 2017) and simulated chamber response of the R_3 chamber in ^{60}Co and magnetic fields up to 2.0 T.

In contrast to the Farmer-type chambers, the technical drawings of the MR-compatible chambers ($A19MR$, $A28MR$ and $A1SLMR$) comprised an outline of the dead volume. Therefore, the chambers could be directly simulated with the dead volume and no adjustment of the simulated dead volume needed to be performed. The good agreement between measurements and simulations confirmed the outlined dead volumes were appropriate for simulation.

5.1.3 Influence of the magnetic field orientation

For a magnetic field parallel to the chamber (±Y-direction) or parallel to the beam (±Z-direction), smaller changes in the response curves were observed compared to a field in ±X-direction. With the magnetic field applied in Y-direction, the average track length of electrons inside the cavity of the Farmer-type chambers slightly increases towards larger magnetic field strengths, while the number of electrons decreases (see figures 5.4). Therefore, the change in response reveals a small maximum curve for a field in ±Y-direction. Reversing the magnetic field yields no change in the response curve, since the average Lorentz force points along the ±X-direction, the rotationally-symmetric axis of the chambers (see figure 5.6). Manufacturing tolerances can lead to deviations from perfect rotational symmetry and chamber positioning accuracy is limited; therefore a small influence of the field orientation in Y-direction may exist in measurements.

In contrast to the Farmer-type chamber, the response of the MR-compatible chambers decreases with increasing magnetic field in Y-direction. This can be explained with the different material of the chamber wall and overall geometry of the chambers. For increasing field strength in Y-direction, the decreasing amount of electrons entering the cavity dominates the response for these chambers.

For a magnetic field parallel to the beam (±Z-direction), the average track length inside the chamber cavity and the amount of electrons reaching the cavity increase with increasing magnetic field strength for all Farmer-type chambers (see figure 5.5). This leads to the monotonous increase in chamber response for the magnetic field strengths studied. This increasing trend agrees with findings of Reynolds et al. (2013). For two Farmer-type chambers they found an increase of around 2% for a 1.5 T magnetic field parallel to the beam. Since a field in ±Z-direction causes a focusing of the electrons along the beam, no influence of the field orientation in Z-direction is expected. The same behavior can be observed for the MR-compatible chambers. The larger the chamber volume, the larger is the increase in chamber response.

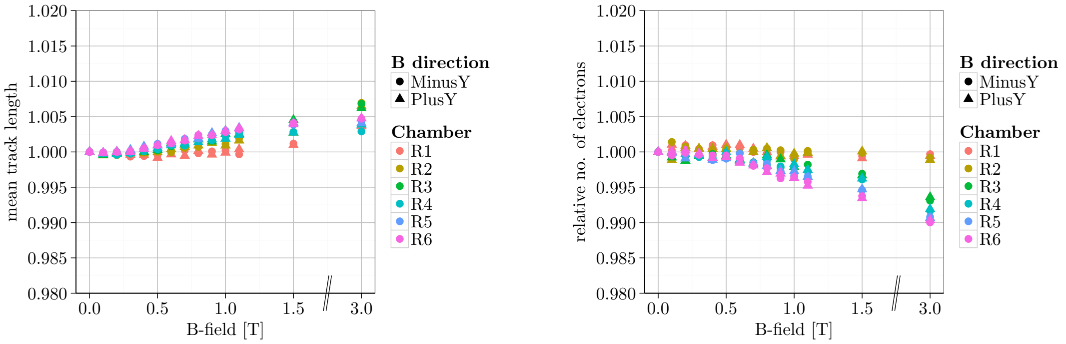

(a)

(b)

Figure 5.4: (a) Mean track length and (b) number of electrons in the sensitive volume of the Farmer-type chambers normalized to the values at 0 T as a function of the magnetic field strength in ±Y-direction.

Since the change in chamber response and thus the correction factors are smaller for a magnetic field in ±Y- or ±Z-direction, these geometries are concluded to be favourable for reference dosimetry. This agrees with the results of O'Brien et al. (2016), showing that the magnetic field correction factors are minimized for a field in ±Y-direction in an MR-linac. Moreover, the simulations are less dependent on the exact sensitive volume. As discussed in section 5.1.2, the dose distribution within the dead volume is rather homogeneous for a magnetic field in ±Y- or ±Z-direction. Therefore, excluding the dead volume from the sensitive volume in the simulations has only a minor effect on the chamber response curves (see figure 5.7).

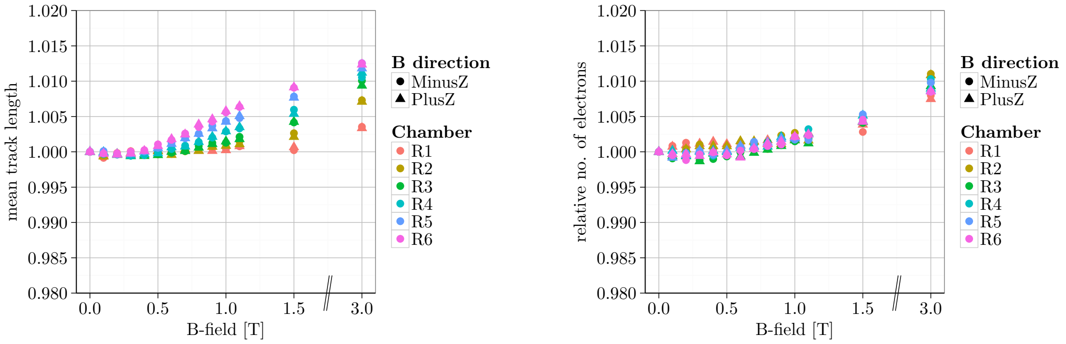

(a) **(b)**

Figure 5.5: (a) Mean track length and (b) number of electrons in the sensitive volume of the Farmer-type chambers normalized to the values at 0 T as a function of the magnetic field strength in ±Z-direction.

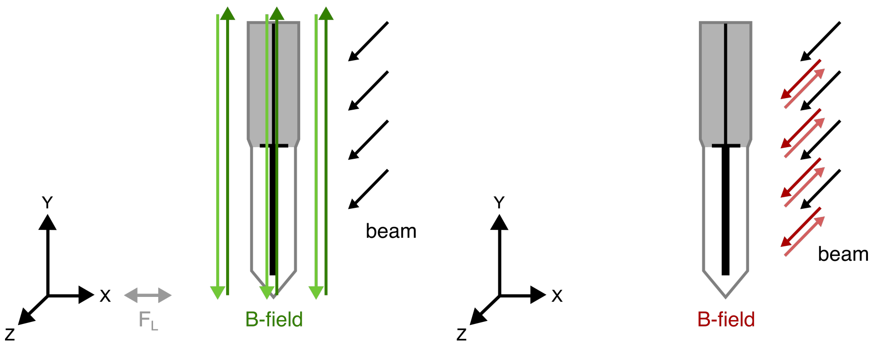

(a) **(b)**

Figure 5.6: Schematic drawing of the response simulations in magnetic fields. (a) The magnetic field directed along the ±Y-axis, (b) the magnetic field directed along the ±Z-axis. F_L represents the direction of the Lorentz force for electrons travelling along the Z-axis (beam direction).

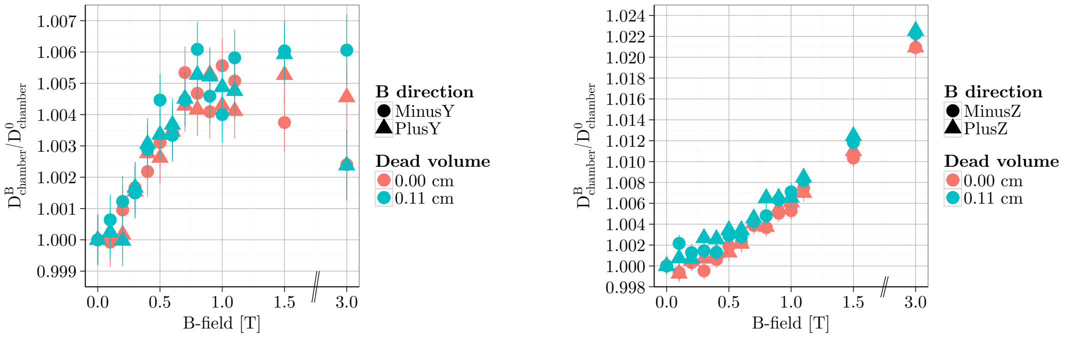

(a) **(b)**

Figure 5.7: Simulated response of the R_3 chambers with and without dead volume in magnetic fields in (a) ±Y- and (b) ±Z-direction.

For a recommendation of a reference dosimetry set-up, the influence of a small misalignment of the chamber needs to be taken into account. Smit et al. (2013) measured the angular dependence in a 1.5 T MR-linac. They found that a 10° misalignment causes a change in response of less than 0.6% for a magnetic field in ±Y-direction and less than 0.4% for a field in ±X-direction, suggesting a similar impact of set-up misalignment for both geometries. This was confirmed by simulations by Reynolds et al. (2017), showing that for a 3° misalignment the angular response of the Farmer-type $PR06C$ chamber changes on average by less than 0.4% for a magnetic field in both ±X- and ±Y-direction, while the maximum variations are slightly larger for the ±Y magnetic field.

5.1.4 Magnetic field correction and perturbation factors

The magnetic field correction factors k_B^Q can be calculated by means of Monte Carlo simulations. The factor calculated for the R_3 chamber in a 1.5 T field in Y-direction (0.993 ± 0.3%) agrees well with published data from Pojtinger et al. (2017) (0.994 ± 0.3%) and O'Brien et al. (2016) (0.994 ± 0.2%). Also, for a field in ±X-direction, the calculated values of this study and data from O'Brien et al. (2016) coincide within the simulation uncertainty of 0.3%, although the beam qualities slightly differ. De Prez et al. (2016b) measured the k_B^Q factor of the $PTW30013$ chamber for a 1.5 T field in X-direction by means of an MR-compatible water calorimeter in an MR-linac with a standard uncertainty of 0.8%. Again, although comparing a flattening filter free beam with a flattened beam, the measured value agrees well within 0.5% with our simulations. The k_B^Q factors of the $A19$ chamber in the 1.5 T MR-linac were calculated by O'Brien et al. (2016) with Monte Carlo simulations. They determined correction factors of 0.962 ± 0.25% for a -X magnetic field and 0.956 ± 0.25% for a +X field, that agree within 1.0% with the values obtained in this study. This difference is consistent with the difference in beam quality as well as small differences in the chamber material, since in our study, the $A19MR$ was used instead of the $A19$ chamber. For a field in Y-direction, the values calculated in this work and by O'Brien et al. (2016) both yield 1.005 ± 0.28%.

As described in section 5.1.3, the k_B^Q correction factors can be minimized by using a magnetic field in ±Y- or ±Z-direction. Since the dose to water changes only slightly with increasing magnetic field, the correction factors are mainly determined by inverting the response curves. Experimentally, the k_B^Q factors can be determined with a newly developed transportable and magnetic field compatible water calorimeter (De Prez et al., 2016a). The measured values should be used to validate Monte Carlo calculated correction factors of routinely used reference chambers. Since the precise k_B^Q determination by means of water calorimetry is time- and labor-extensive, the magnetic field correction factors will not likely be routinely determined experimentally in the various user beams in near future. Consequently, Monte Carlo calculated factors will be needed for all chambers, magnetic field strengths, set-up geometries and beam qualities used.

The perturbation factors of the Farmer-type chambers reveal the largest variations for magnetic fields in ±X-direction. In this case, p_{stem} and p_{wall} change around 1% and p_{cel} around 4%. The replacement perturbation factors p_{repl} shows the largest deviations with changes of up to -8.0% and thus has the biggest impact on the k_B^Q factor. If the magnetic field is aligned in ±Y-direction, p_{stem} varies around 1%, p_{cel}, p_{wall} and p_{repl} around 2%. For a magnetic field in ±Z-direction, the smallest changes in perturbation factors are observed: p_{stem} varies only around 0.2% and p_{cel}, p_{wall} and p_{repl} around 1%.

For most of the investigated geometries, the differences to unity of p_{cel} and p_{wall} are bigger for chambers with small radii. Relative to the chamber radius, the electrode and chamber wall are larger for the R_1 chamber. Therefore, these components have the biggest influence on this chamber.
In the current IAEA protocol, the p_{stem} perturbation factor is neglected for the k_Q calculation (Andreo et al., 2006). Without magnetic field, p_{stem} differs only by below 0.4% from unity and thus has only a minor influence on k_Q. However, with a magnetic field of 1.5 T in X- or 3.0 T in Y-direction, p_{stem} can deviate by up to 1% from unity, depending on the chamber and the orientation of the magnetic field, and thus should be considered in the k_B^Q calculation. If the magnetic field points in Z-direction, p_{stem} remains very close to unity and can still be neglected.
The p_{cel} perturbation factor decreases with increasing magnetic field in Y- and Z-direction. At higher field strengths more electrons can reach the central electrode, resulting in a larger perturbation. The p_{wall} factor increases for higher field strengths, because more electrons can enter the cavity, when no wall is present. For the R_1 and R_2 chambers, p_{wall} is below unity, since the upper part of the wall was modified to match the chamber stem, which was adapted from the R_3 chamber.

Influence of the spectrum and magnetic field gradients

The 6 MV spectra of different linac machines differ only slightly in the amount of low-energy photons. For spectra with more low-energy photons, the calculated k_B^Q factors of the R_3 chamber are mostly slightly closer to unity compared with the other 6 MV spectra. Still, the differences in k_B^Q are small, in the range of 0.4%. This is confirmed by Monte Carlo simulations by Pojtinger et al. (2017), which show that k_B^Q factors in a 1.5 T field and a flattened and unflattened 6 MV beam agree within the simulation uncertainty of 0.2%. Hence, the magnetic field corrections factors can be calculated with reference spectra of the hybrid MRgRT devices and do not need to be determined for each individual machine separately.
The k_B^Q factor is almost depth-independent on the central beam axis. Therefore, no additional factor needs to be considered for depth dose curves or TPR measurements.

The question whether imaging-induced changes in the magnetic field can affect the response could be answered in section 4.3.3. Additional magnetic fields in the order of ±10 mT have no substantial influence on the chamber response. Measurements during imaging can be performed without additional correction factors.

5.1.5 Effective point of measurement

The Monte Carlo calculated shift of the EPOM Δz for the Farmer-type chambers agrees with measured values by Legrand et al. (2012a) without magnetic field within 0.1 mm. This close agreement confirms the calculation method and provides confidence for the EPOM determination in magnetic fields. Without magnetic field, Δz is between 0.5 - $0.6 \cdot r$ for the R_3 to R_6 chambers. The small R_1 and R_2 chamber exhibit smaller shifts. Thus, a shift of $0.6 \cdot r$ as recommended by the TRS protocol (Andreo et al., 2006) or $0.5 \cdot r$ as recommended by the DIN protocol (DIN, 2008), that only depends on the chamber radius, might be insufficient, as already discussed by Kawrakow (2006) and Tessier and Kawrakow (2009). The EPOM is also affected by the cavity length, the central electrode and the chamber wall. Since the investigated Farmer-type chambers exhibit the same dimensions in length, electrode and wall, the EPOM shift for these chambers would consist of a constant factor and a radius dependent factor, as presented by Legrand et al. (2012a).

Applying a magnetic field in ±X- or ±Y-direction causes a decrease in Δz due to the perturbation of the electron fluence. This agrees with Monte Carlo simulations by O'Brien and Sawakuchi (2016). Without magnetic field, the majority of electrons are forward directed along the beam and hit the chamber cavity on the upstream surface of the chamber. With magnetic field in ±X or ±Y-direction, the electrons are bent laterally due to the Lorentz force and might enter the chamber under an angle from the lateral surface (Looe et al., 2017). Therefore, the EPOM is shifted closer to the central electrode.
In contrast, Δz is increased for magnetic fields in ±Z-direction. In this case, the electrons are focused along the beam direction, leading to a more forward-peaked electron fluence than without magnetic field. For all field directions, no substantial influence of the magnetic field orientation was observed.

The magnetic field has also an effect on the lateral radiation field profiles. Since the Lorentz force deflects the electrons in a direction perpendicular to the electron motion and the magnetic field direction, the x-profile is perturbed and becomes asymmetric for a magnetic field in Y-direction. Due to the difference in perturbation in water and air, a lateral shift of the EPOM arises for thimble chambers in magnetic fields (O'Brien and Sawakuchi, 2016). This Δx shift increases for larger chamber radii and magnetic field strengths. For small chambers, like the R_1 chamber, no substantial lateral shift could be observed. Therefore, chambers with small radii would be easier-to-handle for profile measurements in magnetic fields.

In general, when recording base data like depth-dose curves and output factors in a hybrid MR-linac machine, the correct longitudinal and lateral EPOM shift needs to be used. These shifts might not only depend on the chamber, the magnetic field strength and field direction, but also on the radiation quality and field size. Since the lateral field profiles get very asymmetric for small fields and high magnetic field strengths, the maximum peak position of the profile may not lie on the central beam axis. This has to be considered for output factor measurements.

5.2 Optically stimulated luminescence detectors in magnetic fields

5.2.1 Response of OSLDs

The read-out with the automated Risø reader revealed a higher precision compared to the read-out with the portable OSL reader. The reason for the higher precision is due to the use of the S/S_R value instead of the bare OSL signal S. The normalization with a reference signal accounts for variations in the single detectors (detector mass, shape, sensitivity). Therefore, all measurements following this finding were read-out with the automated reader.

Two measurements have been performed with a different amount of detectors per irradiation, in order to minimize the influence of the radiation field size. The 3 x 10 cm^2 radiation field and profiles in x- and y-direction acquired with an OSL film are depicted in figure 5.8. In the first measurement, the outer detectors were close to the penumbra along the x-direction. In this direction, the OSL signal decreases by about -5% at a distance of ±1 cm from the field center. Therefore, the second measurement with only one detector in the center of the radiation field was performed. Both measurement series agree, however, no substantial decrease in the measurement uncertainty could be obtained in the second measurement. Moreover, the magnetic field does not affect the penumbra in x-direction, but in y-direction. Due to the large field size in y-direction, no influence of the field penumbra on the OSL signal is expected. The main source of measurement uncertainty might be small inaccuracies in the set-up, induced when changing the detectors.

In general, a small decrease in OSL signal with the magnetic field strength of approximately 1.3% per 1.0 T was observed when applying a linear regression. Due to the complexity of electron deflection patterns, however, deviation from a linear trend with increasing magnetic field are likely but the data did not permit another statistical conclusion. The decrease in detector signal due to the field was larger than the decrease in dose to water. The reason for this underresponse might be the decreased stopping power ratio of aluminum oxide to water for low energy electrons (Kerns et al., 2011). Since the electrons are deflected by the Lorentz force in presence of a magnetic field, more low energy electrons (large angle Compton electrons) reach the detector than without magnetic field.

Compared to ionization chambers, where signal changes of up to 9% at similar field strengths were observed as described in section 4.2.2, the influence of the magnetic field on the OSL signal is small. This can be explained by the difference in sensitive material. While ionization chambers use air as sensitive medium with a very low density ($\rho = 1.20 \cdot 10^{-3}$ g/cm^3), Al_2O_3:C OSLDs exhibit a higher mass density ($\rho = 3.95$ g/cm^3) than water. Therefore, the material has the opposite influence on the electron perturbation and on the resulting signal reading in a magnetic field than the air in ionization chambers.

Since the difference in density between Al_2O_3:C and water is smaller than between air and water, the change in signal reading in a magnetic field is lower in OSLDs than in air-filled ionization chambers. This supports the applicability of OSLDs in hybrid MR-linacs.

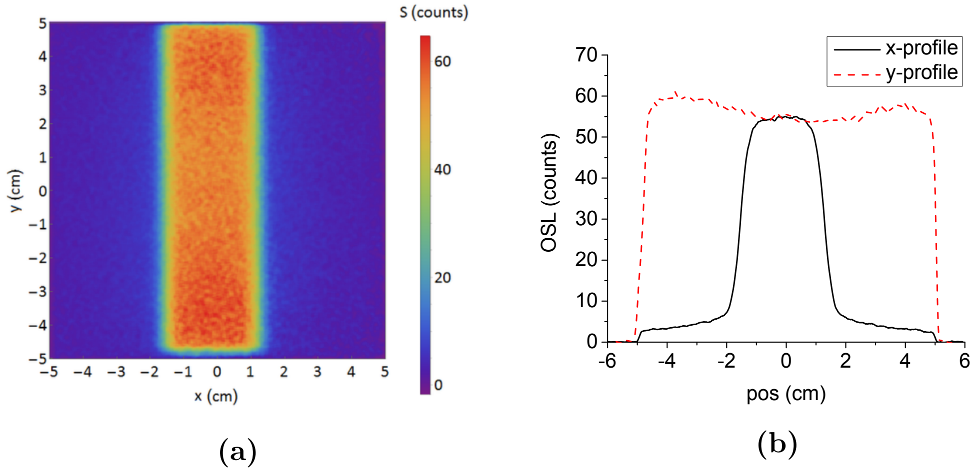

(a) (b)

Figure 5.8: (a) 2D distribution and (b) x- and y-profile of the 3 x 10 cm^2 radiation field acquired with an Al_2O_3:C,Mg OSL film at 10 cm depth of an RW3 slab phantom (PTW, Germany) without magnetic field. The read-out was performed with a dedicated laser-scanning reader (Ahmed et al., 2016). Reprinted from Spindeldreier et al. (2017a).

5.2.2 Magnetic field correction factors

The OSL detectors show a small change in detector response with magnetic field for a magnetic field perpendicular to the beam and no change for a magnetic field parallel to the beam. The calculated k_B^Q factors can be used to correct the measured OSL signals in a hybrid MR-linac device, if the calibration of the OSLDs is performed in a conventional linac without magnetic field. If the detectors can be calibrated directly in the MR-linac in presence of the magnetic field, no additional correction factor needs to be used.

5.2.3 Angular dependence of OSLDs

The measurement results suggest that the angular dependence of the OSL detectors does not depend on the magnetic field strength. Therefore, within the measurement uncertainty, an angular correction factor independent of the magnetic field strength can be used. The uncertainty in angle position can be estimated with approximately $\pm 5°$. Consequently, the measurement uncertainty can be reduced by improving the angle accuracy.

However, in the simulations a small dependence on the magnetic field strength was observed. The decrease in OSL signal for a parallel irradiation is caused by the decrease in stopping power ratio of aluminum oxide to water for low energy electrons, large angle Compton electrons that hit the detector from the side.

This agrees with nanoDot$^{\mathrm{TM}}$ OSL measurements and Monte Carlo simulations performed by Kerns et al. (2011). The change in stopping power ratio might also explain the small differences of the simulated angular dependence for different magnetic field strength. The Lorentz force deflects the electrons such that a different amount of low energy electrons can enter the detector. Furthermore, in the simulation the grain structure of the OSL detectors was not considered, which might have an influence in the measurement.

The angular dependence measured in a 6 MV and a ^{60}Co beam agree very well, i.e. no substantial influence of the beam quality was found. Moreover, in all measurements, the OSL signal was increased by about 2% for a 180° irradiation. This signal increase could not be reproduced in the simulations and does not agree with the measurements of Kerns et al. (2011). A possible explanation of this apparent difference might be the paper sheet in the detector packages. Testing this hypothesis and measuring the OSL signal at 0° and 180° without the paper sheet in the packages, no substantial difference in signal was found within the measurement uncertainty.

In order to avoid the use of additional correction factors, the OSLDs should be irradiated with a fixed perpendicular beam whenever possible.
The OSL signal at 0° measured in the 6 MV beam decreased on average by -0.4% and -1.4% at 0.5 T and 1.0 T, respectively. This agrees with the tendency found in figure 4.28.

5.2.4 OSLDs in a heterogeneous phantom

A good agreement of OSL dose and TPS dose in the heterogeneous phantom was found. In the upper part of the phantom, the OSL doses tends to be higher than the TPS dose. In this region, the phantom consists of cork. The TPS calculates dose to water, whereby the relative electron density is obtained from the CT image or is manually defined by the user. The low density of cork might influence the comparison of measured and calculated doses. A systematic study would be needed to investigate if the field size or the density of the phantom have an impact on the comparison of measurement and TPS, which was not the scope of this experiment. The aim of the measurement was to show the general applicability of the OSL technique in phantom measurements in a hybrid MR-radiotherapy device.

Chapter 6

Conclusions and outlook

In this work, the applicability of ionization chambers and OSLDs for dosimetry in high magnetic fields of hybrid MRgRT devices was investigated. The detector response in magnetic fields for different orientations was examined and magnetic field correction factors were calculated.

For air-filled ionization chambers, the response depends in a complex way on the sensitive volume of the chamber, the magnetic field strengths and the orientation between chamber, magnetic field and radiation beam. The largest change in response was found for the magnetic field perpendicular to the beam and the chamber axis. For this orientation, the exact definition of the sensitive volume excluding dead volumes is needed to correctly reproduce the measured chamber response and calculate corrections factors by Monte Carlo simulations. Since the Lorentz force deflects electrons into or away from the dead volume adjacent to the guard electrode, exclusion of the dead air volume from the sensitive volume has a large effect on the chamber response in magnetic fields. When the magnetic field is oriented parallel to the chamber axis or parallel to the beam, the variations in chamber response and thus in magnetic field correction factors are minimized. For these orientations, small dead volumes have a minor influence on the response. The response changes can be explained by the number of electrons reaching the cavity and their average path length inside the cavity.

Small changes in the beam spectrum have only a small influence on the chamber response. Therefore, the magnetic field correction factors can be calculated with reference spectra of the hybrid MRgRT devices and do not need to be calculated for each individual machine. Likewise, small magnetic field changes due to gradient fields for spatial encoding in MRI have only a minor impact on the chamber response, such that dosimetry will be feasible during imaging.

The EPOM of ionization chambers is affected by the magnetic field. A magnetic field perpendicular to the beam and the chamber or parallel to the chamber causes a decrease in the longitudinal shift, while the EPOM increases for a magnetic field parallel to the beam. A small lateral shift in the EPOM along the average Lorentz force direction was observed, depending on the chamber radius and the magnetic field strength. This needs to be considered, when recording depth-dose curves and output factors for machine commissioning and QA.

The response of OSLDs slightly decreases for an increasing magnetic field perpendicular to the beam. For a magnetic field parallel to the beam, no change in detector response was observed. Magnetic field correction factors can be calculated with Monte Carlo simulations. However, if the detector calibration takes place directly in the MRgRT machine in presence of the magnetic field, no additional correction factor needs to be applied. The magnetic field has no measurable effect on the angular dependence of OSLDs with respect to the beam direction. Still the angular dependence of the OSL detectors is considerable and needs to be taken into account, when the detectors are irradiated under different angles. High precision QA and in-vivo dosimetry in hybrid MRgRT devices can be performed with OSLDs.

In general, magnetic field correction factors have to be calculated by Monte Carlo simulations for each detector, beam quality and magnetic field strength used. For a set-up with the magnetic field perpendicular to beam and chamber, small ionization chambers are beneficial, since they reveal the smallest corrections for this orientation. However, a set-up with the magnetic field parallel to the chamber is generally favorable for reference dosimetry, because the influence of possible dead volumes is minimized and the magnetic field correction factors for all chambers are lower than for a perpendicular magnetic field.
For a magnetic field parallel to the beam, only a small dependence of the chamber response on the chamber volume was observed. For this orientation, the smaller the magnetic field strength, the smaller is the change in response.

In future work, the Monte Carlo calculated magnetic field correction factors for ionization chambers should be compared with and validated by measured values in currently developed magnetic field compatible calorimeters.
Moreover, the effects of the magnetic field on typical high precision small field detectors like diodes, diamond detectors and scintillators need to be investigated. Since the hybrid MRgRT devices have the potential to reduce target volume margins, small radiation fields will be used routinely. Like OSL detectors, small field semiconductor detectors are commonly used for relative dosimetry and are cross-calibrated in the beam. Consequently, no absolute magnetic field correction factors are needed, but the influence of the magnetic field on the effective point of measurement, the angular dependence and dependence on the energy spectrum needs to be studied.

Additionally, a new dosimetry protocol for dosimetry in magnetic fields has to be established, tabulating magnetic field correction factors for common beam qualities, magnetic field strength, chamber types and orientations between beam, magnetic field and chamber. Recommendations concerning the chamber set-up and suitable phantoms for reference measurements should be given.

Closely related to MR-linac devices is the idea of hybrid MR particle therapy machines. Hence, ion beam dosimetry in a magnetic field may be a future challenge.

However, the secondary electrons produced when ions traverse through matter have only a small energy in the lower keV regsion and thus a very small range. Therefore, the effect of the electron deflection by the Lorentz force is small, so that only relatively small changes in the detector response due to the magnetic field are expected. Still, the effect of the magnetic field on the primary and secondary ions has to be considered and should be investigated.

List of publications

Journal articles

O. Schrenk, **C. K. Spindeldreier**, L. N. Burigo, J. Hoerner-Rieber, A. Pfaffenberger: "Effects of magnetic field orientation and strength on the treatment planning of non-small cell lung cancer", *accepted by Medical Physics (2017)*

Parts of this thesis have been published in the following references:

C. K. Spindeldreier, O. Schrenk, A. Bakenecker, I. Kawrakow, L. Burigo, C. P. Karger, S. Greilich & A. Pfaffenberger: "Radiation dosimetry in magnetic fields with Farmer-type ionization chambers: Determination of magnetic field correction factors for different magnetic field strengths and field orientations", *Physics in Medicine and Biology 62(16) (2017)*

C. K. Spindeldreier, O. Schrenk, M. F. Ahmed, N. Shrestha, C. P. Karger, S. Greilich, A. Pfaffenberger & E. G. Yukihara: "Feasibility of dosimetry with optically stimulated luminescence detectors in magnetic fields", *accepted by Radiation Measurements (2017)*

Conference contributions

B. Shukla, **C. K. Spindeldreier**, O. Schrenk, S. Greilich, C. P. Karger & A. Pfaffenberger: "Influence of a magnetic field on the response of the MR-compatible Exradin A19MR Farmer-type ionization chamber", *DGMP 48 (2017)* (poster)

C. K. Spindeldreier, O. Schrenk, C. P. Karger, S. Greilich & A. Pfaffenberger:"The effective point of measurement of Farmer ionization chambers in magnetic fields" *AAPM 59 (2017)* (poster)

C. K. Spindeldreier, I. Kawrakow, O. Schrenk, S. Greilich, C. P. Karger & A. Pfaffenberger: "PO-0761: Dosimetry with Farmer ionization chambers in magnetic fields: Influence of the sensitive volume", *Radiotherapy and Oncology 123 (2017): S401-S402 (Proceedings of ESTRO 36)* (poster)

O. Schrenk, **C. K. Spindeldreier** & A. Pfaffenberger: "The impact of lung tumor motion to the dose delivery in magnetic fields", *MRinRT 5 (2017)* (talk)

C. K. Spindeldreier, O. Schrenk, L. Burigo, S. Greilich, C. P. Karger & A. Pfaffenberger: "Dosimetry in magnetic fields", *DGMP webinar (2016)* (talk)

C. K. Spindeldreier, O. Schrenk, S. Greilich, C. P. Karger & A. Pfaffenberger: "Dosimetrie mit Ionisationskammern für die MR-geführte Strahlentherapie: Einfluss der Orientierung von Kammer und Magnetfeld", *DGMP 47 (2016)* (talk)

O. Schrenk, **C. K. Spindeldreier**, O. Schramm & A. Pfaffenberger: "Monte-Carlo basierte Bestrahlungsplanung für die MR-geführte Strahlentherapie von nichtkleinzelligen Bronchialkarzinomen", *DGMP 47 (2016)* (talk)

C. K. Spindeldreier, O. Schrenk, M. F. Ahmed, N. Shrestha, C. P. Karger, S. Greilich, A. Pfaffenberger & E. G. Yukihara: "Feasibility tests of optically stimulated luminescence detectors for dosimetry in magnetic fields", *SSD 18 (2016)* (poster)

C. K. Spindeldreier, O. Schrenk, S. Greilich, C. P. Karger & A. Pfaffenberger: "PO-0814: Beam quality and perturbation factors of Farmer chambers in magnetic fields", *Radiotherapy and Oncology 119 (2016): S384-S385 (Proceedings of ESTRO 35)* (poster)

O. Schrenk, **C. K. Spindeldreier** & A. Pfaffenberger: "OC-0550: Investigation of magnetic field effects for the treatment planning of lung cancer", *Radiotherapy and Oncology 119 (2016): S263 (Proceedings of ESTRO 35)* (talk)

Acknowledgments

This thesis would have never been possible without a number of people contributing in different ways to this work. I am very grateful to everyone of you!

First, I would like to thank Prof. Joao Seco, head of the division *Biomedical Physics in Radiation Oncology* (DKFZ), and Prof. Dr. Oliver Jäkel, head of the division *Medical Physics in Radiation Oncology* (DKFZ), for being the referees of this thesis. I am very grateful to Prof. Dr. Nobert Herrmann and Prof. Dr. Joerg Jaeckel, professors at the University of Heidelberg, who serve as examiners in the disputation of this thesis.
Very special thanks go to Dr. Asja Pfaffenberger for accepting me as the first member in her research group, supporting me wherever needed, while giving me the freedom to pursue own ideas. Along with Prof. Dr. Wolfgang Schlegel, Prof. Dr. Joao Seco, Prof. Dr. Christian Karger, Dr. Steffen Greilich, Dr. Bernhard Rhein, you are gratefully acknowledged for serving as members in my thesis advisory committee, giving me advice and steering the thesis in the right direction.

I would like to thank the whole *Medical Physics in Radiation Oncology* division and especially the group *MR-guided Radiation Therapy*, Oli, Nina, Kai, Lucas, Bhargesh, Marco and Nami, for the pleasant working atmosphere, our AG-meetings, coffee breaks and ice cream breaks. Particular, I thank Nina for our run training, continuous mutual motivation and for being a wonderful room-mate on numerous conferences and symposia. Along with Oli, you are gratefully acknowledged for our pleasant team work in the "Junge Medizinphysik" sessions at the DGMP conferences. Moreover, I thank Lucas and Christoph for trouble-shooting of the computer cluster, helping with the Monte Carlo simulations as well as general IT issues. I am grateful to my former and current office mates, Oli, Kathrin, Simon, Paul, Markus and Nami, who always succeeded in providing a pleasant and helpful working atmosphere - with such office mates and a lollipop, life's roller coaster is way more fun! Furthermore, I thank the whole E0401/3 working group for our nice lunch, coffee and cake breaks. Particularly, Paul and Christian are acknowledged for their Linux and general IT support. I thank the whole department for our wonderful retreats, several "Bier um 4 (um 5)" meetings and other activities. Especially, I would like to thank Christian, Julia, Giulia, Tim and Philip for always having an "offenes Ohr", your advise and ideas and the fun times we shared e.g. at conferences. Thank you, Bernadette, for encouraging me to apply for the PhD stipend and all your help and advise related to that.

Furthermore, I would like to express my gratitude to Prof. Dr. Eduardo Yukihara for hosting me at his research lab at OSU in Stillwater. I thank the whole lab team for the pleasant working atmosphere as well as Dr. Olga Green and Austen Curcuru for facilitating the measurements in St. Louis. Moreover, I wish to thank the working group *Medical Engineering*, especially Armin and Gernot, for making all the vague ideas of phantoms and holders possible and for technical trouble-shooting if again something broke or just won't fit as it should. Special thanks also go to Peter, Clemens, Mona and Christiane for facilitating the linac measurements and resolving every "Controller 0" interlock.

Additionally, Dr. Iwan Kawarakow is gratefully acknowledged for providing pieces of Monte Carlo code and as for answering all questions concerning the code and the ViewRay® machine. I wish to thank Dr. Edmund Schuele and Rafael Kranzer from PTW as well as Prof. Dr. Markus Alber for helping me with technical information on the chamber designs. Many thanks go also to the DKFZ core facility small animal imaging for providing the µCT data.

I would like to thank the Radiooncology and Radiation Therapy team of the Heidelberg University Hospital, especially Gerald, Sebastian, Laura and Dieter - thank you for showing me the "clinical world" and teaching me the QA procedures.

Of course, I would like to thank my friends (in Bielefeld, Düsseldorf, Heidelberg,..) and family for the never-ending encouragement and for always reminding me of the non-scientific part of life. In particular, I am very thankful to Ann-Christin for proofreading this thesis as well as many other scripts, but also for our motivating coffee breaks and wine evenings.

Very special thanks go to my family - without you, all this would not have been possible. Thanks for letting me find my way, encouraging me to do the next step, always providing me several havens and supporting me in so many ways. Last, but not least, thank you, Nico, for your never-ending motivation, patience and love!

Bibliography

Agnew, J. P., O'Grady, F., Young, R., Duane, S., & Budgell, G. (2017). Quantification of static magnetic field effects on radiotherapy ionization chambers. *Physics in Medicine and Biology*, 62(5):1731–1743.

Ahmed, M. F., Eller, S. A., Schnell, E., Ahmad, S., Akselrod, M. S., Hanson, O. D., & Yukihara, E. G. (2014). Development of a 2D dosimetry system based on the optically stimulated luminescence of Al2O3. *Radiation Measurements*, 71:187–192.

Ahmed, M. F., Shrestha, N., Ahmad, S., Schnell, E., Akselrod, M. S., & Yukihara, E. G. (2017). Demonstration of 2D dosimetry using Al2O3 optically stimulated luminescence films for therapeutic megavoltage x-ray and ion beams. *accepted by Radiation Measurements.*

Ahmed, M. F., Shrestha, N., Schnell, E., Ahmad, S., Akselrod, M. S., & Yukihara, E. G. (2016). Characterization of Al2O3 optically stimulated luminescence films for 2D dosimetry using a 6 MV photon beam. *Physics in Medicine and Biology*, 61(21):7551–7570.

Akselrod, M. S., Kortov, V. S., Kravetsky, D. J., & Gotlib, V. I. (1990). Highly Sensitive Thermoluminescent Anion-Defect Alpha-Al2O3:C Single Crystal Detectors. *Radiation Protection Dosimetry*, 33(1-4):119–122.

Akselrod, M. S., Lucas, A. C., Polf, J. C., & McKeever, S. W. S. (1998). Optically stimulated luminescence of Al2O3. *Radiation Measurements*, 29(3):391–399.

Almond, P. R., Biggs, P. J., Coursey, B. M., Hanson, W. F., Huq, M. S., Nath, R., & Rogers, D. W. O. (1999). AAPM's TG-51 protocol for clinical reference dosimetry of high-energy photon and electron beams. *Medical Physics*, 26(9):1847–1870.

Andreo, P., Burns, D. T., Hohlfeld, K., Huq, M. S., Kanai, T., Laitano, F., Smyth, V., & Vynckier, S. (2006). Absorbed Dose Determination in External Beam Radiotherapy: An International Code of Practice for Dosimetry based on Standards of Absorbed Dose to Water. *IAEA TRS-398.*

Attix, F. H. (2004). *Introduction to Radiological Physics and Radiation Dosimetry.* Wiley-VCH Verlag GmbH.

Bakenecker, A. (2014). Dose measurements with ionization chambers in magnetic fields using 6 MeV photons. Master thesis, University of Heidelberg.

Barten, D. L. J., Van Battum, L. J., Hoffmans, D., & Heukelom, S. (2017). The suitability of radiochromic film in 0.35T magnetic field CO-60 compared with conventional 6MV. *Radiotherapy and Oncology*, 123(Supplement 1):S115 – S116.

Benmakhlouf, H., Sempau, J., & Andreo, P. (2014). Output correction factors for nine small field detectors in 6 MV radiation therapy photon beams: a PENELOPE Monte Carlo study. *Medical Physics*, 41(4):041711.

Berger, M. J., Hubbell, J. H., Seltzer, S. M., Chang, J., Coursey, J. S., Sukumar, R., Zucker, D. S., & Olsen, K. (2010). XCOM: Photon Cross Section Database (version 1.5). *National Institute of Standards and Technology, Gaithersburg, MD.*

Bielajew, A. F. (1993). The effect of strong longitudinal magnetic fields on dose deposition from electron and photon beams. *Medical Physics*, 20(4):1171–1179.

Bielajew, A. F. (2001). Fundamentals of the Monte Carlo method for neutral and charged particle transport. *The University of Michigan.*

Borg, J., Kawrakow, I., Rogers, D. W. O., & Seuntjens, J. P. (2000). Monte Carlo study of correction factors for Spencer-Attix cavity theory at photon energies at or above 100 keV. *Medical Physics*, 27(8):1804–1813.

Bos, A. J. J. (2001). High sensitivity thermoluminescence dosimetry. *Nuclear Instruments and Methods in Physics Research Section B: Beam Interactions with Materials and Atoms*, 184(1-2):3–28.

Bostel, T., Nicolay, N. H., Grossmann, J. G., Mohr, A., Delorme, S., Echner, G., Häring, P., Debus, J., & Sterzing, F. (2014). MR-guidance - a clinical study to evaluate a shuttle-based MR-linac connection to provide MR-guided radiotherapy. *Radiation Oncology*, 9(12):1–8.

Bøtter-Jensen, L., Agersnap Larsen, N., Markey, B. G., & McKeever, S. W. S. (1997). Al2O3:C as a sensitive OSL dosemeter for rapid assessment of environmental photon dose rates. *Radiation Measurements*, 27(2):295–298.

Bouchard, H. & Bielajew, A. (2015). Lorentz force correction to the Boltzmann radiation transport equation and its implications for Monte Carlo algorithms. *Physics in Medicine and Biology*, 60(13):4963–4971.

Bouchard, H., De Pooter, J., Bielajew, A., & Duane, S. (2015). Reference dosimetry in the presence of magnetic fields: conditions to validate Monte Carlo simulations. *Physics in Medicine and Biology*, 60(17):6639–6654.

Brualla, L., Salvat, F., & Palanco-Zamora, R. (2009). Efficient Monte Carlo simulation of multileaf collimators using geometry-related variance-reduction techniques. *Physics in Medicine and Biology*, 54(13):4131–4149.

Butler, D. J., Stevenson, A. W., Wright, T. E., Harty, P. D., Lehmann, J., Livingstone, J., & Crosbie, J. C. (2015). High spatial resolution dosimetric response maps for radiotherapy ionization chambers measured using kilovoltage synchrotron radiation. *Physics in Medicine and Biology*, 60(22):8625–8641.

Chan, H.-P. & Doi, K. (1985). Physical characteristics of scattered radiation in diagnostic radiology: Monte Carlo simulation studies. *Medical Physics*, 12(2):152–165.

Chen, A. M., Hsu, S., Lamb, J., Yang, Y., Agazaryan, N., Steinberg, M. L., Low, D. A., & Cao, M. (2017). MRI-guided radiotherapy for head and neck cancer: initial clinical experience. *Clinical and Translational Oncology*, pages 1–9.

Comte de Buffon, G. (1777). Essai d'arithmétique morale. *Supplément à l'Histoire Naturelle*, 4.

Crijns, S. P. M., Raaymakers, B. W., & Lagendijk, J. J. W. (2011). Real-time correction of magnetic field inhomogeneity-induced image distortions for MRI-guided conventional and proton radiotherapy. *Physics in Medicine and Biology*, 56(1):289–297.

Crop, F., Reynaert, N., Pittomvils, G., Paelinck, L., De Wagter, C., Vakaet, L., & Thierens, H. (2009). The influence of small field sizes, penumbra, spot size and measurement depth on perturbation factors for microionization chambers. *Physics in Medicine and Biology*, 54(9):2951–2969.

Czarnecki, D. & Zink, K. (2013). Monte Carlo calculated correction factors for diodes and ion chambers in small photon fields. *Physics in Medicine and Biology*, 58(8):2431–2444.

De Pooter, J. A., De Prez, L. A., & Bouchard, H. (2015). Application of an adapted Fano cavity test for Monte Carlo simulations in the presence of B-fields. *Physics in Medicine and Biology*, 60(24):9313–9327.

De Prez, L., De Pooter, J., Jansen, B., & Aalbers, T. (2016a). A water calorimeter for on-site absorbed dose to water calibrations in 60Co and MV-photon beams including MRI incorporated treatment equipment. *Physics in Medicine and Biology*, 61(13):5051–5076.

De Prez, L., De Pooter, J., Jansen, B., Wolthaus, J., van Asselen, B., Woodings, S., Soest, T., Kok, J., & Raaymakers, B. (2016b). TH-CD-BRA-05: First Water Calorimetric Dw Measurement and Direct Measurement of Magnetic Field Correction Factors, KQ,B, in a 1.5 T B-Field of An MRI Linac. *Medical Physics*, 43(6Part45):3874–3874.

DeMarco, J. J., Cagnon, C. H., Cody, D. D., Stevens, D. M., McCollough, C. H., O'Daniel, J., & McNitt-Gray, M. F. (2005). A Monte Carlo based method to estimate radiation dose from multidetector CT (MDCT): cylindrical and anthropomorphic phantoms. *Physics in Medicine and Biology*, 50(17):3989–4004.

DIN (2008). DIN 6800-2 Dosismessverfahren nach der Sondenmethode für Photonen- und Elektronenstrhalung - Teil 2: Dosimetrie hochenergetischer Photonen- und Elektronenstrahlung mit Ionisationskammern. *Deutsches Institut für Normung e.V.*

Fallone, B. G. (2014). The Rotating Biplanar Linac-Magnetic Resonance Imaging System. *Seminars in Radiation Oncology*, 24(3):200–202.

Fallone, B. G., Murray, B., Rathee, S., Stanescu, T., Steciw, S., Vidakovic, S., Blosser, E., & Tymofichuk, D. (2009). First MR images obtained during megavoltage photon irradiation from a prototype integrated linac-MR system. *Medical Physics*, 36(6):2084–2088.

Fano, U. (1954). Note on the Bragg-Gray Cavity Principle for Measuring Energy Dissipation. *Radiation Research*, 1(3):237 – 240.

Fedorov, A., Beichel, R., Kalpathy-Cramer, J., Finet, J., Fillion-Robin, J.-C., Pujol, S., Bauer, C., Jennings, D., Fennessy, F., Sonka, M., Buatti, J., Aylward, S., Miller, J. V., Pieper, S., & Kikinis, R. (2012). 3D Slicer as an image computing platform for the Quantitative Imaging Network. *Magnetic Resonance Imaging*, 30(9):1323–1341.

Fischer-Valuck, B. W., Henke, L., Green, O., Kashani, R., Acharya, S., Bradley, J. D., Robinson, C. G., Thomas, M., Zoberi, I., Thorstad, W., Gay, H., Huang, J., Roach, M., Rodriguez, V., Santanam, L., Li, H., Li, H., Contreras, J., Mazur, T., Hallahan, D., Olsen, J. R., Parikh, P., Mutic, S., & Michalski, J. (2017). Two-and-a-half-year clinical experience with the world's first magnetic resonance image guided radiation therapy system. *Advances in Radiation Oncology*, 2(3):485–493.

Fogliata, A., Vanetti, E., Albers, D., Brink, C., Clivio, A., Knöös, T., Nicolini, G., & Cozzi, L. (2007). On the dosimetric behaviour of photon dose calculation algorithms in the presence of simple geometric heterogeneities: comparison with Monte Carlo calculations. *Physics in Medicine and Biology*, 52(5):1363–1385.

Ford, R. L. & Nelson, W. R. (1978). The EGS code system: Computer programs for the Monte Carlo simulation of electromagnetic cascade showers. Technical report, Stanford Linear Accelerator Center.

Ghila, A., Steciw, S., Fallone, B. G., & Rathee, S. (2017). Experimental verification of EGSnrc Monte Carlo calculated depth doses within a realistic parallel magnetic field in a polystyrene phantom. *Medical Physics*, 44(9):4804–4815.

Glitzner, M., Crijns, S. P. M., Senneville, B. D. D., Kontaxis, C., Prins, F. M., Lagendijk, J. J. W., & Raaymakers, B. W. (2015). On-line MR imaging for dose validation of abdominal radiotherapy. *Physics in Medicine and Biology*, 60(22):8869–8883.

Gomà, C., Andreo, P., & Sempau, J. (2016). Monte Carlo calculation of beam quality correction factors in proton beams using detailed simulation of ionization chambers. *Physics in Medicine and Biology*, 61(6):2389–2406.

Hackett, S. L., Van Asselen, B., Wolthaus, J. W. H., Kok, J. G. M., Woodings, S. J., Lagendijk, J. J. W., & Raaymakers, B. W. (2016). Consequences of air around an ionization chamber: Are existing solid phantoms suitable for reference dosimetry on an MR-linac? *Medical Physics*, 43(7):3961–3968.

Houweling, A. C., De Vries, J. H. W., Wolthaus, J., Woodings, S., Kok, J. G. M., Van Asselen, B., Smit, K., Bel, A., Lagendijk, J. J. W., & Raaymakers, B. W. (2016). Performance of a cylindrical diode array for use in a 1.5 T MR-linac. *Physics in Medicine and Biology*, 61(3):N80–N89.

Ibbott, G. S., Roed, Y., Lee, H., Alqathami, M., Wang, J., Pinsky, L., & Blencowe, A. (2016). Gel dosimetry enables volumetric evaluation of dose distributions from an MR-guided linac. In: *AIP Conference Proceedings 1747*.

Jaffray, D. A., Carlone, M. C., Milosevic, M. F., Breen, S. L., Stanescu, T., Rink, A., Alasti, H., Simeonov, A., Sweitzer, M. C., & Winter, J. D. (2014). A Facility for Magnetic Resonance-Guided Radiation Therapy. *Seminars in Radiation Oncology*, 24(3):193–195.

Jursinic, P. A. (2007). Characterization of optically stimulated luminescent dosimeters, OSLDs, for clinical dosimetric measurements. *Medical Physics*, 3436(37):1690–1699.

Kalos, M. H. & Whitlock, P. A. (2008). *Monte Carlo Methods*. Wiley-Blackwell.

Karlsson, M., Karlsson, M. G., Nyholm, T., Amies, C., & Zackrisson, B. (2009). Dedicated Magnetic Resonance Imaging in the Radiotherapy Clinic. *International Journal of Radiation Oncology Biology Physics*, 74(2):644–651.

Kawrakow, I. (2000a). Accurate condensed history Monte Carlo simulation of electron transport. I. EGSnrc, the new EGS4 version. *Medical Physics*, 27(3):485–498.

Kawrakow, I. (2000b). Accurate condensed history Monte Carlo simulation of electron transport. II. Application to ion chamber response simulations. *Medical Physics*, 27(3):499–513.

Kawrakow, I. (2006). On the effective point of measurement in megavoltage photon beams. *Medical Physics*, 33(6):1829–1839.

Kawrakow, I. & Fippel, M. (2000). Investigation of variance reduction techniques for Monte Carlo photon dose calculation using XVMC. *Physics in Medicine and Biology*, 45(8):2163–2183.

Kawrakow, I., Mainegra-Hing, E., Rogers, D. W. O., Tessier, F., & Walters, B. R. B. (2017). The EGSnrc Code System: Monte Carlo Simulation of Electron and Photon Transport. Technical report, NRC.

Kawrakow, I., Mainegra-Hing, E., Tessier, F., & Walters, B. R. B. (2009). The EGSnrc C++ class library. *NRC Report PIRS-898 (rev A)*.

Keall, P. J., Barton, M., & Crozier, S. (2014). The Australian Magnetic Resonance Imaging-Linac Program. *Seminars in Radiation Oncology*, 24(3):203–206.

Kerns, J. R., Kry, S. F., Sahoo, N., Followill, D. S., & Ibbott, G. S. (2011). Angular dependence of the nanoDot OSL dosimeter. *Medical Physics*, 38(7):3955–3962.

Ketelhut, S. & Kapsch, R.-P. (2015). Measurement of spatial response functions of dosimetric detectors. *Physics in Medicine and Biology*, 60(16):6177–6194.

Khan, F. M. & Gibbons, J. P. (2014). *Khan's the physics of radiation therapy*. Wolters Kluwer.

Krieger, H. (2012). *Grundlagen der Strahlungsphysik und des Strahlenschutzes*. Vieweg+Teubner Verlag.

Kupelian, P. & Sonke, J. J. (2014). Magnetic Resonance-Guided Adaptive Radiotherapy: A Solution to the Future. *Seminars in Radiation Oncology*, 24(3):227–232.

La Russa, D. J. & Rogers, D. W. O. (2008). Accuracy of EGSnrc calculations at 60Co energies for the response of ion chambers configured with various wall materials and cavity dimensions. *Medical Physics*, 35(12):5629–5640.

Lagendijk, J. J. W., Raaymakers, B. W., Van den Berg, C. A. T., Moerland, M. A., Philippens, M. E., & Van Vulpen, M. (2014a). MR guidance in radiotherapy. *Physics in Medicine and Biology*, 59(21):R349–R369.

Lagendijk, J. J. W., Raaymakers, B. W., & Van Vulpen, M. (2014b). The Magnetic Resonance Imaging-Linac System. *Seminars in Radiation Oncology*, 24(3):207–209.

Lee, H., Alqathami, M., Kadbi, M., Wang, J., Blencowe, A., & Ibbott, G. (2016). TH-CD-BRA-08: Novel Iron-Based Radiation Reporting Systems as 4D Dosimeters for MR-Guided Radiation Therapy. *Medical Physics*, 43(6Part45):3874–3875.

Legrand, C., Hartmann, G. H., & Karger, C. P. (2012a). Experimental determination of the effective point of measurement and the displacement correction factor for cylindrical ionization chambers in a 6 MV photon beam. *Physics in Medicine and Biology*, 57(21):6869–6880.

Legrand, C., Hartmann, G. H., & Karger, C. P. (2012b). Experimental determination of the effective point of measurement for cylindrical ionization chambers in 60Co gamma radiation. *Physics in Medicine and Biology*, 57(11):3463–3475.

Liauw, S. L., Connell, P. P., & Weichselbaum, R. R. (2013). New paradigms and future challenges in radiation oncology: an update of biological targets and technology. *Science Translational Medicine*, 5(173):173sr2.

Looe, H. K., Delfs, B., Poppinga, D., Harder, D., & Poppe, B. (2017). Magnetic field influences on the lateral dose response functions of photon-beam detectors: MC study of wall-less water-filled detectors with various densities. *Physics in Medicine and Biology*, 62(12):5131–5148.

Malkov, V. N. & Rogers, D. W. O. (2016). Charged particle transport in magnetic fields in EGSnrc. *Medical Physics*, 43(7):4447–4458.

Malkov, V. N. & Rogers, D. W. O. (2017). Sensitive volume effects on Monte Carlo calculated ion chamber response in magnetic fields. *Medical Physics*, 44(9):4854–4858.

Mathis, M., Sawakuchi, G., Flint, D., Tailor, R., Beddar, S., Ibbott, G., & Wen, Z. (2014). Effects of a strong magnetic field on selected radiation dosimeters (TLD, OSLD, EBT3 film, PRESAGE). *Journal of Medical Imaging and Radiology Oncology*, 58:336.

Meeker, D. (2015). Finite Element Method Magnetics. *www.femm.info (accessed November 8, 2017).*

Meijsing, I., Raaymakers, B. W., Raaijmakers, A. J. E., Kok, J. G. M., Hogeweg, L., Liu, B., & Lagendijk, J. J. W. (2009). Dosimetry for the MRI accelerator: the impact of a magnetic field on the response of a Farmer NE2571 ionization chamber. *Physics in Medicine and Biology*, 54(10):2993–3002.

Mohan, R., Chui, C., & Lidofsky, L. (1985). Energy and angular distributions of photons from medical linear accelerators. *Medical Physics*, 12(5):592–597.

Moteabbed, M., Schuemann, J., & Paganetti, H. (2014). Dosimetric feasibility of real-time MRI-guided proton therapy. *Medical Physics*, 41(11):111713.

Muir, B. R. & Rogers, D. W. O. (2010). Monte Carlo calculations of kQ the beam quality conversion factor. *Medical Physics*, 37(11):5939–5950.

Mutic, S. & Dempsey, J. F. (2014). The ViewRay System: Magnetic Resonance-Guided and Controlled Radiotherapy. *Seminars in Radiation Oncology*, 24(3):196–199.

Oborn, B. M., Dowdell, S., Metcalfe, P. E., Crozier, S., Mohan, R., & Keall, P. J. (2015). Proton beam deflection in MRI fields: Implications for MRI-guided proton therapy. *Medical Physics*, 42(5):2113–2124.

Oborn, B. M., Dowdell, S., Metcalfe, P. E., Crozier, S., Mohan, R., & Keall, P. J. (2017). Future of medical physics: Real-time MRI-guided proton therapy. *Medical Physics*, 44(8):e77–e90.

O'Brien, D. J., Roberts, D. A., Ibbott, G. S., & Sawakuchi, G. O. (2016). Reference dosimetry in magnetic fields: formalism and ionization chamber correction factors. *Medical Physics*, 43(8):4915–4927.

O'Brien, D. J. & Sawakuchi, G. O. (2016). TH-CD-BRA-07: MRI-Linac Dosimetry: Parameters That Change in a Magnetic Field. *Medical Physics*, 43(6Part45):3874–3874.

O'Brien, D. J. & Sawakuchi, G. O. (2017). Monte Carlo study of the chamber-phantom air gap effect in a magnetic field. *Medical Physics*, 44(7):3830–3838.

Pena, J., González-Castaño, D. M., Gómez, F., Sánchez-Doblado, F., & Hartmann, G. H. (2007). Automatic determination of primary electron beam parameters in Monte Carlo simulation. *Medical Physics*, 34(3):1076–1084.

Podgorsak, E. B. (2005). *Radiation Oncology Physics: A Handbook for Teachers and Students*. International Atomic Energy Agency.

Pojtinger, S., Dohm, O., & Thorwarth, D. (2017). OC-0261: Monte Carlo Correction Factors for MRgRT Reference Dosimetry. *Radiotherapy and Oncology*, 123:S134.

PTW (2017). Ionizing Radiation Detectors. Technical report.

R Core Team (2016). R: A language and environment for statistical computing. *https://www.r-project.org/ (accessed November 8, 2017)*.

Raaijmakers, A. J. E., Hårdemark, B., Raaymakers, B. W., Raaijmakers, C. P. J., & Lagendijk, J. J. W. (2007). Dose optimization for the MRI-accelerator: IMRT in the presence of a magnetic field. *Physics in Medicine and Biology*, 52(23):7045–7054.

Raaijmakers, A. J. E., Raaymakers, B. W., & Lagendijk, J. J. W. (2005). Integrating a MRI scanner with a 6 MV radiotherapy accelerator: dose increase at tissue-air interfaces in a lateral magnetic field due to returning electrons. *Physics in Medicine and Biology*, 50(7):1363–1376.

Raaijmakers, A. J. E., Raaymakers, B. W., & Lagendijk, J. J. W. (2008). Magnetic-field-induced dose effects in MR-guided radiotherapy systems: dependence on the magnetic field strength. *Physics in Medicine and Biology*, 53(4):909–923.

Raaymakers, B. W., Raaijmakers, A. J. E., & Lagendijk, J. J. W. (2008). Feasibility of MRI guided proton therapy: magnetic field dose effects. *Physics in Medicine and Biology*, 53(20):5615–5622.

Reynolds, M., Fallone, B. G., & Rathee, S. (2013). Dose response of selected ion chambers in applied homogeneous transverse and longitudinal magnetic fields. *Medical Physics*, 40(4):042102.

Reynolds, M., Fallone, B. G., & Rathee, S. (2014). Dose response of selected solid state detectors in applied homogeneous transverse and longitudinal magnetic fields. *Medical Physics*, 41(9):092103.

Reynolds, M., Fallone, B. G., & Rathee, S. (2015). Technical Note: Response measurement for select radiation detectors in magnetic fields. *Medical Physics*, 42(6Part1):2837–2840.

Reynolds, M., Rathee, S., & Fallone, B. G. (2017). Ion Chamber Angular Dependence in a Magnetic Field. *Medical Physics*, 44(8):4322–4328.

Reynoso, F. J., Curcuru, A., Green, O., Mutic, S., Das, I. J., & Santanam, L. (2016). Technical Note: Magnetic field effects on Gafchromic-film response in MR-IGRT. *Medical Physics*, 43(12):6552–6556.

Rogers, D. W. O. (2006). Fifty years of Monte Carlo simulations for medical physics. *Physics in Medicine and Biology*, 51(13):R287–R301.

Rogers, D. W. O., Emwart, G. M., Bielajew, A. F., & Van Dyk, G. (1988). Calculation of electron contamination in a 60Co therapy beam. *Proceedings of IAEA International symposium. Vol. 1.*

Rogers, D. W. O., Kawrakow, I., Seuntjens, J. P., Walters, B. R. B., & Mainegra-Hing, E. (2017a). NRC User Codes for EGSnrc. Technical report, NRC.

Rogers, D. W. O., Walters, B., & Kawrakow, I. (2017b). BEAMnrc Users Manual. Technical report, NRC.

Schellhammer, S. M. & Hoffmann, A. L. (2017). Prediction and compensation of magnetic beam deflection in MR-integrated proton therapy: a method optimized regarding accuracy, versatility and speed. *Physics in Medicine and Biology*, 62(4):1548–1564.

Schlegel, W. & Bille, J. (2002). Medizinische Strahlenphysik. In: *Medizinische Physik 2*. Springer-Verlag.

Schwarzbeck Mess-Elektronik. Electromagnet with variable Air Gap AGEM 5520. Technical report.

Seco, J. & Verhaegen, F. (2013). *Monte Carlo Techniques in Radiation Therapy*. CRC Press.

Sempau, J. & Andreo, P. (2006). Configuration of the electron transport algorithm of PENELOPE to simulate ion chambers. *Physics in Medicine and Biology*, 51(14):3533–3548.

Sheikh-Bagheri, D. & Rogers, D. W. O. (2002). Monte Carlo calculation of nine megavoltage photon beam spectra using the BEAM code. *Medical Physics*, 29(3):391–402.

Shukla, B. (2017). Dosimetry in magnetic field using ionization chambers. Master thesis, Kaunas University of Technology.

Smit, K., Kok, J. G. M., Lagendijk, J. J. W., & Raaymakers, B. W. (2014a). Performance of a multi-axis ionization chamber array in a 1.5 T magnetic field. *Physics in Medicine and Biology*, 59(7):1845–55.

Smit, K., Sjöholm, J., Kok, J. G. M., Lagendijk, J. J. W., & Raaymakers, B. W. (2014b). Relative dosimetry in a 1.5 T magnetic field: an MR-linac compatible prototype scanning water phantom. *Physics in Medicine and Biology*, 59(15):4099–4109.

Smit, K., van Asselen, B., Kok, J. G. M., Aalbers, A. H. L., Lagendijk, J. J. W., & Raaymakers, B. W. (2013). Towards reference dosimetry for the MR-linac: magnetic field correction of the ionization chamber reading. *Physics in Medicine and Biology*, 58(17):5945–5957.

Spencer, L. V. (1965). Note on the Theory of Cavity Ionization Chambers. *Radiation Research*, 25(2):352–358.

Spencer, L. V. (1971). Remarks on the Theory of Energy Deposition in Cavities. *Acta Radiologica: Therapy, Physics, Biology*, 10(1):1–20.

Spencer, L. V. & Attix, F. H. (1955). A Theory of Cavity Ionization. *Radiation Research*, 3(3):239–254.

Spindeldreier, C. K., Schrenk, O., Ahmed, M. F., Shrestha, N., Karger, C. P., Greilich, S., Pfaffenberger, A., & Yukihara, E. G. (2017a). Feasibility of dosimetry with optically stimulated luminescence detectors in magnetic fields. *accepted by Radiation Measurements*.

Spindeldreier, C. K., Schrenk, O., Bakenecker, A., Kawrakow, I., Burigo, L., Karger, C. P., Greilich, S., & Pfaffenberger, A. (2017b). Radiation dosimetry in magnetic fields with Farmer-type ionization chambers: determination of magnetic field correction factors for different magnetic field strengths and field orientations. *Physics in Medicine and Biology*, 62(16):6708 – 6728.

Standard Imaging (2016). Exradin MR-Compatible Ion Chambers. Technical report.

Stefanowicz, S., Latzel, H., Lindvold, L. R., Andersen, C. E., Jäkel, O., & Greilich, S. (2013). Dosimetry in clinical static magnetic fields using plastic scintillation detectors. *Radiation Measurements*, 56:357–360.

Tessier, F. & Kawrakow, I. (2009). Effective point of measurement of thimble ion chambers in megavoltage photon beams. *Medical Physics*, 37(1):96–107.

ViewRay (2015). The MRIdian Advantage Brochure.

Walters, B., Kawrakow, I., & Rogers, D. W. O. (2017). DOSXYZnrc Users Manual. Technical report, NRC.

Wang, J., Rubinstein, A., Ohrt, J., Ibbott, G., & Wen, Z. (2016). TH-CD-BRA-04: Effect of a Strong Magnetic Field On TLDs, OSLDs, and Gafchromic Films Using An Electromagnet. *Medical Physics*, 43(6Part45):3873–3874.

Wang, L. L. W. & Rogers, D. W. O. (2009). The replacement correction factors for cylindrical chambers in high-energy photon beams. *Physics in Medicine and Biology*, 54(6):1609–1620.

Wulff, J., Heverhagen, J. T., & Zink, K. (2008a). Monte-Carlo-based perturbation and beam quality correction factors for thimble ionization chambers in high-energy photon beams. *Physics in Medicine and Biology*, 53(11):2823–2836.

Wulff, J., Zink, K., & Kawrakow, I. (2008b). Efficiency improvements for ion chamber calculations in high energy photon beams. *Medical Physics*, 35(4):1328–1336.

Yukihara, E. G., Doull, B. A., Ahmed, M. F., Brons, S., Tessonnier, T., Jäkel, O., & Greilich, S. (2015). Time-resolved optically stimulated luminescence of Al2O3:C for ion beam therapy dosimetry. *Physics in Medicine and Biology*, 60(17):6613–6638.

Yukihara, E. G., Mardirossian, G., Mirzasadeghi, M., Guduru, S., & Ahmad, S. (2007). Evaluation of Al2O3:C optically stimulated luminescence (OSL) dosimeters for passive dosimetry of high-energy photon and electron beams in radiotherapy. *Medical Physics*, 35(1):260–269.

Yukihara, E. G. & McKeever, S. W. S. (2006). Spectroscopy and optically stimulated luminescence of Al2O3:C using time-resolved measurements. *Journal of Applied Physics*, 100(8):083512.

Yukihara, E. G. & McKeever, S. W. S. (2008). Optically stimulated luminescence (OSL) dosimetry in medicine. *Physics in Medicine and Biology*, 53(20):R351–R379.

Yukihara, E. G., Yoshimura, E. M., Lindstrom, T. D., Ahmad, S., Taylor, K. K., & Mardirossian, G. (2005). High-precision dosimetry for radiotherapy using the optically stimulated luminescence technique and thin Al2O3:C dosimeters. *Physics in Medicine and Biology*, 50(23):5619–28.